



DISSERTATION

Determination of the Strong Interaction Ground State Width in Pionic Hydrogen

ausgeführt zum Zwecke der Erlangung des akademischen Grades eines
Doktors der technischen Wissenschaften unter der Leitung von

ao.Univ.Prof. Dipl.-Ing. Dr.techn. Manfred Faber
am
Atominstitut der Österreichischen Universitäten – E141
und am
Stefan-Meyer-Institut für subatomare Physik
der Österreichischen Akademie der Wissenschaften

eingereicht an der Technischen Universität Wien
bei der Fakultät für Physik

von

Dipl.-Ing. Albert Hirtl
Matrikelnummer 9326754
Charasgasse 3/16
1030 Wien

Wien, im Februar 2008

To boldly go where no man has gone before

Vielen Dank!

Zuallererst danke ich meinen Eltern für ihre ständige Sorge um meine Zukunft. Trotz mancher gegenteiliger gesellschaftlicher Konvention und Dank ihres Wunsches ihren Kindern eine gute Ausbildung zu ermöglichen, haben sie durch ihre Selbstlosigkeit die Rahmenbedingungen geschaffen, die letztendlich wesentlich zum Gelingen dieser Arbeit beigetragen haben. Hvala lepa za vse!

Dank gebührt auch meinem Bruder Andreas, der mir in diversen nächtlichen Sitzungen im Alt Wien eindrücklich die wahre Funktionsweise der ganzen Welt erläutert hat. Auf Basis dieser Erkenntnisse wurden beinahe sämtliche Probleme dieser Welt gelöst. Im Prinzip zumindest.

Vielen Dank an Barbara, die unermüdlich gegen meine kulturelle Trägheit ankämpft und mich schließlich doch zu mancher Tätigkeit bewegen kann.

Großer Dank und Respekt gebühren in gleichem Maße Detlev Gotta und Leopold Simons, die mich bei meinem erstmaligen Erscheinen am PSI im Jahre 2002 sofort freundschaftlich aufgenommen haben. In den folgenden Jahren haben sie mich an ihrem reichen Erfahrungsschatz auf dem Gebiet der Experimental- und der Teilchenphysik teilhaben lassen. An dieser Stelle sei auf Detlevs Eigenschaft hingewiesen, selbst ob der allereigenartigsten Fragen nicht die Nerven zu verlieren und alles nochmal zu erklären. Unvergessen bleiben wird mir Leos äußerst klare Einführung in die Theorie des korrekten Kabellegens.

Folgende universelle Weisheit hat sich ebenfalls festgesetzt: "Junge das muss jetzt schnell gehen. Also machen wir ganz langsam!" Vielen Dank für alle (manchmal durchaus hitzigen) Debatten während der Strahlzeiten am PSI.

Gedankt sei Hannes Zmeskal, der mich zum Experiment am PSI "mitgenommen" hat und mir ob meiner anfänglichen Skepsis bezüglich meiner Fähigkeiten erklärt hat, dass das alles schon gehen wird.

Vielen Dank allen Mitarbeitern des Stefan-Meyer-Instituts für das hervorragende Arbeitsklima!

Vielen Dank an Manfred Faber für die Bereitschaft diese Dissertation zu betreuen und an Andrei Ivanov für zahlreiche aufschlussreiche Diskussionen über die theoretischen Grundlagen der QCD im Niederenergielimit.

Special thanks to Daniel Covita, Thomas Strauch and Martino Trassinelli, my comrades-in-suffering during long nights on shift, trying to understand what we are doing and how we could manage not to destroy the whole thing.

The hours lasting, though, unsuccessful search for food in and around Villigen on the 1st of August in 2005 will remain unforgotten!

Thanks to Paul Indelicato for the most interesting discussions on Star Trek!

An die subtile Beschreibung der Unterschiede zwischen Österreichern (–) und Schweizern (+) durch Bruno Leoni erinnere ich mich immer wieder gerne.

Finally, thanks to the whole π^- -H collaboration, where I found very interesting friends!

Zusammenfassung

Am Paul Scherrer Institut (PSI) wurden die hadronische Verschiebung (ϵ_{1s}) und Breite (Γ_{1s}) des Grundzustandsniveaus im pionischen Wasserstoff im Rahmen eines Präzisionsexperimentes (PSI-Experiment R-98-01) erneut gemessen. Die messbaren Größen ϵ_{1s} und Γ_{1s} stehen in direktem Zusammenhang mit den Pion-Nukleon Isospinstreulängen. Die exakte Kenntnis dieser Streulängen erlaubt eine Überprüfung der Aussagekraft von im niederenergielimit der Quantenchromodynamik (QCD) definierten effektiven Feldtheorien, wie zum Beispiel der Chiralen Störungstheorie. Darüber hinaus ist Γ_{1s} mit der Pion-Nukleon Kopplungskonstante $f_{\pi N}$ verknüpft. Die präzise Kenntnis von $f_{\pi N}$ erlaubt eine genaue Bestimmung der Goldberger-Treiman-Diskrepanz, die ein Maß für die chirale Symmetriebrechung darstellt.

Die Verschiebung ϵ_{1s} erhält man durch die Bildung der Differenz aus gemessenem Energiewert und dem rein elektromagnetischen Wert. Γ_{1s} erhält man aus der Entfaltung des Linienprofils bestehend aus hadronischer Breite, instrumenteller Auflösungsfunktion und Doppler-Verbreiterung. Die Doppler-Verbreiterung wird ausgelöst durch die Konversion der Abregungsenergie aus Coulomb-Übergängen in kinetische Energie der pionischen Wasserstoff-Atome (π^-p).

Die Messungen wurden am hoch-intensiven Pionen-Strahl der Beschleunigeranlage des PSI durchgeführt. Gemessen wurden Röntgenübergänge in den Grundzustand von pionischem Wasserstoff: $\pi^-p_{np \rightarrow 1s}$ mit $n = 2, 3, 4$. Im Gegensatz zu den Energien dieser Strahlungsübergänge (wenige keV), liegen die Energien der hadronischen Effekte lediglich im Bereich einiger eV. Daher ist die Verwendung eines hochauflösenden Kristallspektrometers unumgänglich.

Der Pionen-Strahl wurde mittels einer Zyklotronfalle in ein kryogenisches Wasserstoffgas-Target geführt. Die von den gebildeten pionischen Wasserstoff-Atomen ausgesendeten Röntgenstrahlen wurden an dem hochauflösenden Kristallspektrometer reflektiert und schließlich von einem großflächigen positionsempfindlichen Detektor nachgewiesen.

Die instrumentelle Auflösungsfunktion wurde mittels schmaler Röntgenübergänge in hochionisierten Atomen in einer Elektron-Zyklotron-Resonanz-Ionenfalle gemessen.

Die kinetische Energieverteilung der π^-p wurde durch ein Modell mit Box-artigen Verteilungen angenähert. Die Gültigkeit dieses Modells wurde anhand des $3p \rightarrow 1s$ Übergangs im nahe verwandten System des müonischen Wasserstoffs (μ^-p) überprüft. Im Gegensatz zum Pion unterliegt das Müon nicht der starken Wechselwirkung. Daher ist das Linienprofil von Röntgenübergängen in μ^-p sehr sensitiv auf die Doppler-Verbreiterung.

Zusammen mit der gemessenen instrumentellen Auflösungsfunktion wurde das Modell für die kinetische Energieverteilung in einem Analyseverfahren zur Bestimmung von Γ_{1s} verwendet. Dieses Analyseverfahren wurde in dieser Arbeit entwickelt und erstmals auf den $4p \rightarrow 1s$ Übergang in π^-p angewendet. Man erhält $\Gamma_{1s} = 765 \pm 56$ meV. Dies entspricht einer Genauigkeit von 7.3%.

Abstract

In a new high-precision experiment at the Paul Scherrer Institute (PSI), the hadronic shift (ϵ_{1s}) and width (Γ_{1s}) were remeasured (PSI-Experiment R-98-01). The measured quantities ϵ_{1s} and Γ_{1s} are directly connected to the pion-nucleon isospin scattering lengths. The precisely determined scattering lengths can be confronted with recent work of effective field theories defined in the low-energy limit of quantum chromodynamics (QCD), such as e. g. chiral perturbation theory (ChPT). In addition, Γ_{1s} is connected to the pion-nucleon coupling constant $f_{\pi N}$. A precisely known value for $f_{\pi N}$ allows an accurate determination of the Goldberger-Treiman discrepancy, which constitutes a measure of chiral symmetry breaking.

The shift ϵ_{1s} is given by the difference between the measured X-ray energy and the purely electromagnetic value. Γ_{1s} is obtained by deconvolution of the measured line-shape consisting of the hadronic broadening, the instrumental response function and Doppler-broadening. Doppler-broadening is caused by the conversion of the deexcitation energy from the Coulomb deexcitation into kinetic energy of pionic atoms.

The measurements were performed using the high-intensity pion beam available at the PSI accelerator facility. X-rays emitted during the transition into the ground state of pionic hydrogen, i. e., the $\pi^- p_{np \rightarrow 1s}$ transitions with $n = 2, 3, 4$, were measured. In contrast to the energy of these radiative transitions (a few keV), the hadronic effects are only of the order of a few eV. Thus, in order to access such small effects, the use of a high-resolution crystal spectrometer is indispensable.

With a cyclotron trap, the pions were guided into a cryogenic hydrogen gas target where pionic hydrogen ($\pi^- p$) atoms are formed. X-rays emitted from the $\pi^- p$ atoms were reflected at the high-resolution crystal spectrometer onto a large area position-sensitive detector.

The instrumental response function was measured using narrow X-ray transitions from highly ionised atoms produced in an electron cyclotron resonance ion trap.

The kinetic energy distribution of pionic atoms was approximated by a model using box-like distributions. This approach was verified in a measurement of the $3p \rightarrow 1s$ X-ray transition in muonic hydrogen ($\mu^- p$). Unlike pions, muons do not experience the strong interaction and thus, the line-shape of the emitted X-rays is very sensitive to Doppler-broadening.

Together with the measured instrumental response function, this model for the kinetic energy distribution was used in an analysis method to extract Γ_{1s} . This analysis method was developed in this work and first applied to the $4p \rightarrow 1s$ transition in pionic hydrogen. The results reads $\Gamma_{1s} = 765 \pm 56$ meV and corresponds to an accuracy of 7.3%.

Contents

1	Introduction	1
1.1	Exotic atoms	1
1.1.1	Pion-nucleon interaction	2
1.2	Pionic hydrogen experiments	3
2	Pionic hydrogen	7
2.1	Formation of exotic atoms	7
2.2	Atomic cascade of pionic hydrogen	9
2.2.1	Coulomb deexcitation	13
2.2.2	Prediction for the kinetic energy distribution	14
2.2.3	Approximative model for the kinetic energy distribution	16
2.2.4	Muonic hydrogen	17
3	Pion nucleon interaction	19
3.1	QCD at low energy	20
3.2	π N scattering lengths	24
3.3	Relation of scattering lengths to ϵ_{1s} and Γ_{1s}	28
3.3.1	Corrections $\delta_{\epsilon,\Gamma}$	28
3.4	π N coupling constant	30
3.5	π N sigma term	30
3.6	Pionic deuterium	31
4	Experimental setup and data processing	33
4.1	The experimental approach	33
4.1.1	Pion production	33
4.1.2	Cyclotron trap	35
4.1.3	Cryogenic target	37
4.1.4	Crystal spectrometer	38
4.1.5	Geometry of the spectrometer setup	42
4.1.6	CCD detectors	43
4.2	Data processing	47

4.2.1	Cluster analysis	47
4.2.2	ADC-cuts	47
4.2.3	Bad pixel map	48
4.2.4	Curvature correction	48
5	The spectrometer response function	51
5.1	The Electron Resonance Ion Trap – ECRIT	51
5.1.1	Experimental setup	52
5.1.2	Experimental procedure	53
5.2	Determination of the spectrometer response function	54
5.2.1	Definition of the spectrometer focus	57
5.2.2	Determination of the additional Gaussian broadening	58
5.2.3	Results for the additional Gaussian broadening	60
5.2.4	The spectrometer response function	61
6	Analysis and results	63
6.1	Analysis	63
6.1.1	Free fit to the data	63
6.1.2	Effect of statistics on the fit-result	66
6.1.3	Monte Carlo studies	68
6.1.4	Analysis strategy	70
6.2	Results	73
6.2.1	Bias for $4p \rightarrow 1s$ 2002	73
6.2.2	Bias for $4p \rightarrow 1s$ 2006	73
6.2.3	Final value for Γ_{1s}	76
7	Summary and Outlook	79
7.1	Summary	79
7.2	Outlook	80
A	File lists	83

1 Introduction

1.1 Exotic atoms

Exotic atoms are atoms where the electron is replaced by another negatively charged particle, like a pion π^- (Figure 1.1). The pion is captured in the Coulomb field of the nucleus into a highly excited atomic state and deexcites to the ground state via various processes comprising the so-called atomic cascade.

In general, the cascade is dominated by collisional processes such as for instance the Auger effect and the Coulomb deexcitation. The Coulomb deexcitation is of special interest, since the energy released in the deexcitation process is converted into kinetic energy of the involved pionic atoms and therefore considerably changes their kinetic energy distribution. Only at the final stages of the cascade, radiative deexcitation starts to become relevant. The measurement of X-rays emitted at this stage allows a direct investigation of properties of pionic atoms.

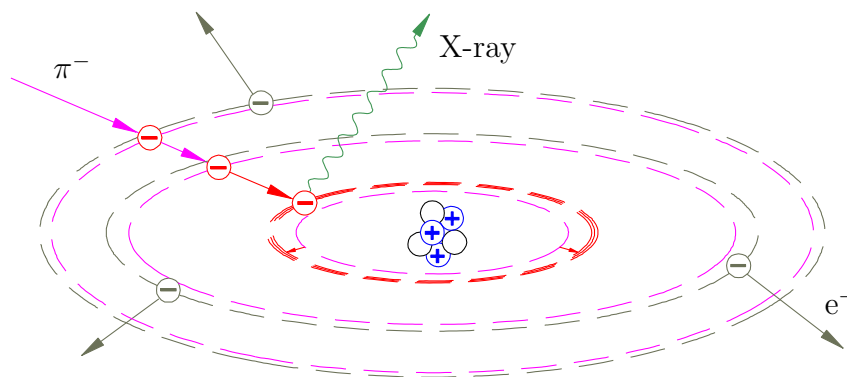


Figure 1.1: Schematic drawing of a pionic atom. After the capture of a pion in a high lying orbit, pionic atoms deexcite to lower states by emitting electrons via the internal Auger effect. For lower states, radiative deexcitation dominates under the emission of X-rays.

1.1.1 Pion-nucleon interaction

Due to its hadronic nature, the pion – once arrived in the ground state – interacts with the nucleon via the strong interaction. This causes a shift ϵ_{1s} and a broadening Γ_{1s} of the atomic $1s$ state, influencing the energy and line shape of X-rays emitted during transitions into the ground state. The strong interaction shift is usually defined as the difference between the measured transition energy and the value calculated within quantum electrodynamics (QED) $\epsilon_{1s} := E_{\text{exp}} - E_{\text{QED}}$. Hence, pionic atoms allow the study of the pion-nucleon interaction at threshold. In contrast to scattering experiments, measurements directly at threshold render a difficult extrapolation to zero energy unnecessary.

A relation between the measurable quantities ϵ_{1s} and Γ_{1s} and the s-wave scattering amplitude of the pion-nucleon scattering was derived by Deser, Goldberger, Baumann and Thirring (DGBT) [1] and it reads

$$-\epsilon_{1s} + i\Gamma_{1s} = \frac{2\pi}{\mu} f_0^{\pi^-p}(0) |\Psi_{1s}(0)|^2. \quad (1.1)$$

Here μ is the reduced mass of the system and $|\Psi_{1s}(0)|^2 = \alpha^3 \mu^3 / \pi$ denotes the square of the Coulomb wave function of the atom at the origin and therefore is a measure for the probability that the pion and the nucleon are close to each other. α is fine structure constant. The scattering amplitude at threshold, $f_0^{\pi^-p}(0)$, is related to the hadronic s-wave scattering lengths.

The comparison of precise experimental values for the scattering lengths, to precise predictions from low-energy effective field theories such as e.g. chiral perturbation theory (ChPT), allows direct studies of the properties of the low-energy QCD. ChPT is formulated in the so-called chiral limit (vanishing quark masses) and exploits the symmetry properties of QCD.

Additionally, the values for the scattering lengths are used as input for the determination of further important parameters of low-energy QCD such as the pion-nucleon coupling constant, determining the strength of the coupling of a pion to a nucleon. From the accurately known pion-nucleon coupling constant in turn the Goldberger-Treiman discrepancy is determined, which is a measure of chiral symmetry breaking due to the non-vanishing quark-masses.

Experiments with exotic atoms Pions constitute the best laboratory for testing the approach provided by ChPT, since pions are light particles including only u and d quarks. For the pion-pion system, an experimental test will be provided by the DIRAC experiment [2], which measures the lifetime of pionium ($\pi^+\pi^-$). The pion nucleon system (π^-N), subject of this work, will allow accurate tests of Heavy Baryon ChPT (HBChPT). HBChPT is an extension of ChPT and includes nucleons.

Apart from pionic systems, the DEAR collaboration measured the shift and width of the ground state in kaonic hydrogen (K^-p) at the DAΦNE accelerator facility [3]. This system is of special interest, since kaons include strange quarks. However, this experiment is very challenging due to the low intensity kaon beam available and the results of the DEAR experiment are expected to be improved by the SIDDHARTA experiment [4].

1.2 Pionic hydrogen experiments

The possibility of investigating the pion-nucleon interaction directly at threshold, gave pionic hydrogen experiments a long history. First experiments were performed already in the 1970s at CERN [5], where a gas proportional counter was mounted directly at the hydrogen gas target.

Following this experiment, all experiments had a similar setup: After slowing down the pions and stopping them in a gas target, the emitted X-rays are reflected by a Bragg spectrometer and finally they are detected at a position sensitive detector. The usage of Bragg crystals is essential in order to obtain high energy resolution.

In 1985 an experiment to extract the strong interaction shift and width of pionic hydrogen was started at the Paul-Scherrer-Institute [6], measuring the $3p \rightarrow 1s$ X-ray transition. The final value given for the shift is

$$\epsilon_{1s} = +7.108 \pm 0.047 \text{ eV},$$

(using the pionic argon $K\alpha$ transition as calibration) and for the width

$$\Gamma_{1s} = 868 \pm 78 \text{ meV}.$$

This amounts in an error of 0.7% for the shift and 9% for the width.

To increase the accuracy of ϵ_{1s} and Γ_{1s} , a new experiment was proposed in 1998 [7]. The goal of this new pionic hydrogen experiment is the determination of the hadronic energy shift ϵ_{1s} and width Γ_{1s} with an accuracy of 0.2% and 2%, respectively. This requires several improvements on both, the experimental and the analysis side.

The new pionic hydrogen experiment was set up at PSI using the high pion flux available at the PSI accelerator facility. The main components of the experimental setup and their main function are:

Cyclotron trap: The cyclotron trap consists of a superconducting split coil magnet, producing a weakly focusing axial \vec{B} -field. The pion beam is moderated by built in plastic degraders and led into the target cell. In this device the stop efficiency is increased by a factor of 200, compared to a linear stop arrangement.

Cryogenic target: In the target gas, pionic hydrogen atoms are formed and pionic hydrogen X-rays are emitted. The cryogenic target cell allowed to cover a high density range for the hydrogen gas.

Crystal spectrometer: The emitted X-rays are energy-analysed with a high resolution ($\Delta E/E = 10^{-4}$) Bragg spectrometer using large spherically bent crystals.

CCD detector: The reflected X-rays are measured at a large area CCD detector with good quantum efficiency for X-rays in the range of 2-3 keV. Significant background suppression is achieved from the two-dimensional pattern recognition.

The measurements were started with an engineering run end of 2000. In the years 2001 and 2002 the three different pionic hydrogen transitions, the $4p \rightarrow 1s$, $3p \rightarrow 1s$ and $2p \rightarrow 1s$, were measured.

In 2003, the final value for the shift was given in [8] and it reads

$$\epsilon_{1s} = +7.120 \pm 0.008_{-0.009}^{+0.008} \text{ eV},$$

which amounts in an error of 0.2%. It was extracted from the $3p \rightarrow 1s$ pionic hydrogen transition using the pionic oxygen $6h \rightarrow 5g$ transition for energy calibration.

For Γ_{1s} , only an upper constraint ($\Gamma_{1s} \leq 850 \text{ meV}$) was given in [8]. This is mainly due to the lack of information on the kinetic energy distribution of the atoms leading to Doppler broadening of the spectra at the time the analysis was performed.

To increase the accuracy of the hadronic width Γ_{1s} , special attention was turned to the instrumental response function and to the influence of the Doppler broadening caused by Coulomb deexcitation.

In 2002, first measurements in order to systematically determine the instrumental response function using narrow X-ray transitions from highly ionised atoms produced in an electron cyclotron resonance ion trap (ECRIT) were performed. These measurements were continued and completed in 2005.

In 2004, a measurement of muonic hydrogen was performed. Unlike pions, muons do not interact strongly and that way allow detailed studies of the influence the kinetic energy distribution of the muonic atoms has on the line-shape of the emitted X-rays.

Data taking was completed by a measurement of pionic deuterium and a second measurement of the $4p \rightarrow 1s$ transition in 2006.

During all measurement periods much effort was put into the improvement of the concrete shielding between the X-ray source (cyclotron trap) and the Bragg spectrometer.

The development of the necessary analysis strategy on the basis of the $4p \rightarrow 1s$ pionic hydrogen X-ray transition is the main task of this work. The choice of the $4p \rightarrow 1s$ transition is a consequence of the fact, that it is least influenced by Doppler broadening.

The document is organised as follows. Chapter 2 gives a short introduction to the atomic cascade with emphasis on the status of the understanding of the kinetic energy distribution of the pionic atoms. In chapter 3, the pion-nucleon interaction and important quantities such as low-energy scattering lengths and their relation to experimentally accessible quantities is outlined. Chapter 4 introduces the components of the experimental setup. The measurement and extraction of the instrumental response function is described in chapter 5. Chapter 6 gives a comprehensive description of the analysis method for extracting the hadronic $1s$ width in pionic hydrogen. Concluding remarks are given in chapter 7.

2 Pionic hydrogen

2.1 Formation of exotic atoms

Exotic atoms are systems in which a negatively charged particle (π^- , μ^- , K^- , \bar{p}) is captured by the Coulomb field of the nucleus $A(Z, N)$ (see also Figure 1.1). Their existence was predicted in the 1940s [9–12] and first experimental evidence was found from the observation of Auger electrons in photographic emulsions [13].

In leading order, given by the Bohr model, the binding energy E_B and the Bohr radii r_B and hence the expectation values of orbit radii $\langle r_n \rangle$ of captured particles are proportional to the reduced mass $\mu_{\text{red}} = \frac{m_{\text{nucl}} \cdot m_{x^-}}{m_{\text{nucl}} + m_{x^-}}$ of the system and $1/\mu_{\text{red}}$, respectively:

$$E_B = \frac{\mu_{\text{red}} c^2 \alpha^2 Z^2}{2n^2}, \quad (2.1)$$

$$r_B = \frac{\hbar c}{\mu_{\text{red}} c^2 \alpha Z}, \quad (2.2)$$

$$\langle r_n \rangle = r_B \cdot [3n^2 - l(l+1)/2], \quad (2.3)$$

with the reduced Planck constant \hbar , the vacuum speed of light c , the fine structure constant α , nuclear charge Z , the angular momentum l and principal quantum number n .

Since the captured particles are heavier than the electron, the binding energy of the exotic system is increased by about a factor m_{x^-}/m_e (m_e is the mass of the electron) and the size of the exotic atom decreases by the same factor. Even for lightest particles, the muon or the pion, the size of the formed exotic atom is rather at the nuclear than at the atomic scale.

For capture, the particle has to be slowed down to kinetic energies of a few tens of eV. This deceleration allows the particle to be captured in a highly excited state with a principal quantum number $n \sim \sqrt{\mu_{\text{red}}/m_e}$ and statistically distributed initial angular momentum l . For the distribution of l mostly the modified statistical distribution $(2l+1)^{\alpha l}$ is used, where α is fitted to the data and is usually $|\alpha| < 0.2$. After capture, the formed exotic atoms deexcite to lower lying states by a number of processes (external Auger effect, radiative transitions, Coulomb deexcitation etc.). These processes constitute the so-called atomic cascade (see Figure 2.1 for a schematic view). Finally, the cascade is terminated by nuclear capture or weak decay of the particle x^- .

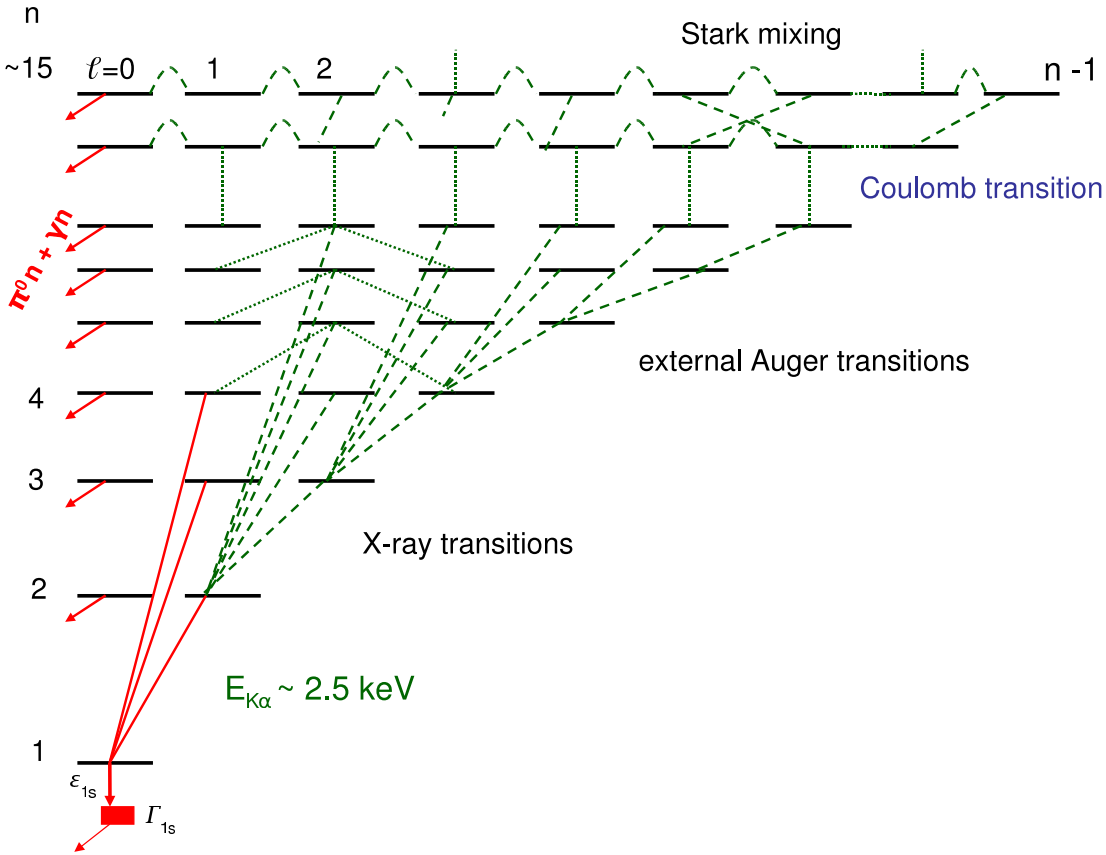


Figure 2.1: Scheme of the atomic cascade in pionic hydrogen. Pionic hydrogen is formed with the capture of pions in highly excited states. In the upper part of the cascade the dominant deexcitation process is the Coulomb deexcitation. In the intermediate stage $n \sim 8$ the Auger deexcitation with $\Delta n = 1$ is dominant. The final part of the cascade $n < 6$ is characterised by a competition between Auger, Coulomb, and radiative deexcitation and nuclear reactions from the s states.

The investigation of strong interaction was the main motivation for studying exotic atoms, since exotic atoms have binding energies in the keV range and therefore allow experiments equivalent to scattering at vanishing relative energy. This offers the possibility for studying the hadron-nucleon interaction at threshold, without the need of extrapolation, as necessary for the low-energy scattering data.

The strong interaction influences the atomic s -levels throughout the cascade. However, at the final stage of the cascade, where the captured particle closely approaches the nucleus, this influence becomes observable. The caused shift ϵ_{1s} (compared to the purely electromagnetic case) and the decrease of the life time of the ground-state, which leads to a broadening Γ_{1s} of X-ray transitions into the $1s$ -state, are experimentally accessible

Process	Example
Radiative transitions:	$(x^-p)_{nl} \rightarrow (x^-p)_{n',l-1} + \gamma$
Stark transitions:	$(x^-p)_{nl} + H_2 \rightarrow (x^-p)_{nl'} + H_2^*$
External Auger effect:	$(x^-p)_{nl} + H \rightarrow (x^-p)_{n'l'} + p + e^-$
Coulomb transitions:	$(x^-p)_{nl} + H_2 \rightarrow (x^-p)_{n'l'} + H + H, \quad n' < n$
Elastic scattering:	$(x^-p)_{nl} + H_2 \rightarrow (x^-p)_{nl} + H_2^*$
Nuclear reaction:	$(\pi^-p)_{nl=0} + H \rightarrow \pi^0 + n, \gamma + n$
Weak decay:	$\pi^- \rightarrow \mu^- + \bar{\nu}_\mu$
Molecular states:	$(\pi^-p) + H_2 \rightarrow (\{\pi^-pp\}^* p e e)^*$

Table 2.1: Summary of different cascade processes – with examples – in exotic hydrogen.

and allow a direct investigation of the effects of the strong interaction.

2.2 Atomic cascade of pionic hydrogen

For atoms with $Z > 2$, the atomic cascade is mainly comprised of the Auger emission of electrons (internal Auger effect) and the radiative decay. For pionic hydrogen, however, additional effects, such as Stark mixing and Coulomb deexcitation play an important role. Since exotic hydrogen is electrically neutral, it is able to approach closely the nuclei of the surrounding atoms and experiences their Coulomb field. These collisions, have a substantial effect on the further development of the atomic cascade. In Table 2.1 a summary of the processes comprising the atomic cascade in exotic hydrogen is given. In general, the whole atomic cascade is characterised by a competition between the different processes listed in Table 2.1.

The cascade is dominated by collisional processes. The main collisional processes important for the understanding of the atomic cascade are the Stark mixing, the external Auger effect and the Coulomb deexcitation. The cross-sections of non-radiative transitions are of geometrical order, i. e. $\sigma_{\text{coll}} \approx \langle r_n \rangle^2$, thus collisional processes are proportional to the target gas density. Even at low densities, the collisional deexcitation dominates over the radiative transitions through the whole cascade, except for the lowest part with $n = 2, 3$. At low n , radiative deexcitation is the dominant process.

Stark mixing is characterised by transitions among the l -sub-levels with the same n and is a very fast process. In the external Auger effect, the transition energy is mainly carried away by the emitted electron. The dominating process in the initial stage of the atomic cascade is the Coulomb deexcitation. The transition energy gained from this process is

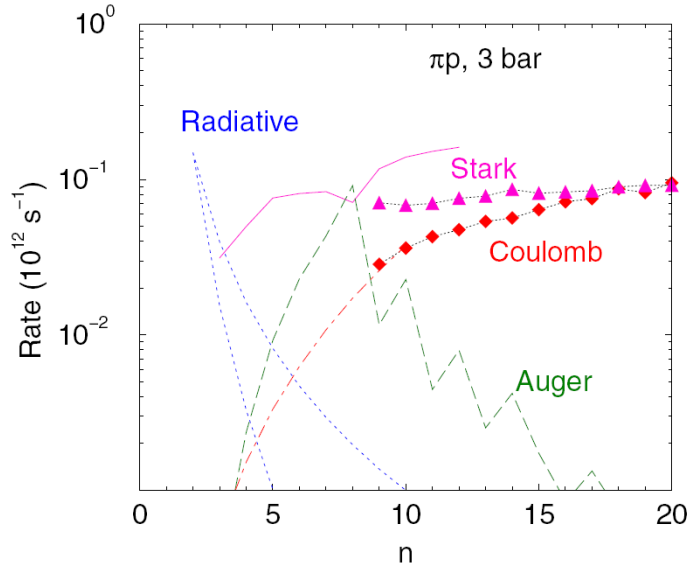


Figure 2.2: Transition rates for pionic hydrogen with the lab kinetic energy $T = 1$ eV as function of the principal quantum number in a gaseous H-target at 3 bar. The figure is taken from [14].

shared among the colliding particles, which results in a substantial acceleration. A deceleration, however, is caused by elastic, inelastic and Stark collisions. Figure 2.2 displays an example of the n -dependence of the atomic cascade for pionic hydrogen.

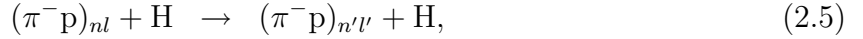
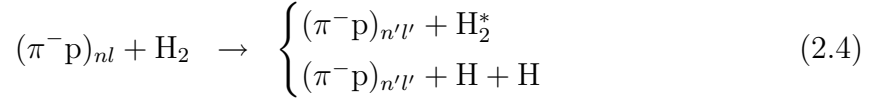
Since collisional processes significantly change the velocity of exotic atoms during the deexcitation, it is very important to include these effects in theoretical calculations of cascade effects. The standard cascade model (SCM) for exotic hydrogen atoms [15, 16] developed in the 60–80th was able to describe the basic features of the atomic cascade. However, the cascade rates are calculated for a fixed value of the kinetic energy T only, with T being treated as a fit parameter.

A recently developed cascade model, the so-called *extended standard cascade model (ESCM)* [17–19] was developed in order to overcome this limitation. It includes all processes from the SCM and, in addition, takes into account the evolution of the kinetic energy distribution during the cascade.

Presently, the understanding of the life history of a π^-p atom (which is the exotic system of interest throughout this paper) can be divided into three parts, see reference [19]:

Upper part ($n > 8$): The pionic atoms are formed by atomic capture in high orbits with a broad distribution of the principal quantum number around $n = 15$, see reference [20]. A realistic median initial kinetic energy of the π^-p is 0.5 eV, as suggested in [17]. For $n > 8$ the deexcitation mainly takes place via Coulomb and

Stark collisions:

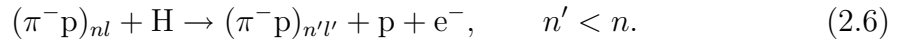


with $n' < n$ for Coulomb and $n' = n$ in Stark collisions.

Cascade calculations for muonic hydrogen have shown, that with increasing n the cross-section for Coulomb deexcitation increases and that the cross-section for the molecular target H_2 is larger by a factor of about 2–3, compared with the one of atomic hydrogen. Moreover, $\Delta n = 1$ transitions dominate for atomic hydrogen, whereas transitions with $\Delta n > 1$ are dominant for the molecular case.

Considering the Stark collisions, the cross-sections with molecular hydrogen are less than twice the atomic ones. This is due to two reasons. First, the molecular screening effect in H_2 (the electrical fields of the two hydrogen atoms cancel each other). Second, the Coulomb cross-section makes up a large fraction of the total cross-section, which leads to a decrease for the Stark cross-section. After completing this stage, most $\pi^- \text{p}$ atoms are accelerated to kinetic energies of a few eV. For a detailed discussion the reader is referred to [18].

Intermediate part ($7 \leq n \leq 8$): The intermediate part of the cascade is dominated by external Auger transitions:



Auger deexcitation occurs via the ionisation of an encountered hydrogen atom. In this process the increase of the binding energy of the pionic hydrogen system is converted into kinetic energy of the emitted e^- . Transitions with $\Delta n = 1$ and $\Delta l = -1$, i. e., transitions with minimal possible energy difference, are favoured ($\Gamma_{\text{Aug}} \propto 1/\sqrt{\Delta E}$), see reference [15]. The cross-sections for Auger transitions strongly increase with n , until a critical level n_c is reached. n_c is the largest n for which a $\Delta n = 1$ transition can ionise an encountered hydrogen atom. For $n > n_c$ only transitions with $\Delta n > 1$ are energetically possible and hence the Auger cross-section decreases with higher n (Figure 2.2).

Lower part ($2 \leq n \leq 6$): The radiative E1 transition with $\Delta l = \pm 1$



is the main process for low n . However, since Stark transitions are very important as well at this stage of the cascade [17–19], the population of the nl sub-states at

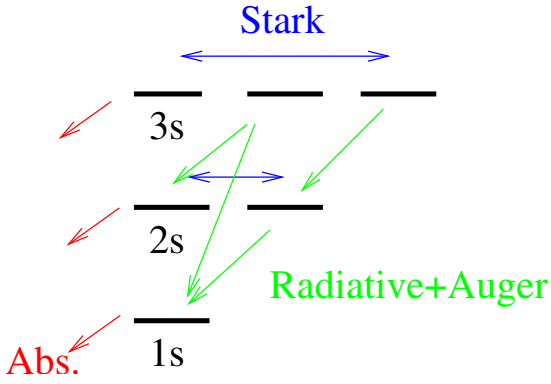


Figure 2.3: Cascade model for the final part of the cascade [21]. The (π^-p) atoms deexcite radiatively and via the external Auger effect, while the Stark effect leads to a mixing of the l -sub-states, where an s -state admixture causes nuclear reaction. Figure taken from [21].

a given level n is modified (see also Figure 2.2). This leads to an increase of the relative importance of the charge exchange reaction

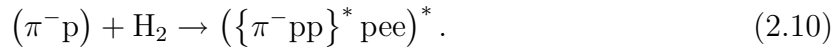


and the radiative capture



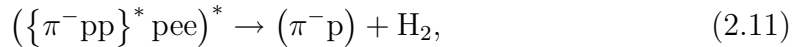
which occurs in s -states where the pion wave function significantly overlaps with the nuclear region. These reactions reduce the yield of the radiative transitions [21]. Although the rate for Coulomb deexcitation is lower than the one for Auger deexcitation at this stage of the cascade, its effect on the kinetic energy distribution of the pionic hydrogen atoms, is far more pronounced because of the large recoil momentum. In fact, good understanding of the Coulomb deexcitation and its effect on the line shape is of crucial importance for the determination of the width of the ground state in pionic hydrogen.

Molecular states It is known from muon catalysed fusion (μCF), see e.g. [22], that during collisions of a muonic hydrogen atom and a H_2 molecule a metastable hybrid molecule can be formed. The same is expected for pions:

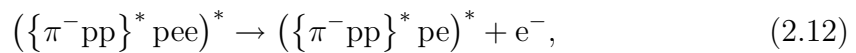


The complex $(\{\pi^-pp\}^* pee)^*$ can decay through several channels (see for instance [23]):

- back to the initial channel



- Auger decay, by emitting an electron



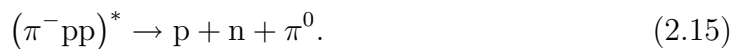
- radiative decay, by emitting a photon



- Coulomb decay, by emitting one of the protons



- and nuclear absorption



The Coulomb decay can take place either directly, or via an intermediate Auger decay, or radiative decay. The binding energies of these various molecular states have been calculated in [20]. They were found to be slightly different, compared to the ones in the atomic case. Hence the energy of X-ray transitions from such a molecular state is shifted, compared to the same X-ray transition in an isolated $\pi^- p$ atom and must be considered when extracting the hadronic shift ϵ_{1s} .

Pressure dependence of the atomic cascade The molecular formation as well as the Coulomb deexcitation are scattering processes, thus they depend on collisions, i. e., on the density. Therefore an important task of the current experiment was to check, whether or not a pressure dependence of the measured X-ray transitions can be observed.

A possible effect of molecular formation was studied in detail by measuring the pressure dependence of the $3p \rightarrow 1s$ pionic hydrogen line energy [8]. The main goal in [8] was the determination of the strong interaction shift ϵ_{1s} of the ground state in $\pi^- p$. If there was a pressure dependence of the atomic cascade and X-ray transitions would occur from molecular states, this would affect the value for the shift.

The measurements were performed over a large range of hydrogen gas densities (from 3.5 bar – very low rate expected – up to ~ 700 bar – liquid hydrogen). However, no pressure dependence of the $\pi H(3p \rightarrow 1s)$ energy was found within the experimental accuracy and therefore it was concluded, that molecular states once formed, deexcite via other mechanisms than radiative deexcitation.

The final value for the strong interaction shift ϵ_{1s} determined in [8] is

$$\epsilon_{1s} = +7.120 \pm 0.008_{-0.009}^{+0.008} \text{ eV}. \quad (2.16)$$

2.2.1 Coulomb deexcitation

Coulomb deexcitation (see (2.4) and (2.5)) has been first directly observed by a Doppler broadening of time-of-flight distributions of neutrons from the charge-exchange reaction

$\pi^-p \rightarrow \pi^0n$ [24–26]. Doppler contributions from several radiation-less transitions $n \rightarrow n'$ ($n' < n$) up to 209 eV (corresponding to $3 \rightarrow 2$ Coulomb transitions) have been identified. The influence of Coulomb deexcitation on the line shape of radiative transitions into the ground state in pionic hydrogen will be similar to the ones observed in the neutron time-of-flight, but the kinetic energy distribution could be very different. Neutron time-of-flight experiments such as those described in [24,25] are only sensitive to atomic ns -states. The radiative transitions into the ground state occur from np -states, which can be populated via $l \gg 1$ momentum states only.

In an $n \rightarrow n'$ Coulomb transition the energy release is given by

$$\Delta E_{n \rightarrow n'} = \frac{\mu_{\text{red}}}{2} \left(\frac{1}{n'^2} - \frac{1}{n^2} \right), \quad (2.17)$$

where μ_{red} is the reduced mass of the π^-p atom. At low n only $\Delta n = 1$ transitions are expected to be important. Thus the characteristic kinetic energies of the highly energetic π^-p atoms are given by

$$T_n = \frac{m_{\text{H}}}{m_{\text{H}} + m_{\pi^-p}} \Delta E_{n+1 \rightarrow n}, \quad (2.18)$$

with m_{H} being the mass of the hydrogen atom and m_{π^-p} the mass of the π^-p atom. Equation (2.18) yields the energies of 18 eV, 34 eV, 73 eV and 209 eV for $n = 5, 4, 3$ and 2, respectively.

State dependence of the line shape In the year 2002 X-ray spectra from the $4p \rightarrow 1s$, $3p \rightarrow 1s$ and $2p \rightarrow 1s$ transitions in pionic hydrogen were measured at PSI. The effect of the Doppler broadening on the three transitions is expected to be different, because the kinetic energy distributions are not the same for the different n levels. For instance, the $3 \rightarrow 2$ Coulomb transition gives rise to a 209 eV component, which is only important for the $2p \rightarrow 1s$ line. However, atoms that go through the $4 \rightarrow 3$ Coulomb transition and thereby gain 73 eV, affect the $3p \rightarrow 1s$ transition as well as the $2p \rightarrow 1s$, because they can reach the $2p$ state via the $3d \rightarrow 2p$ radiative transition without losing kinetic energy. The same is true for the $5 \rightarrow 4$ Coulomb transition, which is supposed to affect all three measured spectra.

2.2.2 Prediction for the kinetic energy distribution

As mentioned earlier, the *extended standard cascade model (ESCM)* [19] takes into account for the first time, the evolution of the kinetic energy distribution of the pionic atoms during the cascade.

The ambitious goal of the ESCM is a full ab initio calculation of the kinetic energy distribution of the π^-p atoms at the instant of the emission of an X-ray. This kinetic energy

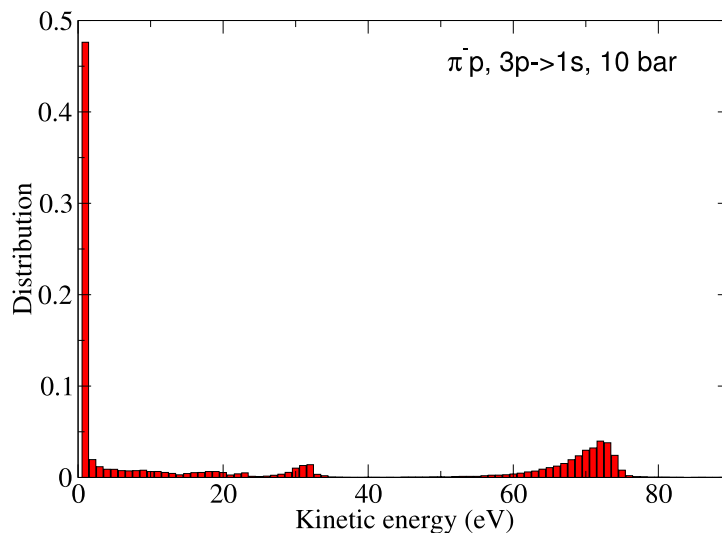


Figure 2.4: The kinetic energy distribution of the π^-p atoms at the instant of the $3p \rightarrow 1s$ transitions, as is predicted by the ESCM. Figure taken from [21].

distribution could then be used in the extraction of the strong interaction width from the measured pionic hydrogen data. In order to reach that goal, the cross sections for the collisional processes must be known reliably, which is a very challenging task. For example, a quantitative understanding of the molecular formation process and the subsequent break-up is necessary, in order to make predictions for the relative rates of absorption, Coulomb, radiative and Auger transitions.

Instead, a method was proposed in [19], which distinguishes between a low and high energy component, i. e., high n and low n part, respectively, of the kinetic energy distribution of the π^-p atoms. The low energy component is treated as a "black box", since the present understanding of the processes involved is not yet sufficient for accurate cascade calculations. Hence, the calculations are only performed for the high energy / low n fraction of the π^-p atoms. The energy chosen to separate the low from the high energy component is set to 10 eV [19].

The method in principle follows the life history of a π^-p atom, starting from an initial distribution of the quantum numbers n and l and kinetic energy. The quantum states of the π^-p atoms are changed by both, collisional processes (i. e., Stark collisions, external Auger effect) and non-collisional processes (i. e., radiative deexcitation and nuclear absorption from the ns -states), which also leads to a broadening of the characteristic kinetic

energy values, calculated in (2.18). Coulomb deexcitation, which is expected to take place from the low energy component, is not included in the cascade calculation.

Finally, with the cascade program briefly discussed here, the kinetic energy distribution at the instant of an $np \rightarrow 1s$ transition in pionic hydrogen can be calculated. Figure 2.4 shows the kinetic energy distribution at the pressure 10 bar at the instant of the $3p \rightarrow 1s$ transition originating from the 34 eV Coulomb component with $n = 4$.

In principle such a kinetic energy distribution could be used in the analysis of measured π^-p spectra, by folding it with the response function of the setup and performing a χ^2 analysis and that way extracting the Lorentz width. However, as will become clear below (section 2.2.4), it turned out, that this is not yet possible. Therefore, a model describing the kinetic energy distribution independently from cascade calculations is necessary.

2.2.3 Approximative model for the kinetic energy distribution

The kinetic energy distribution of the π^-p atoms can be approximated by a model using so-called Doppler-boxes.

Starting from the calculated values for the kinetic energy, a discrete kinetic energy distribution of the atoms at the instant of the emission of an X-ray can be constructed. In this model, each transition corresponds to a δ -like peak, i. e., $\delta(T - T_0)$, where T_0 is one of the values calculated with (2.18). The relation between the velocity and the kinetic energy is given by

$$v_0 = \sqrt{\frac{2T_0}{m_{\pi^-p}}}. \quad (2.19)$$

From this (discrete) kinetic energy distribution and, assuming an isotropic velocity distribution, a "box-like" velocity distribution is obtained for each Coulomb transition (Figure 2.5). For details see also [27].

The influence of collisions on the π^-p atoms prior to the occurrence of a radiative deexcitation is modelled by changing the form of the kinetic energy distribution from a δ -like to a box-like, reaching up to a maximal kinetic energy as given by (2.18). Figure 2.6 illustrates the relation between a box-like kinetic energy distribution and the corresponding velocity distribution. The broad kinetic energy region can be regarded as several discrete (δ -like) peaks, where each of these kinetic energy peaks corresponds to a "box-like" velocity distribution. Finally this leads to a "trapezoid-like" velocity distribution also shown in Figure 2.6. Summing up, for each transition considered, the kinetic energy distribution of the π^-p atoms at the instant of the radiative deexcitation can be approximated.

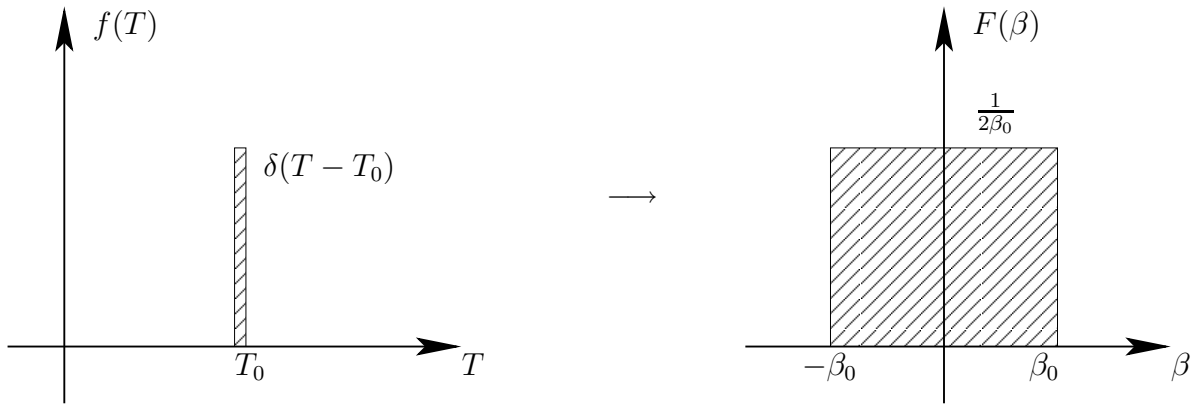


Figure 2.5: Illustration of the relation between a δ -like kinetic energy distribution and the resulting velocity distribution.

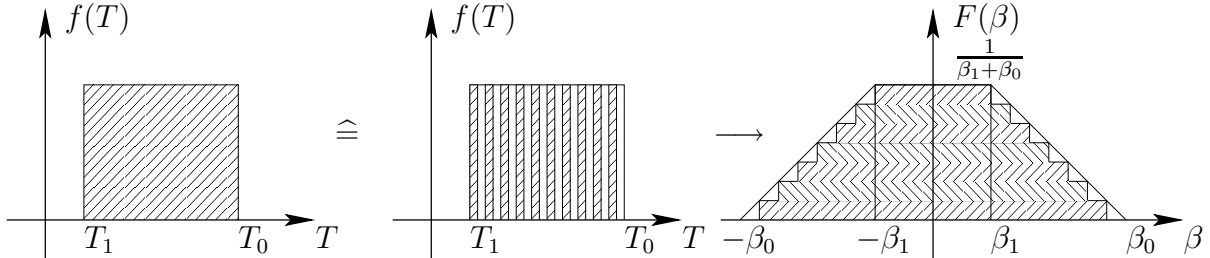


Figure 2.6: Illustration of the relation between a box-like kinetic energy region and the resulting velocity distribution.

2.2.4 Muonic hydrogen

A crucial check of the predictions for the kinetic energy distribution from the cascade model, was the measurement of the $3p \rightarrow 1s$ transition in muonic hydrogen (μ^-p). A detailed description of the measurement and the subsequent analysis can be found in [28]. Unlike pions, muons do not experience the strong interaction and hence, the instrumental response function given, the broadening of the measured X-ray lines is only due to cascade processes, in particular due to the Coulomb deexcitation. Thus μ^-p constitutes an ideal system to verify the prediction of the cascade model for the velocity distribution. In addition, the measurement of muonic hydrogen constitutes the first direct measurement of the splitting and relative population of the hyperfine levels of the ground state in μ^-p . The main result from the analysis of the $3p \rightarrow 1s$ transition in μ^-p is, that, by using the theoretically predicted weights for the different energy components in the kinetic energy distribution, the theoretical prediction for the hyperfine splitting and for the triplet to singlet population in muonic hydrogen can not be reproduced. This is especially true for

the low energy component, if the approach with broad distributions, presented in section 2.2.3, concentrated around the characteristic energies for the Coulomb transitions is used. In fact, in order to be able to reproduce the theoretical prediction for the hyperfine splitting and population of the hyperfine levels of the ground state in μ^-p , the relative weight of the low energy component must be of the order of 60% of the total kinetic energy distribution. This clearly contradicts the prediction from the cascade code, which at present gives 30% (up to 2 eV) and hence reveals the importance of the low energy component of the atomic cascade. In conclusion, the prediction of the cascade calculations, performed within the framework of the ESCM, at present cannot reproduce the μ^-p (or π^-p [29]) kinematics. Especially, for the high n part of the cascade with $n > 8$, which represents the low energy component, the prediction is far off. In future this may be overcome by including molecular formation into the cascade code.

Presently, the approach with box-like kinetic energy distributions extending up to the characteristic kinetic energy values, given by (2.18) and schematically shown in Figure 2.6 must be used [28] to extract the hadronic broadening.

3 Pion nucleon interaction

Quantum chromodynamics (QCD) is the theory describing the strong interaction of coloured quarks and gluons. QCD is, like quantum electrodynamics (QED), a gauge theory and is part of the $SU(3) \otimes SU(2) \otimes U(1)$ standard model. Due to the huge success and the predictive power of QED, QCD is also constructed by demanding a local gauge invariance.

The main difference of these two theories is, that QCD is behaving differently at low and large distances. Only at small distances, i. e., high momentum transfer, the QCD (running) coupling constant α_s becomes small and gives rise to the so called asymptotical freedom of QCD and hence conventional perturbation theory (expansion in the coupling constant) is possible.

For low energies, however, this perturbation expansion does not converge, because here α_s is of the order 1. Hence other tools are necessary in order to describe QCD at low energy. Chiral perturbation theory (ChPT) [30, 31] is such a tool. ChPT is an effective field theory, exploiting the symmetry properties of QCD in the limit of vanishing quark masses (the so called chiral limit).

The QCD Lagrangian is constructed on the basis of the symmetry group $SU(3)$ and it contains a gluonic part and a fermionic part:

$$\mathcal{L}^{\text{QCD}} = \mathcal{L}_{\text{fermion}}^{\text{QCD}} + \mathcal{L}_{\text{gluon}}^{\text{QCD}}, \quad (3.1)$$

with

$$\mathcal{L}_{\text{fermion}}^{\text{QCD}} = \sum_{f=1}^{n_f} \bar{q}_f (i\gamma_\mu D^\mu - m_f) q_f, \quad (3.2)$$

$$\mathcal{L}_{\text{gluon}}^{\text{QCD}} = -\frac{1}{4} G_{\mu\nu,a} G_a^{\mu\nu}. \quad (3.3)$$

Where n_f is the number of flavours, m_f are the quark masses, q_f are Dirac-spinors, D^μ is the covariant derivative and $G_a^{\mu\nu}$ is the field strength tensor of QCD. $\mu = 1 \dots 4$ is the Lorentz-index, $a = 1 \dots 8$ is the gluon-colour index and γ_μ are the Dirac matrices. D^μ and $G_a^{\mu\nu}$ are given by

$$D^\mu = \partial^\mu + ig_s A_a^\mu G_a, \quad (3.4)$$

$$G_a^{\mu\nu} = \partial^\mu A_a^\nu - \partial^\nu A_a^\mu - g_s f_{abc} A_b^\mu A_c^\nu. \quad (3.5)$$

With g_s being the colour gauge coupling constant of QCD, A_a^μ the eight gauge fields of QCD, G_a the generators of SU(3) and f_{abc} is the totally asymmetric tensor of the structure constants of the SU(3) algebra. G_a can be written in terms of the Gell-Mann-matrices λ_a

$$G_a = \frac{\lambda_a}{2}. \quad (3.6)$$

For the generators the following commutation relation holds

$$[G_a, G_b] = if_{abc}G_c. \quad (3.7)$$

3.1 QCD at low energy

As long as there is no nonperturbative (analytical) solution, another small expansion parameter must be found. Chiral perturbation theory does exactly this by exploiting the symmetry properties in the chiral limit ($m_f \rightarrow 0$).

Limiting the discussion to the three lightest quarks (up (u), down (d) and strange (s)) and considering that the mass of the proton $m_p = 938$ MeV, then $m_p \gg 2m_u + m_d$ holds, with $m_u = 5$ MeV and $m_d = 9$ MeV. This implies, that for the generation of hadron masses a complex mechanism must be responsible.

Let us now consider $m_u, m_d, m_s \rightarrow 0$ (chiral limit). Then, by inserting (3.2) and (3.3) into (3.1), equation (3.1) reduces to

$$\mathcal{L}_0^{\text{QCD}} = \sum_{f=1}^{n_f} i\bar{q}_f \not{D} q_f - \frac{1}{4} G_{\mu\nu, a} G_a^{\mu\nu} \quad \text{with} \quad \gamma_\mu D^\mu = \not{D}. \quad (3.8)$$

The covariant derivative \not{D} acts on colour and Dirac indices but not on flavour indices. $\mathcal{L}_0^{\text{QCD}}$ has an extra symmetry related to right- or left-handedness (chirality) of zero mass and spin 1/2 particles. To see this q is written as

$$q = \left[\frac{1}{2}(1 + \gamma_5) + \frac{1}{2}(1 - \gamma_5) \right] q = [P_R + P_L] q \equiv q_R + q_L, \quad (3.9)$$

with the indices R and L meaning right and left, respectively and $\gamma_5 = i\gamma_0\gamma_1\gamma_2\gamma_3$. The 4×4 matrices P_R and P_L have the properties

$$P_R + P_L = 1, \quad P_{R,L}^2 = P_{R,L}, \quad P_R P_L = P_L P_R = 0 \quad (3.10)$$

and project on the right- and left-handed quark states. Now the QCD-Lagrangian in the chiral limit can be written as

$$\mathcal{L}_0^{\text{QCD}} = \sum_{f=u,d,s} (\bar{q}_{R,f} i \not{D} \bar{q}_{R,f} + \bar{q}_{L,f} i \not{D} \bar{q}_{L,f}) - \frac{1}{4} G_{\mu\nu, a} G_a^{\mu\nu}. \quad (3.11)$$

The Lagrangian in (3.11) exhibits a $U(3)_L \otimes U_R(3)$ symmetry, i. e., it is invariant under transformations

$$q_R \rightarrow e^{-i\sum_{a=1}^8 \Theta_a^R \frac{\lambda_a}{2}} q_R, \quad q_L \rightarrow e^{-i\sum_{a=1}^8 \Theta_a^L \frac{\lambda_a}{2}} q_L. \quad (3.12)$$

Applying Noether's theorem to the Lagrangian in (3.11) one obtains the following conserved quantities (Noether currents)

$$V_a^\mu = \bar{q} \gamma^\mu \frac{\lambda_a}{2} q, \quad (3.13)$$

$$A_a^\mu = \bar{q} \gamma^\mu \gamma_5 \frac{\lambda_a}{2} q. \quad (3.14)$$

With V_a^μ being the vector current and A_a^μ the axial vector current. The properties of the vector and axial vector current under parity transformations P are

$$PV_a^\mu(t, \vec{x}) \rightarrow V_a^\mu(t, -\vec{x}), \quad (3.15)$$

$$PA_a^\mu(t, \vec{x}) \rightarrow -A_a^\mu(t, -\vec{x}). \quad (3.16)$$

In the massless case these currents are conserved and fulfil

$$\partial_\mu V_a^\mu = 0 \quad \text{and} \quad \partial_\mu A_a^\mu = 0 \quad (3.17)$$

and the corresponding Noether charges are conserved.

Considering non vanishing quark masses in the mass-term in (3.2)

$$\mathcal{L}_{\text{mass}} = \sum_{f=1}^{n_f} \bar{q}_f m_f q_f \quad (3.18)$$

and taking into account only the three light flavours, with $n_f = 3$ and

$$q = \begin{pmatrix} u \\ d \\ s \end{pmatrix}, \quad m_f = \begin{pmatrix} m_u & 0 & 0 \\ 0 & m_d & 0 \\ 0 & 0 & m_s \end{pmatrix}, \quad (3.19)$$

then the masses can be treated as a perturbation and the vector and the axial currents are no longer conserved

$$\partial_\mu V_a^\mu = i\bar{q} [m_f, \frac{\lambda_a}{2}] q, \quad (3.20)$$

$$\partial_\mu A_a^\mu = i\bar{q} \{ \frac{\lambda_a}{2}, m_f \} \gamma_5 q, \quad (3.21)$$

with the commutation relation $[A, B] := AB - BA$ and the anti-commutation relation $\{A, B\} := AB + BA$. Finally, the following statements can be made:

- For equal quark masses , $m_u = m_d = m_s \neq 0$ (isospin symmetry), the eight vector currents V_a^μ are conserved, since $[\lambda_a, 1] = 0$, see (3.20). In contrast, the axial vector currents A_a^μ are not conserved quantities. In the case of three quark flavours, this limit is usually referred to as the SU(3) limit.
- For $m_u = m_d = m_s = 0$, both – vector and axial-vector – currents are conserved and the Lagrangian in (3.11) exhibits the global chiral symmetry $SU(3)_L \otimes SU(3)_R$. This is called the chiral limit.

Partially conserved axial current – PCAC After the general discussion of symmetry properties of QCD for vanishing quark masses (chiral limit), the special role of pions should be pointed out. At a hadronic scale, compared to the nucleon mass, the pion mass is very small:

$$\left(\frac{m_\pi}{m_N}\right)^2 \approx \left(\frac{140 \text{ MeV}}{940 \text{ MeV}}\right)^2 \approx 0.02 \ll 1. \quad (3.22)$$

Considering the decay of a pion into a muon and a neutrino

$$\pi \rightarrow \mu + \nu, \quad (3.23)$$

the matrix element of this decay has a leptonic and a hadronic part. Due to parity considerations (the pion is a pseudoscalar particle), the decay is a pure axial vector transition and is described by the matrix element

$$\langle 0 | A_a^\mu(x) | \pi_b(q) \rangle = -i F_\pi q^\mu e^{-iqx} \delta_{ab}, \quad (3.24)$$

where a, b are isospin indices and q^μ is the four momentum of the pion. F_π is referred to as the pion decay constant. By forming the divergence of the axial current $\partial_\mu A^\mu$ in (3.24),

$$\langle 0 | \partial_\mu A_a^\mu(x) | \pi_b(q) \rangle = -i F_\pi q^2 e^{-iqx} \delta_{ab} = -i F_\pi m_\pi^2 e^{-iqx} \delta_{ab}, \quad (3.25)$$

is obtained, where $q^2 = q_\mu q^\mu = m_\pi^2$ was used. If the axial vector current was exactly conserved, this would imply

$$F_\pi m_\pi^2 = 0, \quad (3.26)$$

which is not observed in reality, since the pion has finite mass and $F_\pi \neq 0$ (the pion decays). However, the pion mass is small on the hadronic scale ($m_\pi \rightarrow 0$, see (3.22)) and hence, the hypothesis of partial conservation of the axial vector current (PCAC) is justified.

A microscopic basis of PCAC can be obtained by considering the components $A_{1,2,3}^\mu$ in

(3.21) operating in the sector of u and d quarks. Using the combinations $A_{\pm}^{\mu} = A_1^{\mu} \pm iA_2^{\mu}$ one finds

$$\partial_{\mu}A_{+}^{\mu} = (m_u + m_d) \bar{q}_u i\gamma_5 q_d, \quad (3.27)$$

$$\partial_{\mu}A_{-}^{\mu} = (m_u + m_d) \bar{q}_d i\gamma_5 q_u, \quad (3.28)$$

$$\partial_{\mu}A_3^{\mu} = m_u \bar{q}_u i\gamma_5 q_u + m_d \bar{q}_d i\gamma_5 q_d. \quad (3.29)$$

The divergence of the axial current thus produces sources of the pseudoscalar quark-antiquark pairs. In the chiral limit, the axial current is conserved again by setting $m_u, m_d \rightarrow 0$ in (3.27), (3.28) and (3.29).

Goldberger-Treiman relation A relation of quantities from weak interaction to quantities from strong interaction is given by the Goldberger-Treiman (GT) relation [32, 33]. For its derivation the assumption of vanishing pion mass (PCAC) is used and it reads:

$$\left(\frac{g_{\pi NN}}{m_N}\right)^2 = \left(\frac{g_A}{F_{\pi}}\right)^2 = 0.072, \quad (3.30)$$

where

$$g_{\pi NN} = \frac{2m_N}{m_{\pi}} \sqrt{4\pi} f_{\pi N}. \quad (3.31)$$

Here $f_{\pi N}$ is the pion nucleon coupling constant (see section 3.4), m_N and m_{π} are the masses of the proton and the charged pion, respectively, and g_A is the axial coupling constant, which stems from the axial form factor of the nucleon.

The GT relation is satisfied at the percent level (2-4%). Its violation is expressed in the so-called Goldberger-Treiman discrepancy

$$\Delta_{\pi N} = 1 - \frac{m_N g_A}{F_{\pi} g_{\pi NN}}, \quad (3.32)$$

which constitutes a measure of chiral symmetry breaking.

Chiral perturbation theory – ChPT ChPT is formulated in the chiral limit, i. e., it is based on massless QCD, with quark masses introduced only as perturbation. It is an effective field theory (EFT). The basic idea of effective field theories is, that it is not necessary to know everything in order to make useful statements on a particular part of physics. Generally speaking, effective field theories are low energy approximations of more fundamental theories. EFTs can be used to calculate physical quantities up to an energy scale which is defined by p/Λ , where p can stand for momenta or masses that are smaller than the scale of Λ .

The foundation of ChPT was laid by Weinberg [34] and in [30, 31] Gasser and Leutwyler

performed first calculations within the framework of ChPT. Principally, ChPT is an expansion of the effective Lagrangian in powers of (small) momenta and the chiral symmetry breaking terms (light quark masses and the fine structure constant α), in which the consecutive terms in the chiral expansion are suppressed by the inverse powers of the symmetry breaking scale ($\Lambda \sim 1 \text{ GeV}$):

$$\mathcal{L}_{\text{eff}} = \sum_n \mathcal{L}_n = \mathcal{L}_0 + \mathcal{L}_2 + \mathcal{L}_4 + \mathcal{L}_6 + \dots \quad (3.33)$$

Here n denotes the low energy dimension, also known as chiral dimension (number of derivatives and/or quark masses); the term of order 0 is a constant. The restriction to even terms in the development is due to Lorentz invariance.

By this chiral expansion, low energy constants (LECs) are introduced, which can not be determined by symmetry considerations alone. In the ideal case, the LECs should be calculated from the fundamental underlying theory. Alternatively, LECs can be determined with the help of experiments.

A detailed discussion of the formulation of ChPT is beyond the scope of this work and the interested reader is referred to various reviews, such as for instance [35] and references therein. Detailed discussion on PCAC and topics connected to chiral symmetry can be found in, e. g., [32, 36].

In the following section the connection between experimentally accessible (strong interaction shift ϵ_{1s} and width Γ_{1s} in π^-p) and in the framework of ChPT important quantities (low energy scattering lengths and LECs) will be established.

3.2 πN scattering lengths

A very important concept in strong interaction is isospin symmetry, where the proton and the nucleon are regarded as two states of the same particle, the nucleon. Proton and neutron are defined as two components of an isospin $\frac{1}{2}$ doublet:

$$|p\rangle = \begin{pmatrix} 1 \\ 0 \end{pmatrix}, \quad |n\rangle = \begin{pmatrix} 0 \\ 1 \end{pmatrix}. \quad (3.34)$$

Similarly, a pion can be represented as a three vector in isospin space, such that the three charge states of a pion are summarised in a vector $\vec{\Phi} = (\Phi_1, \Phi_2, \Phi_3) = (\pi^+, \pi^0, \pi^-)$. This three states form an isospin triplet and the three charge states can be written as

$$\pi^- = \frac{1}{\sqrt{2}} \begin{pmatrix} 1 \\ -i \\ 0 \end{pmatrix}, \quad \pi^0 = \begin{pmatrix} 0 \\ 0 \\ 1 \end{pmatrix}, \quad \pi^+ = -\frac{1}{\sqrt{2}} \begin{pmatrix} 1 \\ i \\ 0 \end{pmatrix}. \quad (3.35)$$

Pions form an isospin triplet with isospin $I^\pi = 1$ and with π^- , π^0 , π^+ being the eigenstates of the third component of the isospin I_3^π , where $I_3^\pi = -1, 0, +1$, respectively. Accordingly, the neutron and the proton form an isospin doublet with $I^N = \frac{1}{2}$ and $I_3^N = -\frac{1}{2}, +\frac{1}{2}$, respectively.

In terms of $|I, I_3\rangle$ one can write the nucleon states as

$$|p\rangle = \left| \frac{1}{2}, \frac{1}{2} \right\rangle, \quad |n\rangle = \left| \frac{1}{2}, -\frac{1}{2} \right\rangle \quad (3.36)$$

and the pion states as

$$|\pi^+\rangle = |1, 1\rangle, \quad |\pi^0\rangle = |1, 0\rangle, \quad |\pi^-\rangle = |1, -1\rangle, \quad (3.37)$$

where I is the isospin quantum number and I_3 its projection onto the third component, see [37].

Considering pion-nucleon scattering, the initial state consists of a pion with isospin 1 and a nucleon with isospin $\frac{1}{2}$. Therefore the initial state can be expressed as a superposition of the total isospin $\frac{1}{2}$ and 1, depending on the orientation of the isospin of the nucleon and the pion. The states are

$$I = \frac{1}{2} \quad \begin{cases} I_3 = +\frac{1}{2} : & \sqrt{\frac{1}{3}}|p\pi^0\rangle - \sqrt{\frac{2}{3}}|n\pi^+\rangle \\ I_3 = -\frac{1}{2} : & \sqrt{\frac{2}{3}}|p\pi^-\rangle - \sqrt{\frac{1}{3}}|n\pi^0\rangle, \end{cases} \quad (3.38)$$

$$I = \frac{3}{2} \quad \begin{cases} I_3 = +\frac{3}{2} : & |p\pi^+\rangle \\ I_3 = +\frac{1}{2} : & \sqrt{\frac{2}{3}}|p\pi^0\rangle + \sqrt{\frac{1}{3}}|n\pi^+\rangle \\ I_3 = -\frac{1}{2} : & \sqrt{\frac{1}{3}}|p\pi^-\rangle + \sqrt{\frac{2}{3}}|n\pi^0\rangle \\ I_3 = -\frac{3}{2} : & |n\pi^-\rangle. \end{cases} \quad (3.39)$$

Let us now consider the three experimentally accessible elastic scattering processes involving pions and nucleons

$$\pi^+ + p \rightarrow \pi^+ + p, \quad (3.40)$$

$$\pi^- + p \rightarrow \pi^- + p, \quad (3.41)$$

$$\pi^- + p \rightarrow \pi^0 + n. \quad (3.42)$$

Where (3.42) describes the charge exchange reaction.

With the total isospin $\vec{I} = \vec{I}^\pi + \vec{I}^N$ of the pion-nucleon system and its third component $I_3 = I_3^\pi + I_3^N$, the properties of this system can be written in terms of a state vector $|I, I_3\rangle$ containing only the total isospin and its third component. The possible values of

the total isospin I are $\frac{1}{2}$ and $\frac{3}{2}$. With the appropriate Clebsch-Gordan coefficients, the state vectors of the physical channels can be written in terms of $|I, I_3\rangle$ as

$$|\pi^+p\rangle = \sum_I C_{1,1/2} \left(I, \frac{3}{2}; 1, \frac{1}{2} \right) |I, I_3\rangle = \left| \frac{3}{2}, \frac{3}{2} \right\rangle \quad (3.43)$$

$$|\pi^-p\rangle = \sum_I C_{1,1/2} \left(I, -\frac{1}{2}; -1, \frac{1}{2} \right) |I, I_3\rangle = \sqrt{\frac{1}{3}} \left| \frac{3}{2}, -\frac{1}{2} \right\rangle - \sqrt{\frac{2}{3}} \left| \frac{1}{2}, -\frac{1}{2} \right\rangle \quad (3.44)$$

$$|\pi^0n\rangle = \sum_I C_{1,1/2} \left(I, -\frac{1}{2}; 0, -\frac{1}{2} \right) |I, I_3\rangle = \sqrt{\frac{2}{3}} \left| \frac{3}{2}, -\frac{1}{2} \right\rangle + \sqrt{\frac{1}{3}} \left| \frac{1}{2}, -\frac{1}{2} \right\rangle \quad (3.45)$$

with the Clebsch-Gordan coefficient $C_{I\pi, I^N} (I, I_3; I_3^\pi, I_3^N)$ (the sign convention is that of Wigner used in [38]).

If charge independence is assumed, i. e., that the matrix elements of the transition matrix depend only on I , but not on I_3 , and the masses of the quarks are considered to be equal, then the scattering matrix – the \mathbf{T} -matrix – can be decomposed as

$$\langle I' I_3 | \mathbf{T} | I I_3 \rangle = T_I \delta_{I, I'} \delta_{I_3, I'} \quad (3.46)$$

and hence, using (3.43), (3.44) and (3.45) it can be written

$$\langle \pi^+p | \mathbf{T} | \pi^+p \rangle = T_{\frac{3}{2}}, \quad (3.47)$$

$$\langle \pi^-p | \mathbf{T} | \pi^-p \rangle = \frac{1}{3} T_{\frac{3}{2}} + \frac{2}{3} T_{\frac{1}{2}}, \quad (3.48)$$

$$\langle \pi^-p | \mathbf{T} | \pi^0n \rangle = \frac{\sqrt{2}}{3} \left(T_{\frac{3}{2}} - T_{\frac{1}{2}} \right). \quad (3.49)$$

This calculation is only valid, if Coulomb scattering of the charged particles and the mass differences between the three charged states of the pion is neglected.

From scattering theory it is known that the elements of the \mathbf{T} -matrix are related to the scattering amplitude $f(E, \theta)$ (the isospin index I is suppressed for convenience)

$$T \propto -f(E, \theta). \quad (3.50)$$

$f(E, \theta)$ can be written in terms of a partial-wave expansion

$$f(E, \theta) = \sum_{l=0}^{\infty} (2l+1) f_l(E) P_l(\cos \theta), \quad (3.51)$$

where $P_l(\cos \theta)$ are the Legendre-polynomials and

$$f_l(E) = \frac{e^{2i\delta_l(E)} - 1}{2ip} = \frac{e^{i\delta_l(E)} \sin \delta_l}{p} \quad (3.52)$$

denotes the partial-wave amplitude, where δ_l is the scattering phase and p is the momentum. For low energy with $p \rightarrow 0$ the amplitude becomes

$$\lim_{p \rightarrow 0} f_l = \lim_{p \rightarrow 0} \frac{e^{i\delta_l(E)} \sin \delta_l}{p} \rightarrow -a_l p^{2l}, \quad (3.53)$$

where a_l is known as the scattering lengths for $l = 0$ and scattering volume for $l \geq 1$. For s-wave scattering with $l = 0$ one finds, that $f_{l=0} \rightarrow -a_0$.

Finally, using (3.53) with $l = 0$ equations (3.47), (3.48) and (3.49) can be rewritten as

$$\begin{aligned} \lim_{p \rightarrow 0} \langle \pi^+ p | \mathbf{T} | \pi^+ p \rangle &= a_{\frac{3}{2}} \\ \lim_{p \rightarrow 0} \langle \pi^- p | \mathbf{T} | \pi^- p \rangle &= \frac{1}{3} a_{\frac{3}{2}} + \frac{2}{3} a_{\frac{1}{2}} \\ \lim_{p \rightarrow 0} \langle \pi^- p | \mathbf{T} | \pi^0 n \rangle &= \frac{\sqrt{2}}{3} (a_{\frac{3}{2}} - a_{\frac{1}{2}}), \end{aligned} \quad (3.54)$$

or

$$\begin{aligned} a_{\pi^+ p \rightarrow \pi^+ p} &= a_{3/2} \\ a_{\pi^- p \rightarrow \pi^- p} &= \frac{1}{3} (2a_{1/2} + a_{3/2}) \\ a_{\pi^- p \rightarrow \pi^0 n} &= \frac{\sqrt{2}}{3} (a_{3/2} - a_{1/2}). \end{aligned} \quad (3.55)$$

A detailed discussion of non-relativistic scattering theory may be found in [39, 40] and thorough discussion of the pion-nucleon system is given in [32, 41].

The hadronic scattering lengths in (3.55) are connected to each other by the so-called isospin triangle

$$a_{\pi^- p \rightarrow \pi^- p} - a_{\pi^+ p \rightarrow \pi^+ p} = \sqrt{2} a_{\pi^- p \rightarrow \pi^0 n}. \quad (3.56)$$

Introducing the isoscalar (isospin-even) and isovector (isospin-odd) scattering lengths a^+ and a^-

$$a^\pm = \frac{1}{2} (a_{\pi^- p \rightarrow \pi^- p} \pm a_{\pi^+ p \rightarrow \pi^+ p}), \quad (3.57)$$

and isospin conservation given, one can write

$$a_{\pi^- p \rightarrow \pi^- p} = a^+ + a^- \quad \text{and} \quad a_{\pi^- p \rightarrow \pi^0 n} = -\sqrt{2} a^-, \quad (3.58)$$

or

$$a^+ = \frac{a_{1/2} + 2a_{3/2}}{3}, \quad (3.59)$$

$$a^- = \frac{a_{1/2} - a_{3/2}}{3}. \quad (3.60)$$

The scattering lengths a^+ and a^- were already calculated by Weinberg in the framework of current algebra using PCAC [42] and yielded $a^+ = 0$ and $a^- = 0.08m_\pi^{-1}$, representing the leading order of ChPT. Therefore, deviations from these values are a measure of chiral symmetry breaking.

3.3 Relation of scattering lengths to ϵ_{1s} and Γ_{1s}

The measurable quantities ϵ_{1s} and Γ_{1s} are related to the low energy scattering lengths a^+ and a^- using Deser-type formulae [1, 43]

$$\frac{\epsilon_{1s}}{E_{1s}} = -4\frac{1}{r_B}a_{\pi^-p \rightarrow \pi^-p}(1 + \delta_\epsilon) \quad (3.61)$$

$$\frac{\Gamma_{1s}}{E_{1s}} = 8\frac{Q_0}{r_B}\left(1 + \frac{1}{P}\right)(a_{\pi^-p \rightarrow \pi^0n}(1 + \delta_\Gamma))^2. \quad (3.62)$$

Here $E_{1s} = 3238$ eV is the el. mag. binding energy of the ground-state, $r_B = 222.56$ fm is the Bohr radius in π^-p , $Q_0 = 0.142$ fm $^{-1}$ is the cms momentum of the π^0 , $P = 1.546 \pm 0.009$ is the Panofsky ratio between $\pi^-p \rightarrow \pi^0n$ and $\pi^-p \rightarrow \gamma n$ [44], $\delta_{\epsilon,\Gamma}$ are corrections. Their relevance will be discussed separately.

Using (3.58) this leads to

$$\epsilon_{1s} \propto a^+ + a^- \quad \text{and} \quad \Gamma_{1s} \propto (a^-)^2. \quad (3.63)$$

3.3.1 Corrections $\delta_{\epsilon,\Gamma}$

The level of accuracy for the measured values of the strong interaction width and shift in the experiment discussed in this work is desired to be at the percent level. From these accurate values, the s-wave pion-nucleon scattering lengths in "pure" QCD will be extracted. In order to achieve this goal, the corrections $\delta_{\epsilon,\Gamma}$ stated in (3.61) and (3.62) have to be known accurately as well.

For the calculation of $\delta_{\epsilon,\Gamma}$ various approaches are available [45–51]. The predecessor π^-p experiment of the ETHZ-PSI collaboration [6] used corrections based on a potential model [45], where $\delta_\epsilon = (2.1 \pm 0.5) \cdot 10^{-2}$ and $\delta_\Gamma = (1.3 \pm 0.5) \cdot 10^{-2}$. However, it turned out that the potential model is incomplete. In [50,51] $\delta_{\epsilon,\Gamma}$ are calculated within a quantum field theoretic, relativistic covariant and model-independent approach. Below a brief survey of the calculations within the models described in [46–49] is given.

Correction for the shift – δ_ϵ In [46] a new calculation of δ_ϵ was performed in the framework of effective field theories at next-to-leading order in the low energy expansion.

Whereas, in [47] the correction was calculated in leading order. The relation between the strong energy-level shift ϵ_{1s} of the ground state in pionic hydrogen and the threshold scattering amplitude for the process $\pi^- p \rightarrow \pi^- p$, $\mathcal{T}_{\pi N}$, was calculated in [47] and reads

$$\epsilon_{1s} = -\frac{\alpha^3 \mu_c^3 \mathcal{T}_{\pi N}}{2\pi m_\pi} \left\{ 1 - \frac{\alpha (\ln \alpha - 1) \mu_c^2 \mathcal{T}_{\pi N}}{2\pi m_\pi} \right\} + \dots \quad (3.64)$$

With $\mu_c = \frac{m_p m_\pi}{m_p + m_\pi}$ being the reduced mass of the pion-nucleon system, m_p and m_π standing for the mass of the proton and the mass of the charged pion, respectively and α is the fine structure constant.

The scattering amplitude $\mathcal{T}_{\pi N}$ can be written as $\mathcal{T}_{\pi N} = \mathcal{T}_{\pi N}^0 + \delta\mathcal{T}$. Here $\mathcal{T}_{\pi N}^0$ is the isospin symmetric part, referring to "pure" QCD and $\delta\mathcal{T}$ accounts for isospin-breaking effects. Now the correction δ_ϵ takes the form [46]

$$\delta_\epsilon = \frac{\delta\mathcal{T}}{4\pi (1 + m_\pi/m_p) (a^+ + a^-)} - 2\alpha (\ln \alpha - 1) \mu_c (a^+ + a^-) + \delta_\epsilon^{\text{vac}}, \quad (3.65)$$

where $\delta_\epsilon^{\text{vac}}$ is the correction due to the interference of vacuum polarisation and strong interactions. The calculation of $\delta_\epsilon^{\text{vac}}$ within a non-relativistic effective Lagrangian approach gave $\delta_\epsilon^{\text{vac}} = 0.48\%$ [52].

The leading term of the chiral expansion $\delta\mathcal{T} = \delta\mathcal{T}_2 + \delta\mathcal{T}_3 + \mathcal{O}(p^4)$ was calculated in [47] and gave

$$\delta\mathcal{T}_2 = \frac{m_p}{8\pi (m_p + m_{\pi^+}) F_\pi^2} \left\{ 8c_1 (m_{\pi^+}^2 - m_{\pi^0}^2 - 4e^2 f_1 - e^2 f_2) \right\}, \quad (3.66)$$

with the pion decay constant F_π^2 , the electron charge e and the low-energy constants (LECs) c_1 , f_1 and f_2 . The term $\delta\mathcal{T}_3$ was evaluated in [46] and thus the final result for δ_ϵ in this context reads

$$\delta_\epsilon = (-7.2 \pm 2.9) \cdot 10^{-2}. \quad (3.67)$$

Since the LECs are constants in the theory, they have to be determined experimentally. Up to now only c_1 and f_2 are known with some accuracy. c_1 was determined from πN phase shift data [53] and f_2 is related to the electromagnetic part of the proton-neutron mass difference by $-e^2 F_\pi^2 f_2 = (m_p - m_n)^{\text{em}}$. F_π is the pion decay constant in the chiral limit.

The determination of f_1 , however, is problematic and can presently be approximated only. See [46] for a detailed discussion of this issue. The error $\pm 2.9 \cdot 10^{-2}$ of the correction from (3.67) is dominated by the poorly known value for the LEC f_1 , which has an uncertainty of $\pm 2.8 \cdot 10^{-2}$. Taking into account $\delta\mathcal{T}_3$ doesn't help, since only more LEC are introduced, though they are suppressed by one power of the pion mass m_π and their effect on the shift is thus expected to be small, compared to the ones from the leading order.

Correction for the width – δ_Γ A recent calculation of the isospin correction δ_Γ in leading-order in ChPT was performed in [48]. In leading order it does not depend on the unknown LEC f_1 , which decreases the uncertainty of the calculation significantly. In fact, in leading order it only depends on the LECs f_2 and c_1 . The result presented in [48, 49] yields

$$\delta_\Gamma = (0.6 \pm 0.2) \cdot 10^{-2}. \quad (3.68)$$

3.4 πN coupling constant

Another important motivation to improve the accuracy of Γ_{1s} and thereby improving a^- , is the pion-nucleon coupling constant $f_{\pi^- N}^2$. Via the Goldberger-Miyazawa-Oehme (GMO) sum rule [54], the isovector scattering lengths a^- is related to $f_{\pi^- N}^2$ as

$$f_{\pi^- N}^2 = \frac{1}{2} \left[1 - \left(\frac{m_\pi}{2m_N} \right)^2 \right] \left[\left(1 + \frac{m_\pi}{m_N} \right) m_\pi a^- - m_\pi^2 \cdot J \right], \quad (3.69)$$

where J is the difference between the total cross sections σ of $\pi^+ p$ and $\pi^- p$ scattering, integrated over the momentum q :

$$J = \frac{1}{4\pi^2} \int_0^\infty \frac{\sigma_{\pi^- p} - \sigma_{\pi^+ p}}{\sqrt{q^2 + m_\pi^2}} dq. \quad (3.70)$$

A recent evaluation of J gave [55]

$$J = -1.083 \pm 0.009 \pm 0.031 \text{ mb}. \quad (3.71)$$

An improved value of the pion nucleon coupling constant allows a more accurate determination of the Goldberger-Treiman discrepancy (3.32).

3.5 πN sigma term

A measure of the contribution of the non-vanishing quark masses to the nucleon mass and the strangeness content of the nucleon is provided by the so-called pion-nucleon sigma term

σ_N

$$\sigma_N = \frac{1}{2M_N} (m_u + m_d) \langle N | \bar{u}u + \bar{d}d | N \rangle, \quad (3.72)$$

where M_N is the nucleon mass, m_u and m_d are the masses of the up and down quark, respectively and N denotes the nucleon state. The connection of the πN sigma term to pion-nucleon scattering is provided by the isoscalar scattering length a^+ at the unphysical

Cheng-Dashen point ($\nu = (s - u) = 0, t = 2m_\pi^2$).

σ_N can not be obtained from pion-nucleon scattering lengths only, but also scattering volumes are needed. Therefore it can not be determined fully from s-wave scattering alone. For detailed discussion of the pion nucleon sigma term the reader is referred to [56–58].

3.6 Pionic deuterium

Additional constraints for the isoscalar a^+ and the isovector a^- scattering lengths and the LEC f_1 can be provided by a measurement of the strong interaction shift and width in pionic deuterium. Schematically, ϵ_{1s} and Γ_{1s} in π^-p and π^-d are functions of a^+ , a^- and f_1 (higher order terms are neglected):

$$\begin{aligned}\pi^-p &\Rightarrow \epsilon_{1s}^{\pi^-p}(a^+, a^-, f_1), \\ \pi^-p &\Rightarrow \Gamma_{1s}^{\pi^-p}(a^-), \\ \pi^-d &\Rightarrow \epsilon_{1s}^{\pi^-d}(a^+, a^-, f_1),\end{aligned}\tag{3.73}$$

which, coarsely spoken, leads to three equations with three variables.

Similarly to pionic hydrogen, the relation between the measurable quantity ϵ_{1s} and the real part of the scattering length in π^-d $\text{Re } a_{\pi d}$ is given by

$$\epsilon_{1s} = -2\alpha^3 \mu_d^2 \text{Re } a_{\pi d}.\tag{3.74}$$

In [59] an expression for $\text{Re } a_{\pi d}$ within ChPT was derived under the assumption of exact isospin symmetry. Until recently, using the values for ϵ_{1s} , Γ_{1s} , δ_ϵ , δ_Γ and the value for the scattering length for π^-d from [60] this led to a coherent picture. The values for a^+ and a^- which emerge from the three different measurements had a common intersection region. This case is schematically shown in Figure 3.1.

Preliminary analysis of the new pionic hydrogen experiment, together with new calculations of the corrections δ_ϵ and δ_Γ (see section 3.3.1), however, resulted in slightly shifted bands for a^+ and a^- which do no longer have a common intersection region.

A theoretical investigation up to next-to-leading order in [61] points out, that isospin symmetry corrections are significant in pionic deuterium and hence, the theoretical treatment of the πd scattering length must be adapted accordingly. Thus $\text{Re } a_{\pi d}$ is written as

$$\text{Re } a_{\pi d} = \text{Re } \bar{a}_{\pi d} + \Delta a_{\pi d},$$

where $\text{Re } \bar{a}_{\pi d}$ refers to the isospin limit and $\Delta a_{\pi d}$ takes into account isospin breaking terms. That way values for a^+ and a^- can be obtained, such, that the three bands have a

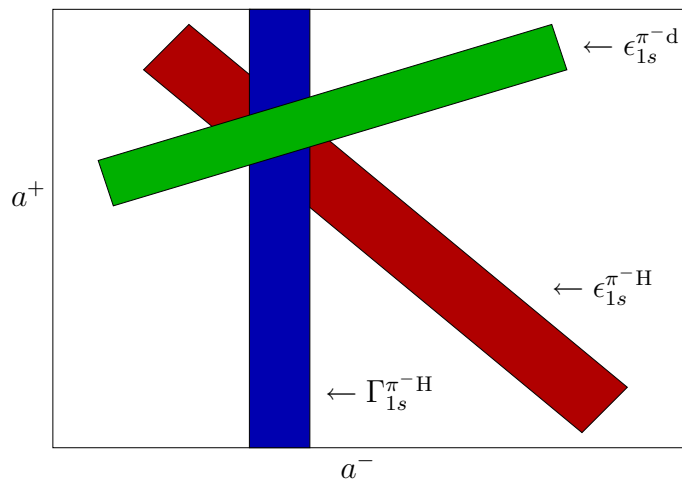


Figure 3.1: Schematic view of the bands for a^+ and a^- , resulting from measurements of $\epsilon_{1s}^{\pi^-H}$, $\Gamma_{1s}^{\pi^-H}$ and ϵ_{1s}^d . The scale on the axes is arbitrary.

common intersection area again. For a detailed theoretical discussion of this issue see [61] and [62].

From the above discussion it is clear, that this matter needs clarification. Therefore, pionic deuterium X-rays from the $3p \rightarrow 1s$ transition were measured in 2006 at PSI. The analysis is still in progress and will be published elsewhere.

4 Experimental setup and data processing

Accuracy at the level of a few per mill for the ground-state shift and a few percent for the width requires a highly sophisticated and well understood experimental setup and an efficient formation of pionic hydrogen.

In the next sections the main parts of the experimental setup will be described. The starting point is the pion production at the accelerator at PSI, and finally the X-ray signal as measured by the CCD detectors completes the description. Following the description of the setup, the processing of the data will be explained.

In the beginning a general sketch of the experimental approach is given, followed by a detailed description of the respective components of the apparatus.

4.1 The experimental approach

For the production of pionic hydrogen, the high intensity low energy pion beam at PSI was used. Therefore the experimental apparatus was set up in the $\pi E5$ area of the experimental hall at PSI (see Figure 4.1). The principle of the experiment is depicted in Figure 4.2.

After passing the beamline leading to the $\pi E5$ area, pions are stopped in a cryogenic target using a cyclotron trap. The target is filled with hydrogen gas. A small fraction of the pions is captured by the hydrogen atoms in the target gas and pionic hydrogen is formed. After undergoing cascade processes, as described in chapter 2, amongst others, pionic hydrogen X-rays originating from the $4p \rightarrow 1s$, $3p \rightarrow 1s$ and $2p \rightarrow 1s$ transitions, are emitted. The X-rays are diffracted by a spherically bent Bragg-crystal and are finally measured at a position sensitive large-area detector comprised of an array of six charge-coupled devices (CCDs).

4.1.1 Pion production

For pion production at PSI, a high intensity ring cyclotron is used. From this cyclotron a proton beam with an energy of 590 MeV is extracted. During the experimental periods

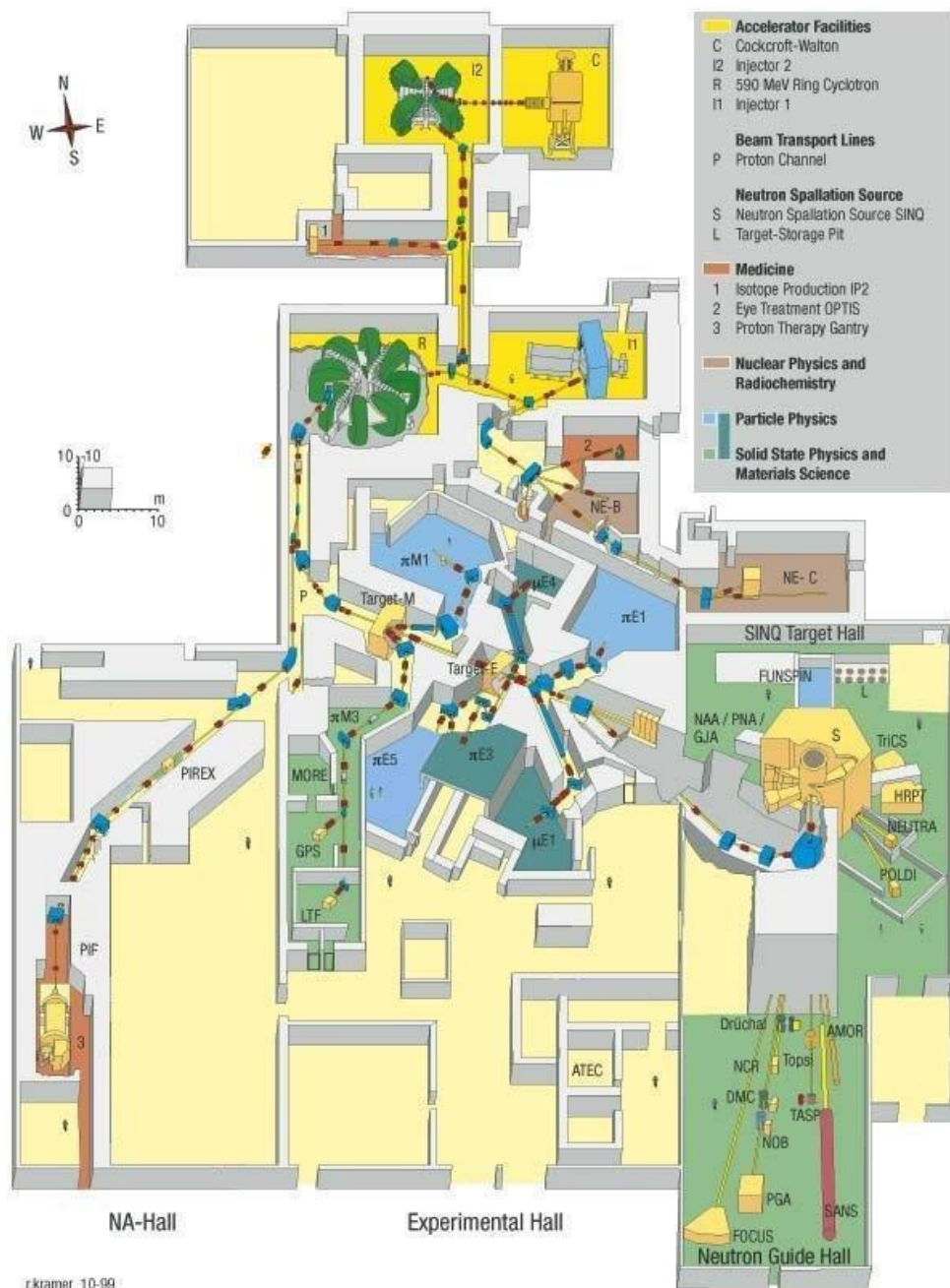


Figure 4.1: Overview of the accelerator complex and the experimental hall at PSI.

the current was up to 1.6 mA and thus it is ideally suited for a high rate production of pions. After extraction (efficiency = 99.7%), the protons are guided to the production target "E", made out of carbon with diameter of 40 mm. The secondary π E5 beam line conducts the produced pions into the experimental area.

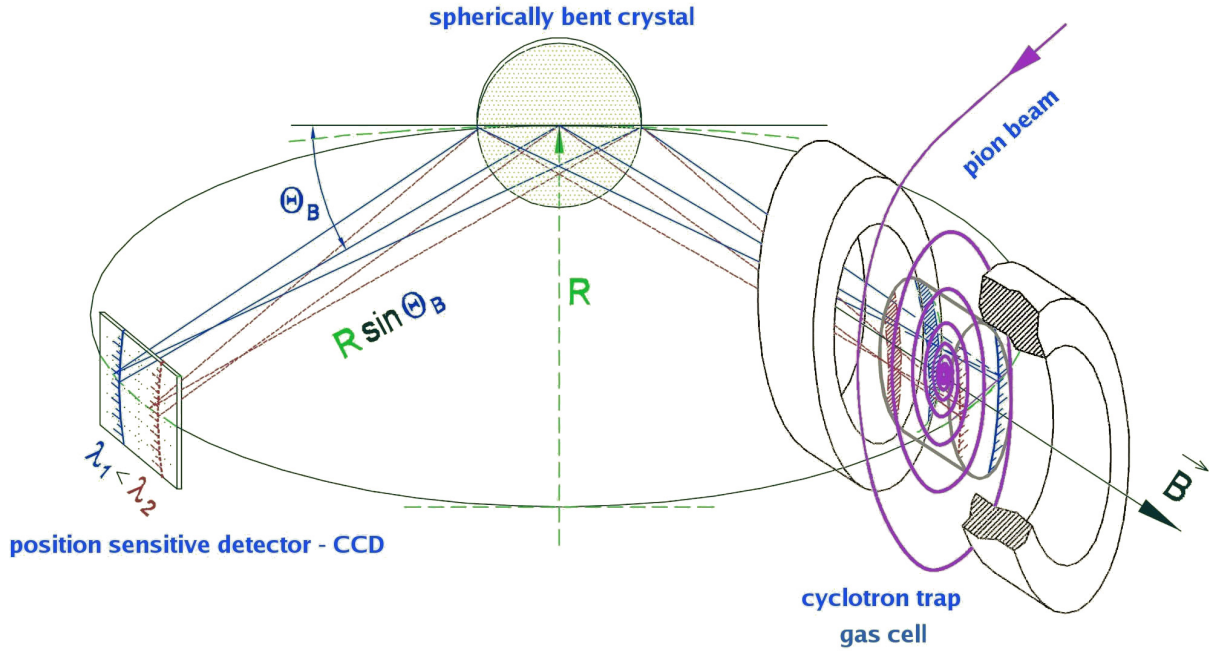


Figure 4.2: Basic setup principle of the pionic hydrogen experiment, for details see text.

Since pions decay within $\tau_{\pi^-} = 2.6 \cdot 10^{-8}$ s, the shortness of the $\pi E5$ beam line (10.4 m) is ideally suited for guiding low energy pions (and muons) with momenta in the range of 10 – 120 MeV/ c . The momentum acceptance of the $\pi E5$ beam line is 10% and its momentum resolution amounts to 2%. The dimension of the spot size in the focus is 15 mm horizontal and 20 mm vertical, with an angular divergence of 450 mrad horizontal and 120 mrad vertical. A graphic overview of the experimental hall and the accelerator is given in Figure 4.1.

For the $\pi^- p$ experiment a pion beam with momentum of 112 MeV/ c was used and injected into the cyclotron trap. At this setting, a pion rate of $4 \cdot 10^9 \pi^- / s$ is achieved. In Figure 4.3 the setup of the experiment in the area $\pi E5$ can be seen.

4.1.2 Cyclotron trap

In order to form a large number of pionic hydrogen atoms in the target gas, pions, coming from the beam line, have to be slowed down from the MeV range to a few eV. Pions exhibit a short lifetime, therefore the deceleration has to be accomplished very quickly. Additionally, to increase the number of formed pionic hydrogen atoms, a high stop density of pions in the target gas has to be achieved.

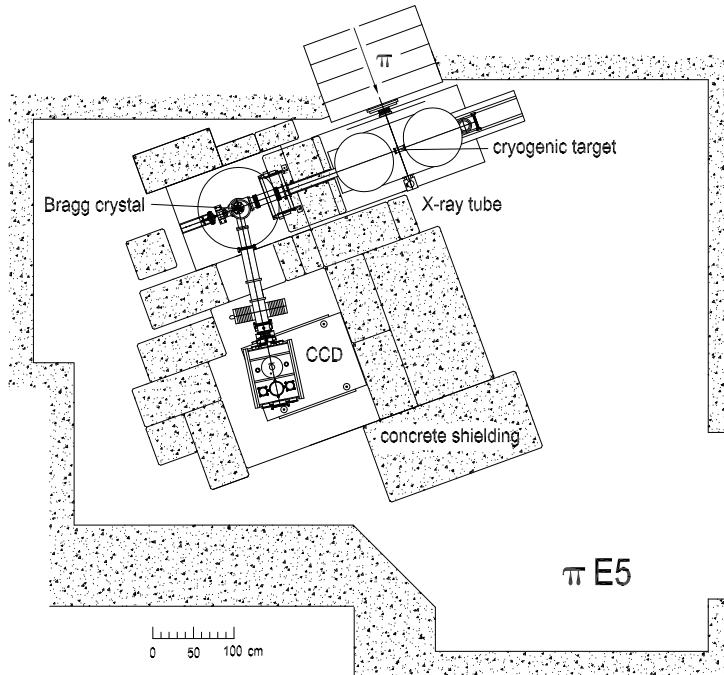


Figure 4.3: Setup of the experiment at PSI. A fraction of the incoming pions is stopped in the target cell inside the cyclotron trap. X-rays from pionic hydrogen are emitted to a crystal, where they are Bragg-reflected onto the CCD detector. The concrete shielding indicated in the figure is essential for an efficient background reduction.

The cyclotron trap described in [63] fulfils both purposes. It consists of a split coil superconducting magnet, with a weakly focusing axial \vec{B} -field (Figure 4.4). Once the pions arrive at the cyclotron trap, the strong magnetic field forces the pions onto spiral orbits. The magnetic field alone, however, would not be sufficient to guide the pions into the target in time. Therefore, plastic degraders mounted in the path of the pions are used. With the help of these degraders, the pion momenta are reduced and that way pions are guided into the target cell after approximately 2 turns.

To have conditions as ideal as possible, i. e., a high stop density of pions in the target, the thickness of the degraders was optimised. That way, approximately 1% of pions entering the cyclotron trap are stopped in the target at 1 bar (equivalent to room temperature) and increase approximately linearly with density.

Of course, at such high pion rates like they occur at PSI, a high neutron background (by absorption of pions in matter) is produced in the experimental area. Therefore, background and its suppression is an important issue of the new pionic hydrogen experiment, as will become more clear as soon as the analysis of the data will be discussed in detail in chapter 6.

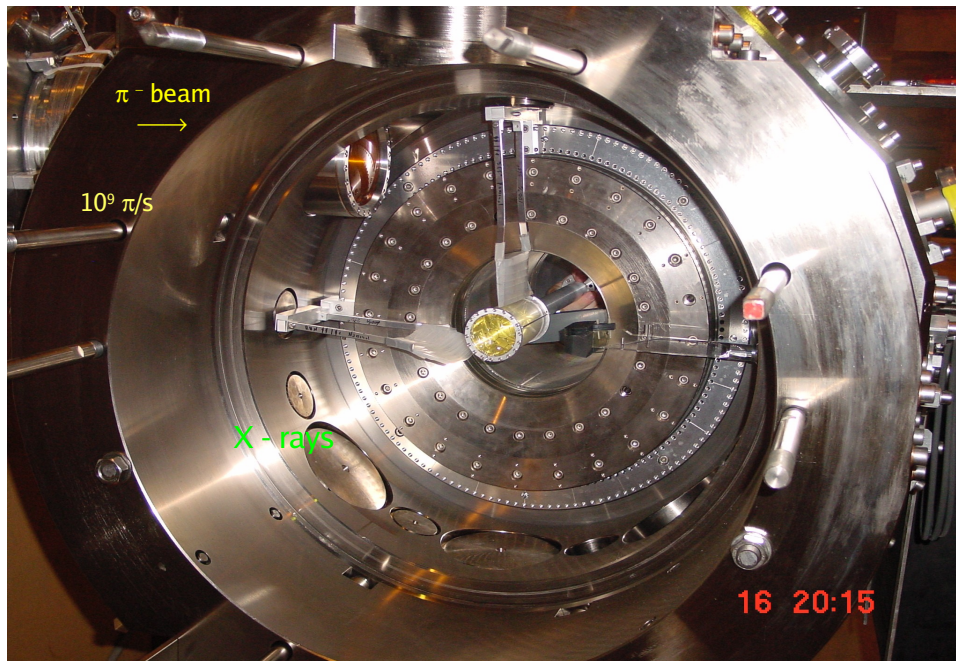


Figure 4.4: Cyclotron trap with target cell in the centre. A high flux of pions is entering on top left of the cyclotron trap. After entering the trap, the pions are forced onto spiral orbits using the trap’s magnetic field and degraders mounted in their path. After approximately two turns a fraction of the pions stops in the central target cell.

4.1.3 Cryogenic target

As outlined in chapter 2, the pressure dependence of the energy of the emitted X-rays has to be verified. This can not be achieved by simply increasing and decreasing the pressure in an arbitrary gas cell, as the low energy pionic hydrogen X-rays (~ 3 keV) considered here, would be absorbed in any thick enough material to withhold high pressures. Therefore a cryogenic target (Figure 4.5), which could be cooled down to 20 K, was used. With it a large pressure range (equivalent to room temperature) could be reached. It was placed in the axis of the magnetic field produced by the cyclotron trap (see also Figure 4.4). Cooling was achieved by an external copper cold finger onto which the target was mounted. Furthermore, the axial target position could be changed without breaking the vacuum (Figure 4.10).

The most important requirement for the window of the target cell was to absorb as few as possible of the produced pionic hydrogen X-rays. Therefore it was made out of a very thin Kapton foil ($7.5 \mu\text{m}$), stabilised by an aluminium support structure containing a

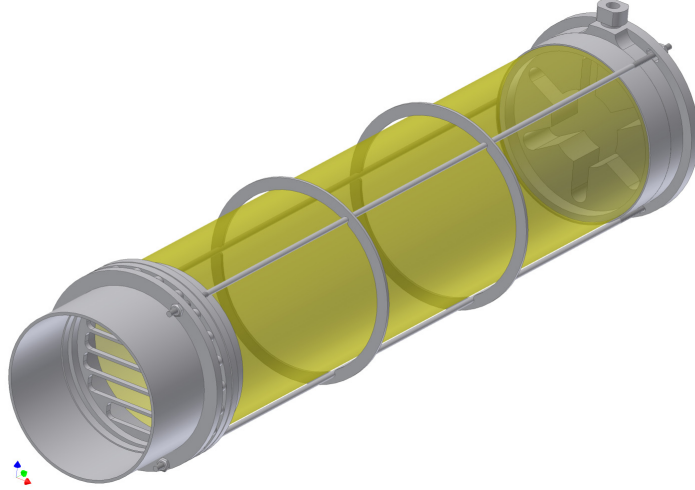


Figure 4.5: Three dimensional view of the cryogenic target cell used in the pionic hydrogen experiment.

horizontal grating. The walls of the cylinder were made out of $50\ \mu\text{m}$ Kapton, supported by two aluminium rings and three connecting aluminium rods. A detailed description of the target cell can be found in [64].

4.1.4 Crystal spectrometer

Bragg's law The pionic hydrogen X-rays are emitted from the pionic hydrogen atoms formed in the target cell and are then reflected by the crystal spectrometer if Bragg's law

$$n\lambda = 2d \sin \Theta_B \quad (4.1)$$

is fulfilled. Here n is the order of reflection, λ is the wavelength of an incident X-ray, d is the crystal lattice spacing and Θ_B is the Bragg angle (Figure 4.6). Using $E = \frac{hc}{\lambda}$, with h as the Planck constant and c the speed of light, a direct relation of energy and Bragg angle can be established in (4.1).

Crystals Due to the requirement of high resolution for X-rays in the keV range, the only possible choice is quartz or silicon crystals. They exhibit a relative resolution of $\Delta E/E \approx 10^{-4}$ in the few keV energy region. In Figure 4.7 an example of the theoretical diffraction patterns (rocking curves) for plane crystals is shown.

The plots in Figure 4.7 suggest, that quartz crystals should be used during measurements, since they offer a higher (theoretical) reflectivity while having a resolution similar to silicon crystals. During the measurements of pionic X-ray transitions, however, it turned out,

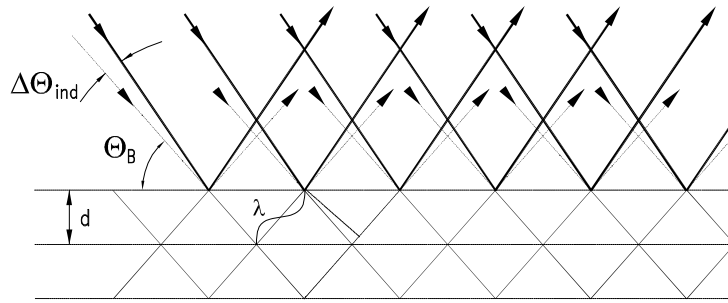


Figure 4.6: Illustration of Bragg's law. Reflected X-rays interfere constructively, if the Bragg condition (4.1) is fulfilled. $\Delta\Theta_{\text{ind}}$ is the necessary correction to the Bragg angle due to the index of refraction shift; for details see text.

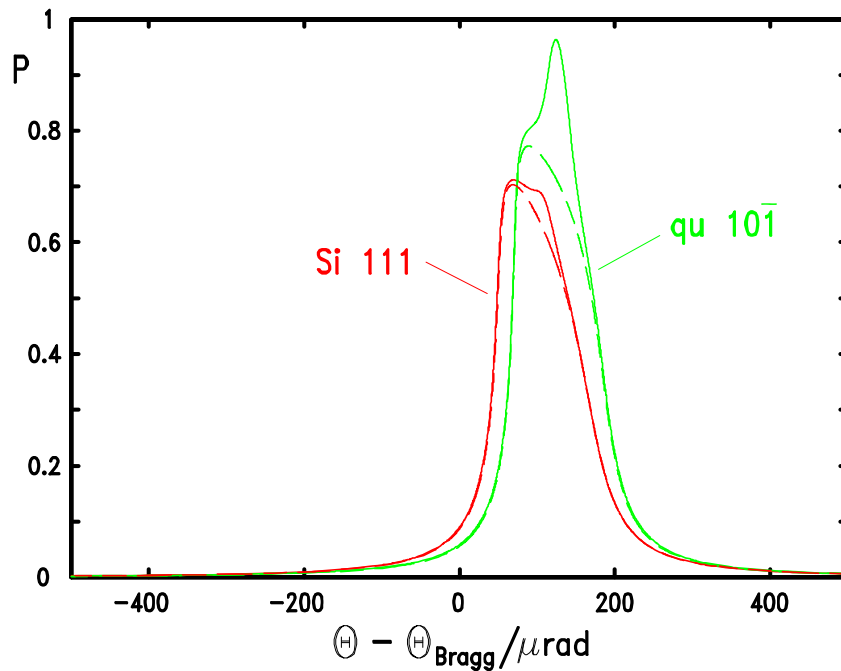


Figure 4.7: Rocking curves for flat silicon and quartz crystals produced by the X-ray Oriented Programs XOP [65]. The solid lines consist of the sum of σ - and π -polarisation. The dashed lines indicate the σ -polarisation only and nicely illustrate the effect of π -polarisation on the shape of the rocking curves.

that in reality this is not the case and the silicon crystals exhibit better reflectivity. Therefore, silicon crystals were used during all measurements of pionic hydrogen X-ray transitions described here.

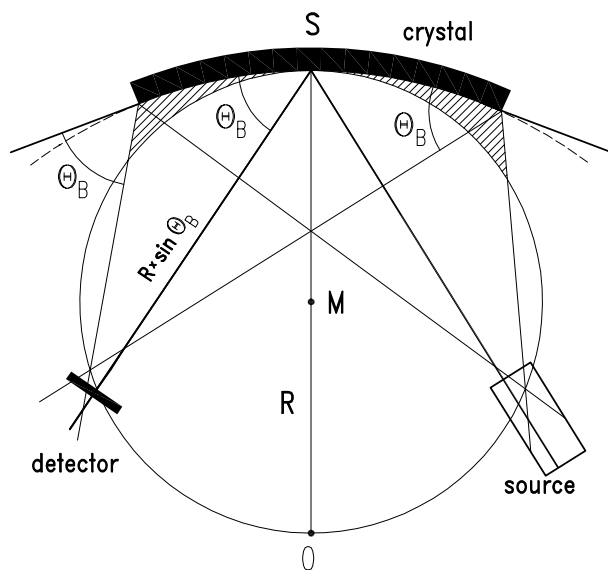


Figure 4.8: Schematic view of a crystal spectrometer in Johann setup.

Index of refraction correction An important correction to Bragg's law is caused by the so-called index of refraction shift. It is due to a change of the wavelength of X-rays after entering a crystal and hence causes a change of the Bragg angle of circa 1% for silicon and quartz crystals at low X-ray energies (Figure 4.6).

Johann setup For flat crystals, only a small region of the crystal surface fulfils the Bragg condition, which leads to a low rate of the reflected X-rays. In order to increase the rate of reflected X-rays, crystals are bent to an appropriate curvature. Bending the crystals changes the crystal lattice spacing d and therefore gives rise to another correction. d is also influenced by variations of the temperature which also has to be considered.

Already in the early times of X-ray spectroscopy the use of bent crystals in order to improve the efficiency of Bragg spectrometers was investigated. However, the development of a working method was hindered by the conclusion of a report by E. Wagner [66], which claimed that the fulfilment of both, the Bragg condition and the ordinary law of reflection, where the emission angle is equal to the incidence angle, is impossible to accomplish. It was found by Johann [67] that, by using a cylindrically bent crystal and an extended source, it is possible to simultaneously fulfil both constraints up to a small error which can be quantified. Using an extended (large area) detector, it is also possible to measure two lines with similar energy at the same time (see also Figure 4.2).

In the so-called Johann setup the bent crystal has a radius (R_C) twice the radius of the

Rowland circle (R), which is defined by the focusing condition

$$R = R_C \cdot \sin \Theta_B. \quad (4.2)$$

Furthermore, the source and the detector are placed on the Rowland circle, see Figure 4.8 for a sketch. Since the crystal is bent, it only touches the Rowland circle in one point where both conditions hold. X-rays deflected elsewhere on the crystal, will be reflected ("shifted") to the high energy side, leading to a broadening of the X-ray line on the detector (Figure 4.8). The farther away from the Rowland circle the crystal is, the larger the shift is. The maximal shift at the edge of the crystal reads

$$\Delta\Theta_J = \frac{1}{8} \left(\frac{b}{R_C} \right)^2 \cot^2 \Theta_B, \quad (4.3)$$

where b is the full horizontal width of the crystal and R_C is the bending radius of the crystal. By integrating over the whole crystal surface, the average shift is given in second order

$$\Delta\Theta_{\text{Johann}} = \frac{1}{3} \Delta\Theta_J = \frac{1}{24} \left(\frac{b}{R_C} \right)^2 \cot^2 \Theta_B, \quad (4.4)$$

which describes the so-called Johann-broadening. This purely geometric effect can be tolerated as long as it is small, compared to the resolution of the crystals. For crystals with large R_C , as used in this experiment, this is the case.

To increase the efficiency of a Bragg spectrometer even more, the Johann setup can be improved by bending the crystal spherically for partial vertical focusing, as described in [68]. For the sake of completeness the Johansson setup [69] shall be mentioned here, where the crystals are ground with a radius $R_C = 2 \cdot R$. Such, the crystal surface is tangent to the Rowland circle and the broadening introduced by the Johann setup is avoided. However, the grinding of such crystals is highly sophisticated.

The crystals used in the experiment and described herein have a diameter of 100 mm and are bent with a radius of approximately 3 m (Figure 4.9). By using adhesion forces, they are attached onto a glass lens with a diameter of 120 mm by the Carl Zeiss company [70]. The thickness of the crystals is approximately 0.2 mm for quartz and 0.3 mm for silicon.

The crystal surface available for Bragg reflection can be changed by placing apertures in front of it. Throughout the experiment a rectangular aperture of 60 mm width was used, which represents a compromise between rate and the extent of Johann broadening. As it is clear from equation (4.4), only horizontal limitation is needed in order to decrease the effect of the Johann broadening $\Delta\Theta_{\text{Johann}}$.

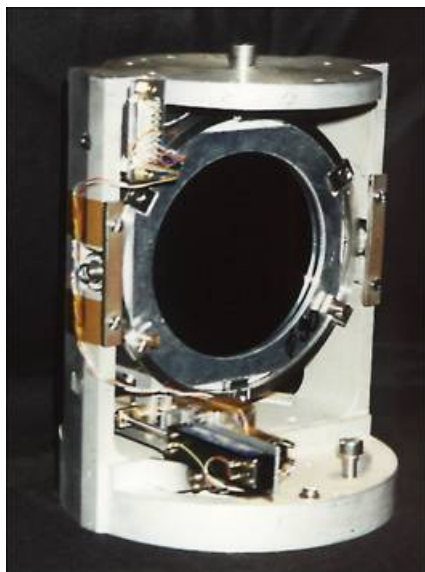


Figure 4.9: Picture of the crystal holder with a mounted silicon crystal.

4.1.5 Geometry of the spectrometer setup

In Figure 4.2 the principle of the measurement with schematics of the main parts is shown. In Figures 4.10 and 4.11 the different parts of the spectrometer attached to the crystal are shown in detail. On the target side, i. e., the side of the cyclotron trap, the crystal housing is connected to the target arm, which is fixed in its position (Figure 4.10). On the side of the detector, it is attached to the detector arm, which can be rotated by a stepper motor that controls the arm angle Θ_{ARM} (Figure 4.11). The crystal is controlled by another stepper motor, which rotates the crystal by the angle Θ_{CRY} . For the definition of Θ_{ARM} and Θ_{CRY} see Figure 4.12. Once Θ_{CRY} is set, it is stabilised by a ceramic piezo element, controlled by an angular encoder with an accuracy of ± 0.14 seconds of arc. The possibility of changing Θ_{ARM} and Θ_{CRY} individually has the advantage that by varying only Θ_{ARM} , a different region in the target can be chosen, without changing the position of the reflection on the detector. This is a very important feature of the setup, since it provides the possibility to "scan" the target. In a "target scan", the arm angle Θ_{ARM} is varied and is plotted versus the X-ray rate (Figure 4.13). For the measurement of a specific X-ray transition in pionic hydrogen, Θ_{ARM} is set to a value where the rate is maximal. A detailed investigation of the features of a crystal spectrometer is performed in [71].

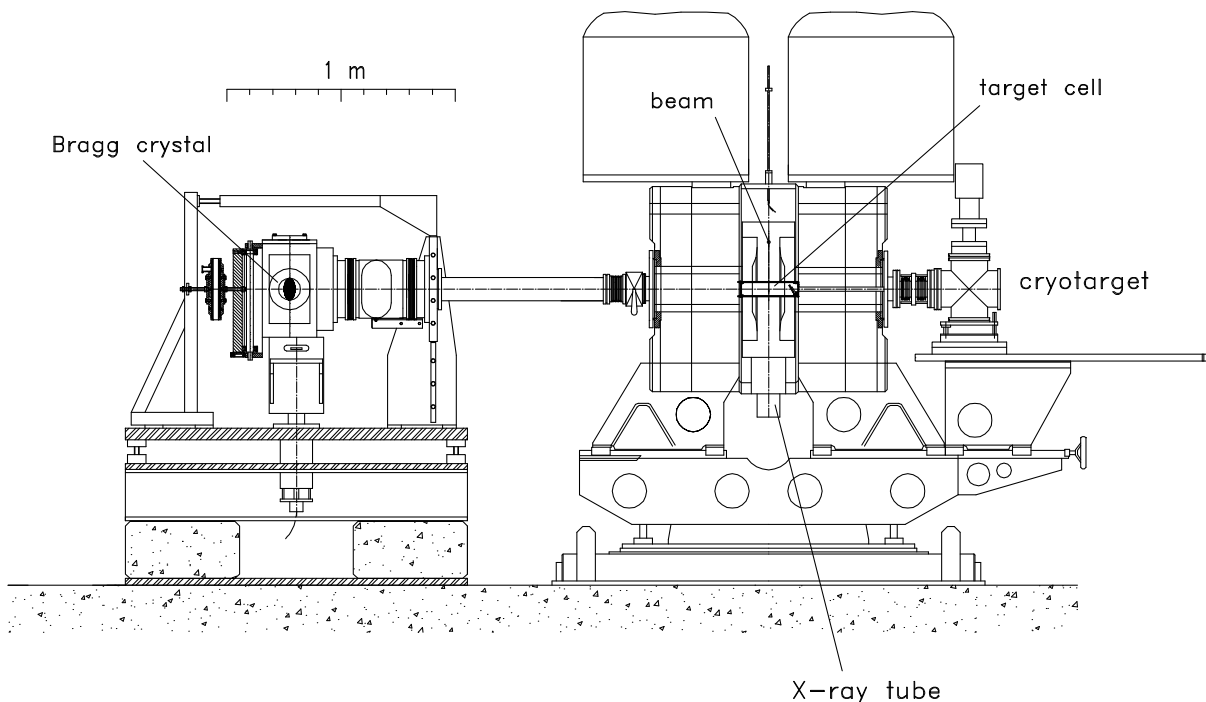


Figure 4.10: Drawing of the cyclotron trap attached to the crystal. On top of the cyclotron trap, the two helium tanks providing the cooling of the superconducting coils of the magnet are indicated. On the right, the construction allowing the axial movement of the target can be seen. For the measurement the space between the Bragg crystal and the cyclotron trap is completely filled with concrete, see Figure 4.3.

4.1.6 CCD detectors

The main energy region of interest in the pionic hydrogen experiment is of the order of 2-3 keV. Since the countrate is also expected to be very low (< 100 X-rays/h), a detector with good quantum efficiency in this region is needed. Additionally, due to the high background expected in the experimental area, background reduction capabilities are also desired. Therefore an array of charge coupled devices (CCDs) was chosen as detector. A detailed description of the CCD22 used in this experiment can be found in [72]. Here a short summary of the main features of the used CCD detector will be given.

The whole detector is comprised of 6 CCD devices. Each device has 600×600 $40 \mu\text{m}$ square pixels. This makes an active area of $24 \text{ mm} \times 24 \text{ mm}$ for each device. The CCD22 has a depletion depth of $\sim 30 \mu\text{m}$ and the quantum efficiency in the region of interest is about 80-90%.

The CCD22 is able to operate in frame-transfer mode, which allows the image region to be shifted to a storage area within less than 20 ms. That way, provided the integration

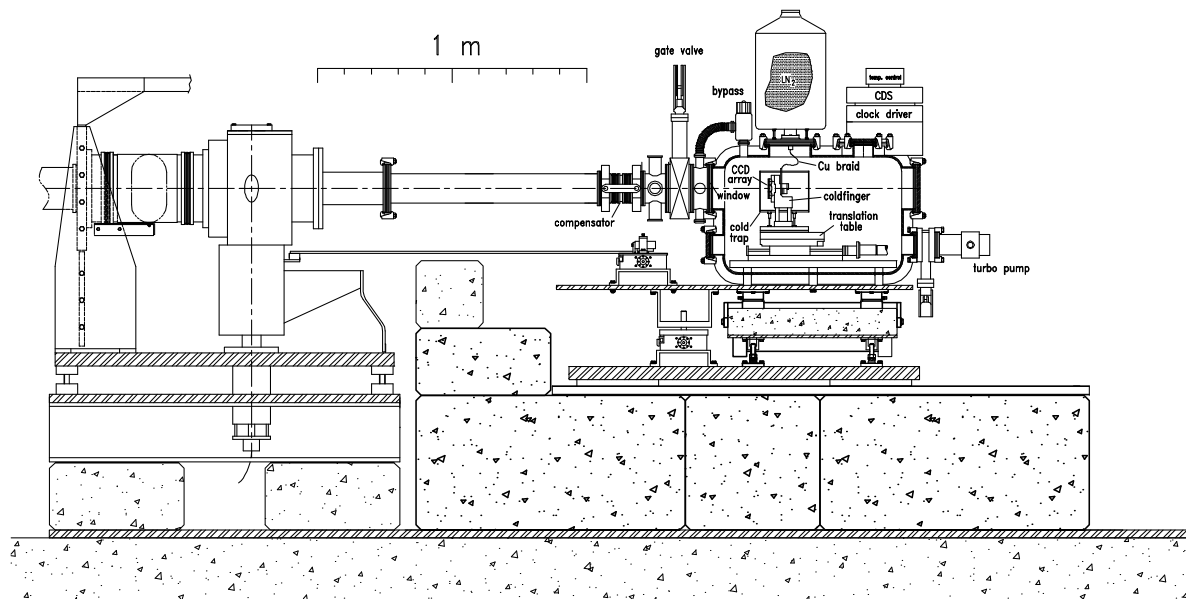


Figure 4.11: Drawing of the crystal and the housing containing the CCD detector.

period is larger than the read-out period, losses are eliminated.

The 6 CCDs are mounted in a 2 column by 3 row array, which gives a imaging area of $48\text{ mm} \times 72\text{ mm}$ with a gap of about $500\ \mu\text{m}$ between the individual CCDs (Figure 4.14). Ideally, the six CCDs would be mounted perfectly aligned to each other. In reality, however, there are gaps between the CCDs and the individual devices are slightly askew, with relative rotations of about 1-6 mrad. The relative rotations of the individual CCDs have been measured and were determined with a precision of about $50\ \mu\text{rad}$ in [73].

In order to minimise the thermally induced dark current, the CCDs are mounted on a cold-finger and are cooled using liquid nitrogen. A closed loop control maintains the CCD temperature at $-100 \pm 0.5^\circ\text{C}$.

The cold-finger (with the CCD array attached to it) is mounted on a high-precision translation table (called "LinTab"), which allows the detector to be moved (over a range of 86 mm), in order to position it at the calculated focal position of the crystal in use without breaking the vacuum.

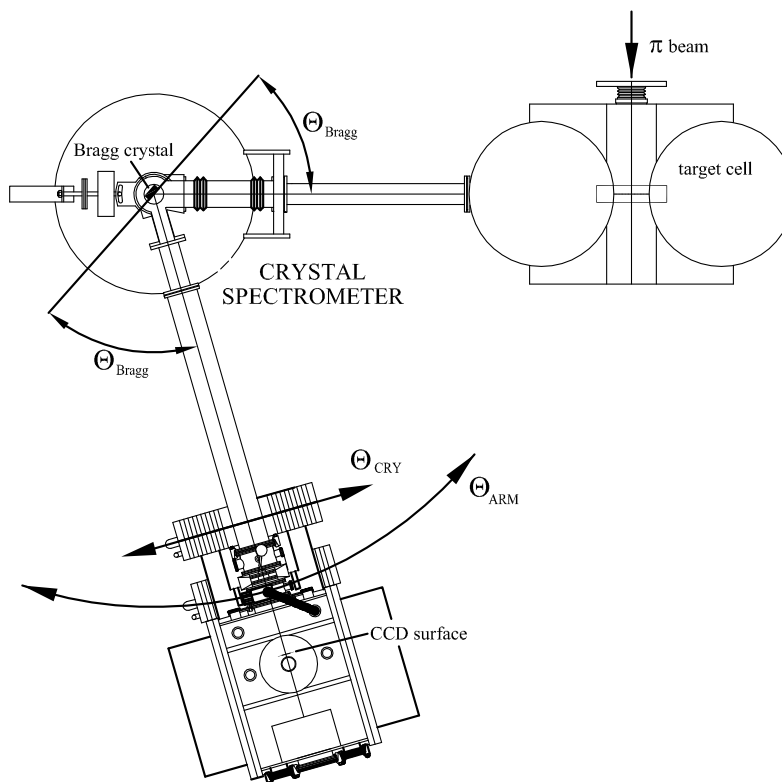


Figure 4.12: Illustration of the setup geometry with the angular degrees of freedom indicated by arrows. For details see text.

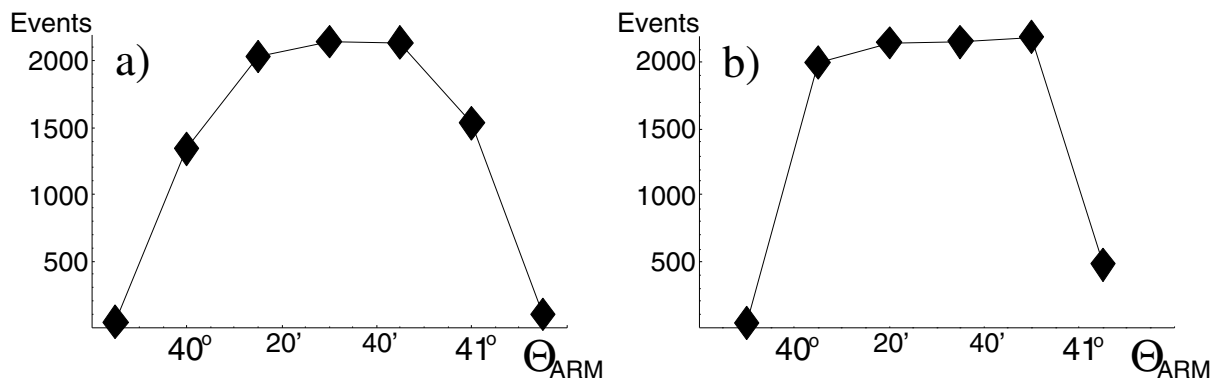


Figure 4.13: Examples of target scans performed prior to data taking. For the target scan on the right, an additional rectangular aperture was attached on the target window. The sharp edges allow a quick determination of the optimal setting of Θ_{ARM} . Figure taken from [8].

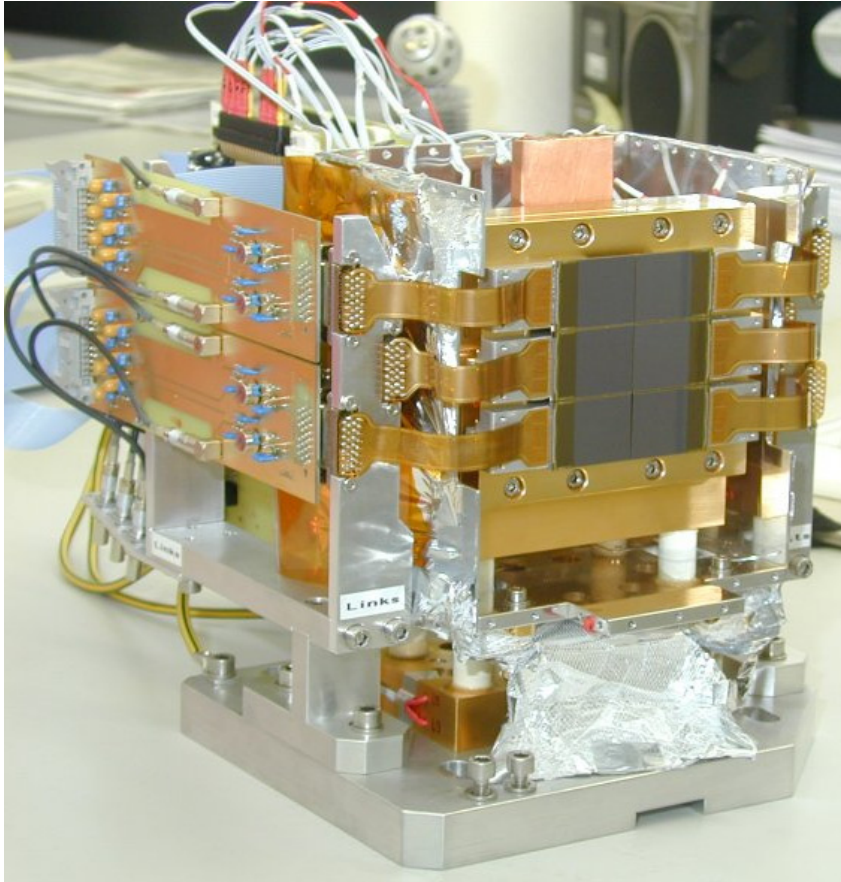


Figure 4.14: Picture of the CCD array comprising the large area detector used in the experiment.

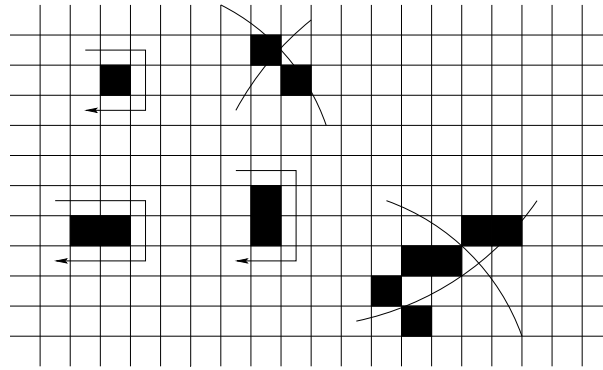


Figure 4.15: The cluster analysis separates pionic hydrogen X-rays (single or paired events) from background events (multipixel events).

4.2 Data processing

4.2.1 Cluster analysis

As already mentioned earlier, pions stopping in matter produce a high neutron background by absorption: $\pi^- + A \rightarrow A' + nn$. The neutrons interact with the surrounding matter and finally high energy γ -rays are produced via the reaction $n + A \rightarrow A'^* \rightarrow A'\gamma$. The detector can be shielded from neutrons with concrete by moderation of the neutrons in its water content. Especially, it is important, that the region between the crystal and the source (cyclotron trap) is well shielded (about 1 m of concrete), see Figure 4.3.

The γ -rays can reach the detector and produce multi-pixel events by charge splitting. In order to suppress such events from being taken into account in the production of the final spectrum, a cluster analysis has to be performed. The cluster analysis makes use of the different structure of background events and events originating from pionic hydrogen X-rays. Since X-rays from transitions in pionic hydrogen are in the order of a few keV only, they result in one activated pixel or two adjacent activated pixels. Whereas the high energy γ -rays form large clusters (Figure 4.15).

4.2.2 ADC-cuts

A further reduction of the background is achieved by applying energy cuts (ADC-cuts) to the cluster analysed data. With energy cuts, a region around the X-ray line of interest is selected (Figure 4.16). In order to be able to identify the line, a suitable energy calibration has to be performed. Once the line is identified, it is fitted using a Gaussian profile to determine its position and width. Afterwards, regions with widths from 1σ up to 3σ around the peak are selected and taken for further analysis.

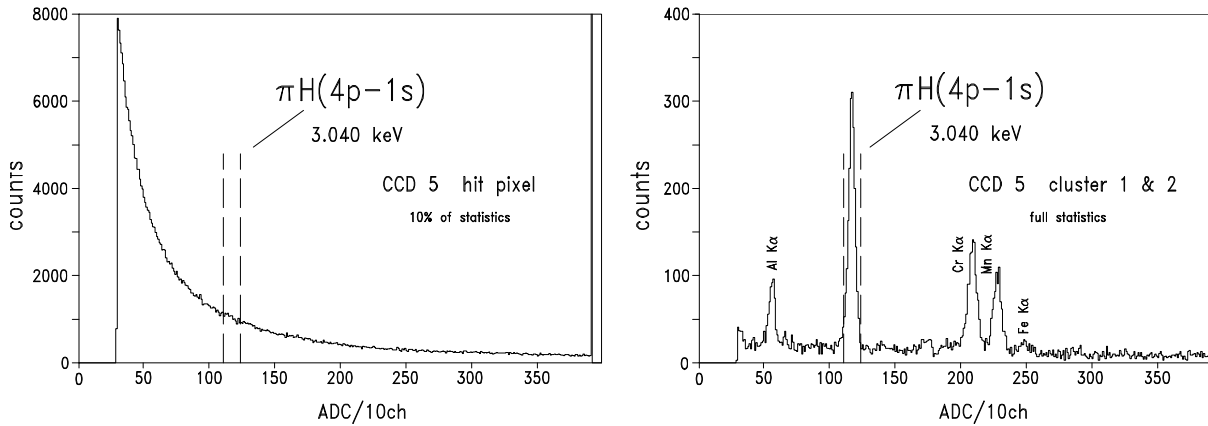


Figure 4.16: ADC-spectrum before cluster analysis (left) and after cluster analysis (right). The ADC-cut is indicated by dashed vertical lines.

Applying the cluster analysis and energy cuts to the data has a drastic effect, as can be seen in Figure 4.16. A detailed description of the cluster analysis used here can be found in [8].

4.2.3 Bad pixel map

There is also the possibility of damaged pixels, which are activated without being hit by an X-ray. To avoid that these pixels are taken into account, a bad pixel map (BPM) can be established. With the BPM a threshold is set, which defines above what number of hits a pixel is called defect. To find a suitable threshold, a first BPM is applied and it is checked how this BPM influences the produced spectrum. Finally, a compromise has to be found such, that as few interesting events as possible are ignored in the spectrum.

4.2.4 Curvature correction

After the application of cluster analysis, ADC-cuts and the BPM, a "clean" two dimensional spectrum is obtained (Figure 4.17). In this spectrum, however, all effects according to geometry are still included: CCD alignment relative to each other (see section 4.1.6) and curvature. The curvature is due to the fact, that a monochromatic X-ray line, reflected at a crystal spectrometer results in a curved reflex on a flat detector. In order to obtain a one dimensional spectrum which can be used for the final analysis, these effects have to be accounted for.

Here the consequences of the curvature correction will be summarised shortly. For a thorough investigation the reader is referred to [8].

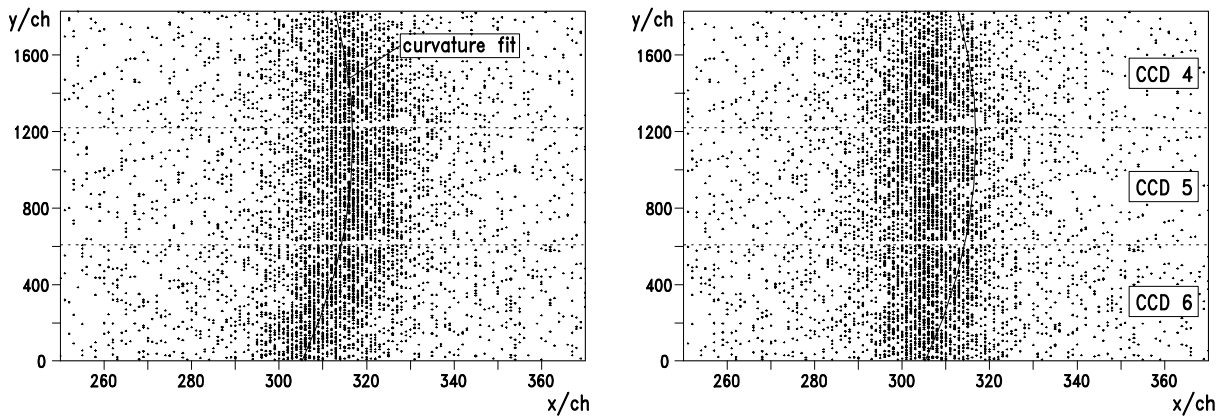
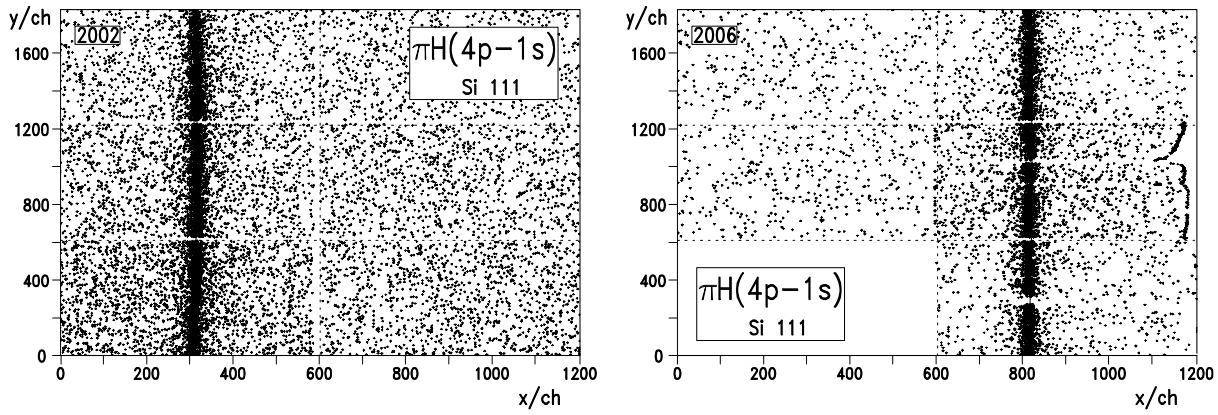


Figure 4.17: Effect of the application of a curvature correction to the cluster analysed data shown in a two dimensional plot of the data ("scatter plot"). The parabola parametrising the curvature is indicated by a solid line.

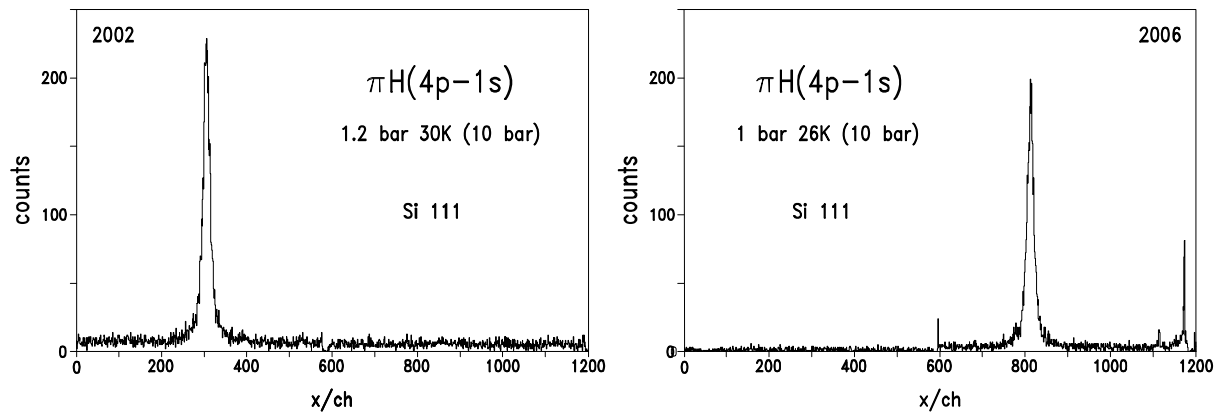
The Bragg-reflection of a point-like source results in a hyperbolic image on a flat detector. By using an extended source, the image on the detector is a superposition of all hyperbolas resulting from the individual points constituting the extended source. If the reflection surface is a curved crystal, and if the size of the crystal surface is small compared to its bending radius, then the curvature of the reflex on a flat detector can be parametrised by a parabola $f(x) = ax^2 + bx + c$. Once the parameters a , b and c are obtained via a χ^2 analysis, the curvature correction can be performed.

Figure 4.17 shows the effect of the curvature correction. The application of a curvature correction is very important, since, if not applied, the one dimensional projection of the curved spectrum leads to a distorted line shape.

Finally, a one dimensional spectrum is obtained, which can be subjected to an elaborate analysis (Figure 4.18). The spectrum produced in this way, serves as a basis for a fit routine developed separately. The analyses necessary in the following chapters will be performed using this fit routine. The fit models used will be explained in the sections where they are applied.



(a) Two dimensional plots of data.



(b) One dimensional position spectrum.

Figure 4.18: Two dimensional plots of data and one dimensional position spectra of the $4p \rightarrow 1s$ transition measured in the years 2002 and 2006. The structure seen in Figure 4.18(a) right is due to the malfunction of the CCD chip and will be cut away.

5 The spectrometer response function

5.1 The Electron Resonance Ion Trap – ECRIT

In order to be able to extract the width of the ground state in pionic hydrogen with sufficient accuracy, the response function of the spectrometer has to be known. The underlying idea is to use narrow X-ray lines with the same, or very similar, energies like the $4p \rightarrow 1s$, $3p \rightarrow 1s$ and $2p \rightarrow 1s$ transitions in pionic hydrogen, which have the energies 3.043, 2.886 and 2.436 keV, respectively.

Accuracy is the outstanding requirement of this experiment. A prerequisite to compass that requirement, is the accurate determination of the spectrometer response function. In Figure 4.7 examples of rocking curves of quartz and silicon are plotted. They exhibit a complicated shape and hence no simple model is applicable. Their shape is asymmetric and, most importantly, they have Lorentz-like tails. Additionally, due to the use of a spherically bent crystal setup, the imaging is also complicated.

Because of the shape of the tails, the measurement of the response function is of high relevance for the extraction of the hadronic width of the ground state in pionic hydrogen, since otherwise the influence of the Lorentz-like tails originating from the response function may be attributed to the strong interaction, which is of the same shape.

In order to account for these circumstances accurately, the response function requires a few 10 000 events in the line. Furthermore, this measurement has to be performed with the whole experimental setup as it is used for the measurement of the pionic hydrogen X-rays, since the whole geometry of the setup has to be accounted for.

There were already attempts to measure the response function using fluorescence targets, excited by X-ray tubes. Unfortunately, due to Auger transitions, X-rays produced in such a way possess a natural line width much broader than the resolution of the spectrometer. In principle, narrow transitions from other exotic atoms (such as X-rays from the $5g \rightarrow 4f$ transition in π^-C [8]) could be used to measure the response function. However, this approach turns out not to be adequate for a precise determination, since the expected rate of X-rays is in the order of $\sim 50/h$ only.

An alternative way of combining the requirement of narrow X-ray lines and high rate is the usage of highly ionised atoms, like they can be produced in electron cyclotron resonance (ECR) sources. For low to medium Z atoms, the hydrogen-like E1 and helium-

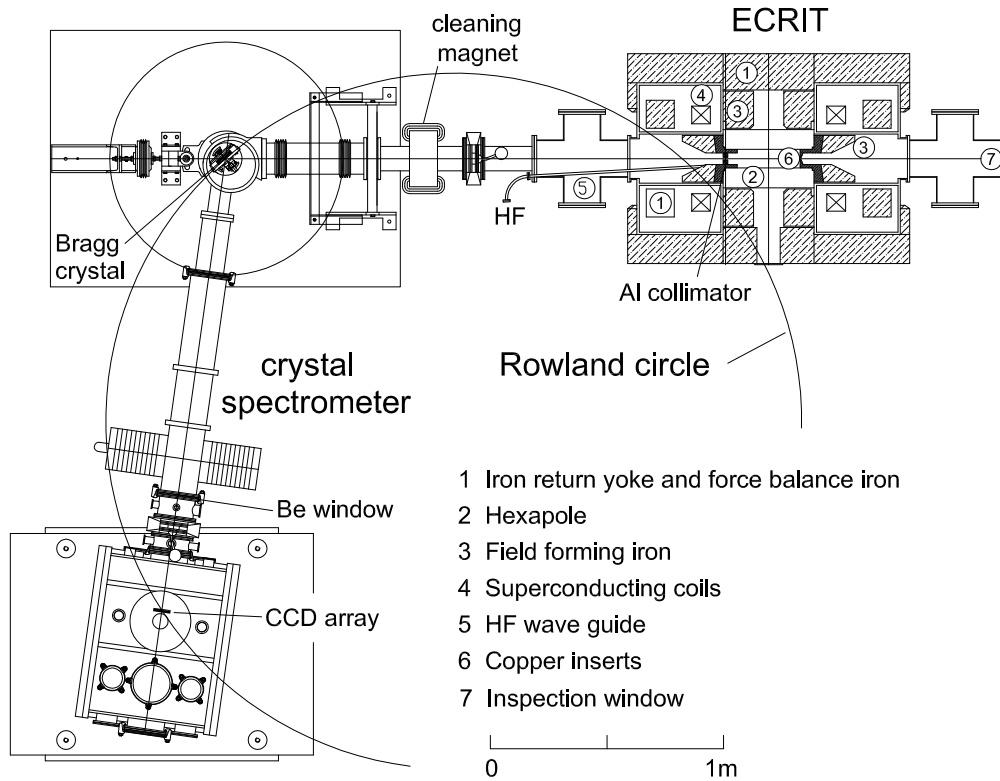


Figure 5.1: Setup of the ECRIT at PSI – the main components are indicated. The figure is taken from [78].

like M1 X-rays have natural line widths sufficiently small to satisfy the requirements of the experiment. The M1 line in helium-like argon for instance has a lifetime of $0.2 \mu\text{s}$ [74]. Another important feature of ECR sources is, that the kinetic energy of the ions is less than 1 eV [75, 76] and hence Doppler broadening of less than 40 meV is to be expected in the He-like argon M1 line ($\sim 3 \text{ keV}$). In principle also EBIT (electron beam ion trap) sources could be tuned to low kinetic energies of the captured ions, but this would result in a drastic reduction in intensity. Therefore, an electron cyclotron ion resonance trap (ECRIT) [77] was developed and set up at PSI.

5.1.1 Experimental setup

The setup of the PSI-ECRIT is depicted in Figure 5.1. Like in the setup for the measurement of pionic hydrogen X-rays, the experimental setup to determine the spectrometer response function consists of three parts:

- The electron cyclotron resonance ion trap – ECRIT, which is the modified cyclotron trap as used in the $\pi^- \text{p}$ measurements.

- The crystal spectrometer.
- The CCD detector.

The ECRIT consists of the existing cyclotron trap with special iron inserts, which provide the mirror field configuration. In the axis of the cyclotron trap a permanent hexapole magnet is mounted. The hexapole magnet is cooled by a forced flow of demineralised water. The mirror ratio produced by this device is one of the highest achieved for ECR sources and has a value of 4.3 over the length of the chamber.

Additionally, a 6.4 GHz power-regulated microwave emitter for the ignition of the plasma is used. The microwave high frequency power is directly introduced into the plasma chamber.

Without plasma, a pressure in the order of some 10^{-8} mbar was reached. The pumping was done by three turbo molecular pumps and one cryo-pump. The gas for the plasma was filled in radially via UHV precision leak valves and the gas composition was monitored by a quadrupole mass spectrometer.

In the vacuum tubes connecting the crystal spectrometer with the ECRIT and the CCD detector system, valves were mounted, such that the crystal and the attached apertures could be changed while the ECRIT and the detectors were active. All details of the experimental setup of the PSI-ECRIT can be found in [78, 79].

5.1.2 Experimental procedure

In the pionic hydrogen experiment three transitions (the $4p \rightarrow 1s$, $3p \rightarrow 1s$ and $2p \rightarrow 1s$) were measured. Two different crystals were used: a Si(111) and a quartz (10–1). In order to characterise the two crystals used in the experiment, X-ray lines which are close to the one coming from pionic hydrogen have to be used. Therefore, the PSI-ECRIT was tuned to produce narrow X-ray lines from highly charged sulphur, chlorine and argon. In Table 5.1 the energies from the pionic transitions are confronted with the helium like X-ray energies from the three gases. Since the relative resolution of the crystal spectrometer is of the order 10^{-4} , the helium-like transitions overlap well with the pionic hydrogen X-rays in question and no extrapolation is necessary.

In order to produce a high intensity spectrum, the ECRIT had to be tuned. The optimum for the high-frequency power was found at about 450 W. The highly ionised gas in an ECRIT is produced by collisions of electrons with atoms. Therefore, O₂ gas was added to provide additional electrons. The gas mixture had to be optimised in order to obtain a high intensity of X-rays from highly excited ionised atoms. For argon, for instance, the optimal mixture of Ar/O₂ was 1/9. Figure 5.2 shows a picture of the plasma taken through the inspection window at the ECRIT.

ECRIT				π^-p		
Crystal	Gas	θ_B [°]	E_X [eV]	Transition	θ_B [°]	E_X [eV]
Quartz	Ar	36.6814	3104.18	4p→1s	37.5443	3043.00
	Cl	42.2687	2756.92	3p→1s	39.9804	2886.00
	S	49.7269	2430.40	2p→1s	49.5441	2437.00
Silicon	Ar	39.5608	3104.18	4p→1s	40.5191	3043.00
	Cl	45.8171	2756.92	3p→1s	43.2392	2886.00
	S	54.4357	2430.40	2p→1s	54.2192	2437.00

Table 5.1: Comparison of the transition energies originating from pionic hydrogen to the energies from the helium like lines in argon, chlorine and sulphur. For quartz(10 – 1) $2d = 6.686277 \text{ \AA}$ and for silicon(111) $2d = 6.2712016 \text{ \AA}$. d is the crystal lattice spacing.

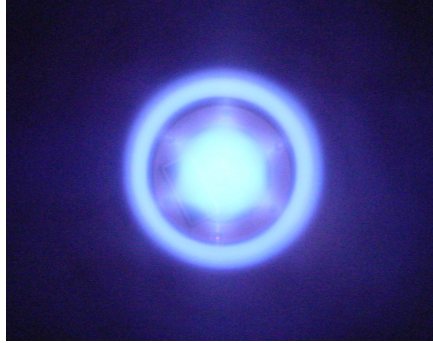


Figure 5.2: Picture of the argon plasma inside the ECRIT at PSI. Picture taken from the inspection window at the ECRIT.

Once the ECRIT settings are optimised, a target scan (see section 4.1.5) and a focal scan are performed, in order to have the optimal setting of the spectrometer for the M1 X-ray transition. In a focal scan the position of the detector is optimised such, that the width of the line at a given position of the detector is minimised. In Figure 5.3 an example of a spectrum for the argon M1 X-ray transition is depicted.

5.2 Determination of the spectrometer response function

The starting point of the determination of the spectrometer response function is the rocking curve of a flat ideal crystal. This rocking curve is used as a basis for the real response function of the spectrometer, which of course also has to incorporate the whole

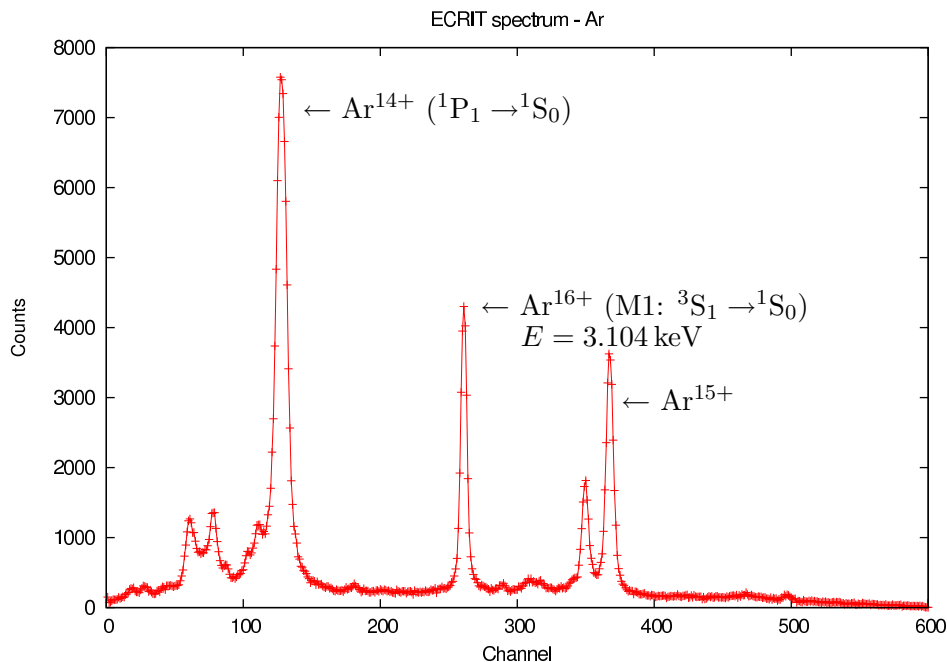


Figure 5.3: Argon X-rays from Ar¹⁴⁺, Ar¹⁶⁺ (M1 line) and Ar¹⁵⁺ measured with a quartz (10 – 1) crystal. The energy value is taken from [74].

geometry of the setup.

XOP response function The rocking curve of a flat ideal crystal can be provided by a program package such as the X-ray Oriented Programs (XOP) [65] (Figure 5.4(a)).

XOP + geometry To include geometrical effects such as source size, crystal and detector properties, and relative alignment of the setup, a Monte Carlo X-ray tracking routine was developed, which uses the XOP response function as input and calculates the Bragg reflection of a spherically bent crystal, including all geometrical properties of the experimental setup. A major benefit from the X-ray tracking routine is, that by changing several parameters representing the experimental setup in the tracking routine, a detailed investigation of the effects on the X-ray spectrum, resulting from these changes is possible. After application of the X-ray tracking routine, a two dimensional image on the detector is obtained (Figure 5.4(b)). To this spectrum a curvature correction has to be applied and has to be projected onto the x-axis in the same way as the measured spectra. Finally this one dimensional spectrum can be used for the further investigation described below. The output of the tracking routine can be considered as the ideal, theoretical response function, which under ideal circumstances would reproduce the data.

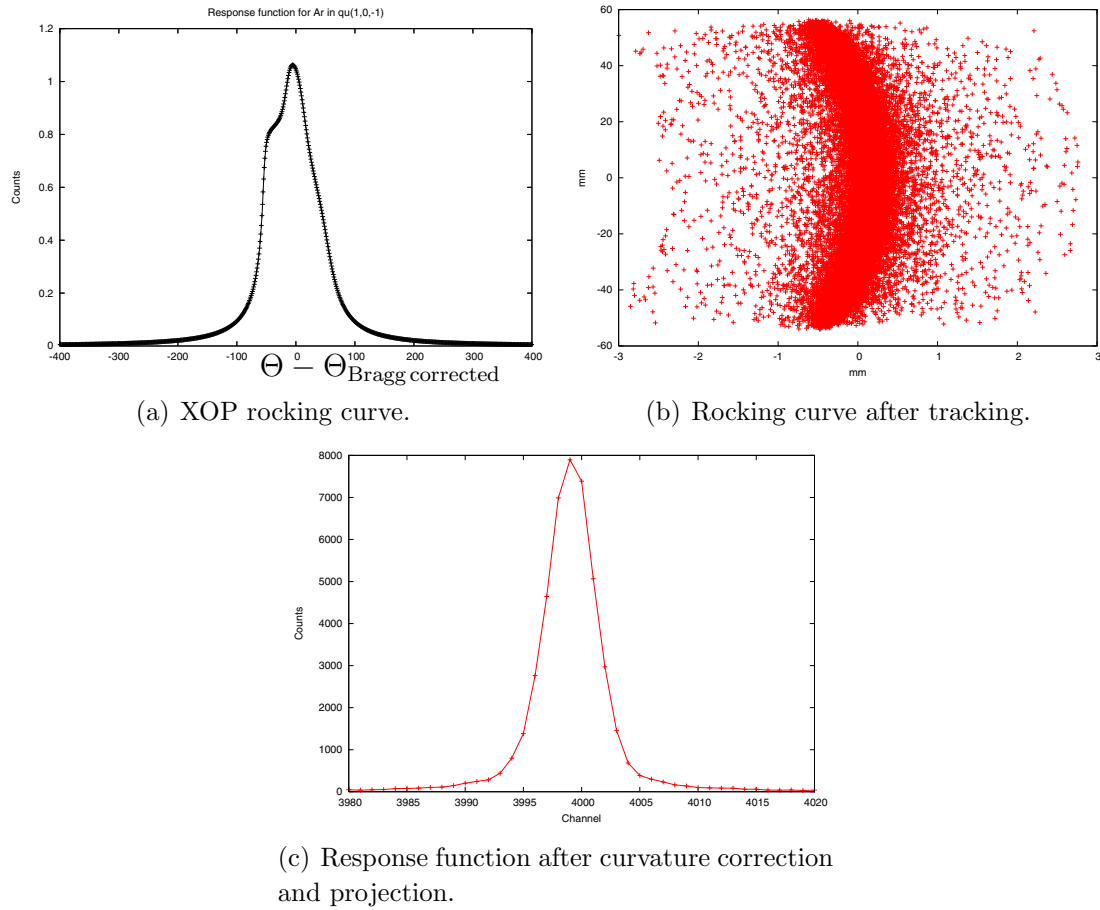


Figure 5.4: The evolution of the rocking curve for the argon M1 line calculated by XOP is shown. First tracking is applied (Figure 5.4(b)), then a curvature correction and a projection onto the x-axis is performed (Figure 5.4(c)).

XOP + geometry + Gaussian Deviations from the ideal situation, such as for instance imperfections of the crystal, could be parametrised by a simple additional Gaussian broadening. Using the tracking routine, this additional Gaussian can be folded into the ideal response function and that way additional broadening effects can be included. In fact, by varying the distance of the detector from the crystal, it turned out that this additional Gaussian broadening is the same for all settings of the crystal–detector distance [78]. This clearly indicates, that this Gaussian broadening is due to crystal properties and not due to geometrical effects.

It is this additional Gaussian broadening which is of interest. Its determination will be explained in section 5.2.2.

5.2.1 Definition of the spectrometer focus

In order to provide a systematic approach to determine the additional Gaussian broadening, at first, a few basic considerations have to be made and the term "focus" has to be defined. As the focal position is defined, the position of the detector for which the width of measured line is minimal.

The so-called focal scan, that is, varying the distance crystal–detector, allows the determination of the focal position, which generally is close to the calculated focal position: $R_C \cdot \sin \Theta_B$. Usually the scan is performed in steps of ~ 2 mm. At each detector position, data are taken for 20 minutes. Immediately after data acquisition, a first rough analysis of the line width is performed by means of a Voigt profile. From this evaluation a focal position (position with minimal line width) is determined already in good approximation. However, the shape of the rocking curve is in general too complicated to be reproduced by a symmetric Voigt profile. This leads to an incorrect focal position and the detector is placed at a position slightly off the "real" focus (which has to be treated as unknown up to now). This displacement of the detector results, of course, in an additional broadening of the response function and should not be associated with the additional Gaussian broadening, which is expected to account only for broadening caused by imperfection of the crystal.

It follows, at first the extent of the misplacement of the detector has to be determined. That is, the distance of the nominal focus, which was used during the measurement of the spectrometer response function, from the "real" focus.

Once this value is known, a spectrum with the detector shifted by this value, can be simulated with the X-ray tracking routine. The spectrum obtained that way represents the theoretical response function with the detector at the real focal position and thus can be compared to the spectrum measured at (or closest to) this real focal position. Only now the additional Gaussian broadening can be quantified.

Crystal miscut Another parameter that influences the focal position is the so called miscut of the crystal. During the detailed investigation of all geometrical properties of the spectrometer, it was discovered, that the crystallographic planes are not parallel to the surface of the crystal. Therefore the simple focal condition given by

$$F = R_C \cdot \sin \Theta_B \quad (5.1)$$

has to be changed to

$$F = R_C \sin \Theta_B + R_C \cos \Theta_B \sin [\alpha \cos(\Phi - \Phi_0)], \quad (5.2)$$

where F is the focus, R_C is the curvature radius of the crystal, Θ_B is the Bragg angle, α is the angle of the miscut, Φ_0 is the orientation of the miscut and Φ represents the

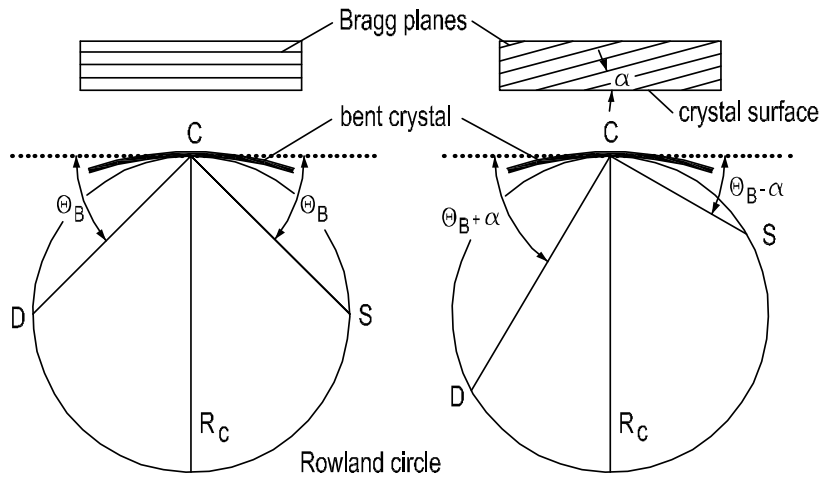


Figure 5.5: Schematic drawing of the crystal miscut. Ideally the crystal planes are parallel to the surface (left). Figure taken from [80].

Crystal	Plane	Miscut α [°]	Orientation Φ [°]
Qu - Z20	(1, 0, -1)	0.034 ± 0.0013	-3 ± 21
Qu - Z21	(1, 0, -1)	0.011 ± 0.0011	-58 ± 56
Si - Z13	(1, 1, 1)	0.288 ± 0.006	-87.4 ± 1.2

Table 5.2: Miscut for some crystals.

orientation of the crystal during the measurement (Figure 5.5). A detailed investigation of measurement and the influence of the miscut can be found in [80, 81]. In Table 5.2 examples for the miscut of the used crystals are given. Apparently the miscut of the quartz crystals is very small and is thus negligible. For silicon, however, it can not be neglected, since this would prevent an accurate determination of the defocusing. Therefore, the influence of the miscut was implemented into the X-ray tracking routine as well.

5.2.2 Determination of the additional Gaussian broadening

In this section the procedure to extract the additional Gaussian broadening will be described in detail. Even though the analysis using a Voigt profile used during the focal scan is wrong only for ~ 2 mm (as will be found out in the following), this displacement has an effect on the additional Gaussian broadening, which should be attributed only to geometrical deformations of the crystal and not to a broadening induced by a displacement of the detector. The whole procedure has to be repeated for each transition energy and each crystal.

Description of the procedure Starting point is the spectrum taken at the nominal focal position determined in the focal scan, together with the simulated theoretical response function (XOP + X-ray tracking) simulated at the nominal focus with $\Delta x = 0$ and $G = 0$. Δx and G are input parameters in the Monte Carlo X-ray tracking routine. Δx is variable and describes shifts of the detector in direction and away from the crystal. G is the additional Gaussian broadening, which is set to zero at the beginning of the procedure. Another important quantity has to be defined: "LinTab". It is an arbitrary quantity from the experimental setup, representing the detector position on the linear table (see also section 4.1.6). Therefore, the numerical value for the nominal focus is given by LinTab. Both spectra (the data from the ECRIT measurement and the theoretical response function produced at the nominal focus ($\Delta x = 0$)) are read into the fitting routine and a fit to the data is executed. The result of this fit is a value for the Gaussian broadening which is kept fixed in the further analysis.

Next, several ECRIT spectra farther off the nominal focus are chosen. For each of them several theoretical response functions are produced, but they are slightly shifted from the value the detector is set in the focal scan. In other words, during the focal scan the detector is set to a position a from the nominal focus. The theoretical response functions are produced "around" this value, i. e., $\Delta x = a \pm \Delta a$, where $\Delta a \approx 5$ mm in steps of 0.5 mm. Each of these in such way produced theoretical response functions is read into the fitting routine and a fit to the ECRIT data taken at a is performed, with the Gaussian broadening fixed at the value obtained at the start of the procedure.

In this way, a χ^2 distribution as a function of the distance from the nominal focus Δx is obtained (Figure 5.6 displays an example). This χ^2 distribution is fitted using a polynomial of third order. The minimum of this distribution is identified as the distance from the "real" focus, the detector was set in the focal scan. As can be seen in Figure 5.6, for spectra taken far off the focus, the method described here is more sensitive. Therefore, the outermost points of each focal scan were taken for the determination of the focal position.

This is repeated for several points off the nominal focus. For each of these points a "real" focus is found. Finally, from these values a weighted mean is calculated and thus the focus of the spectrometer is found. The formula for the weighted mean is given by

$$F = \frac{\sum_i f_i \cdot \frac{1}{(\Delta f_i)^2}}{\sum_i \frac{1}{(\Delta f_i)^2}} \quad (5.3)$$

and for the error

$$\frac{1}{(\Delta F)^2} = \sum_i \frac{1}{(\Delta f_i)^2} \quad (5.4)$$

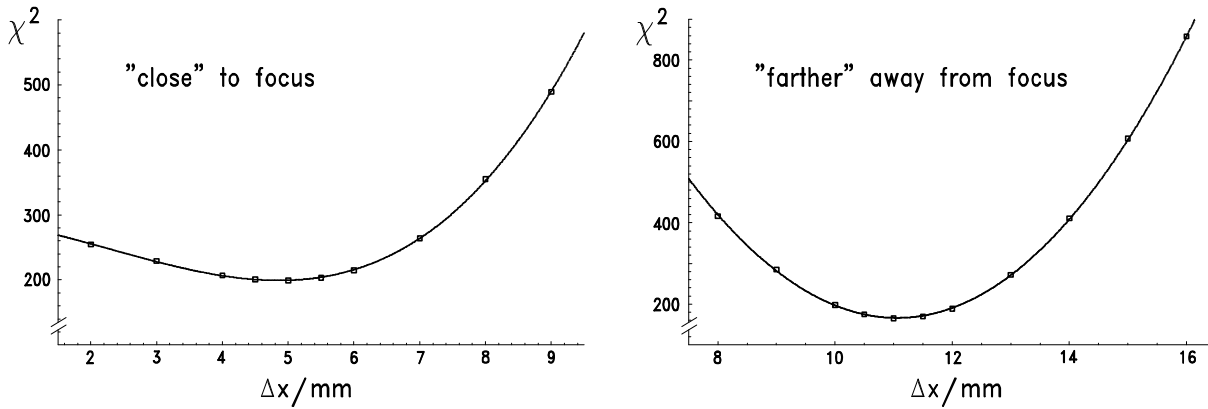


Figure 5.6: χ^2 distribution as function of the distance from the focus Δx .

was used (see e. g. [82]). f_i are the different foci obtained for the different spectra at the different positions of the focal scan, Δf_i are the corresponding errors.

In Table 5.3 the results for the foci for two quartz (10 – 1) crystals (Z20 & Z21) and one silicon (111) crystal (Z13) are summarised. In this work only quartz crystals were analysed. The result for the silicon crystal was taken from [28]. In addition, since the $3p \rightarrow 1s$ transition in pionic hydrogen was always measured with a silicon crystal, only argon and sulphur were used for determining the response function of the quartz crystals.

5.2.3 Results for the additional Gaussian broadening

With the focal position defined for the respective crystals, the additional Gaussian can be determined: First, a theoretical response function at the correct focal position has to be simulated. After this, the measured spectrum with the setting of the linear table closest to the correct focus has to be identified. And ultimately, this measured spectrum has to be compared to the theoretical response function produced at that position.

The result from this fit is the additional Gaussian broadening, which is expected to account for all broadening effects that are not included in the theoretical calculation of the rocking curve in XOP. The results for the different crystals are found in Table 5.4.

Discussion of the procedure The procedure to find the additional Gaussian broadening starts with the Monte Carlo simulation of the theoretical response function with $\Delta x = 0$ and additional Gaussian $G = 0$. After the "real" focus is identified, the additional Gaussian broadening can be determined.

The assumption is, that this additional Gaussian accounts for all additional broadening

Crystal	Gas	F_{nominal} [mm]	F_{weighted} [mm]	Δx [mm]
Z20	Ar	97.98 ± 0.20	96.86 ± 0.08	$+1.12 \pm 0.21$
	SO ₂ (1)	94.87 ± 0.20	93.57 ± 0.21	$+1.30 \pm 0.29$
	SO ₂ (2)	91.87 ± 0.20	92.72 ± 0.55	-0.85 ± 0.58
Z21	Ar	97.72 ± 0.20	97.16 ± 0.07	$+0.56 \pm 0.21$
	SO ₂	94.87 ± 0.20	93.19 ± 0.25	$+1.68 \pm 0.32$
Z13	Ar	97.04 ± 0.20	97.50 ± 0.16	-0.46 ± 0.26
	Cl	91.96 ± 0.20	90.92 ± 0.20	$+1.04 \pm 0.28$
	SO ₂	130.00 ± 0.20	129.88 ± 0.34	$+0.12 \pm 0.39$

Table 5.3: Results for the real foci (F_{weighted}), confronted with the foci obtained during the measurement (F_{nominal}). Δx is the difference between the nominal and the correct focus. A negative sign for Δx corresponds to a direction away from the crystal. Z20 and Z21 are synonyms for two quartz crystals. In the case of quartz and sulphur, two focal scans were performed (1 + 2). The results for Z13 are taken from [28].

effects not included in the theoretical model used in the XOP. However, it could be argued, that this additional Gaussian is only a first approximation which could be improved by another iteration of the whole procedure. That is, to use that additional Gaussian as input at the beginning of the procedure (instead of $G = 0$) and repeat the whole procedure and that way determine an improved additional Gaussian broadening.

However, detailed investigations have shown, that this does not change the result and therefore the additional Gaussian found after the first iteration is sufficient.

5.2.4 The spectrometer response function

With the knowledge of the additional Gaussian broadening, the response functions needed for the analysis of the pionic hydrogen transitions can be provided. Using the X-ray tracking routine, with the additional Gaussian broadening as input, the response function is calculated at the position the detector is set during the measurement of the pionic hydrogen spectra. The response function produced in this way is a convolution of three components

$$\text{RF} = \text{XOP} \otimes \text{Tracking} \otimes \text{Gauss}. \quad (5.5)$$

”XOP” represents here the rocking curve for a flat ideal crystal, ”Tracking” accounts for imaging properties of the setup and ”Gauss” describes all imperfections of the used crystals. Taken together, these components comprise the desired response function of the

Crystal	Gas	Gauss [μ rad]	Gauss [meV]
Z20	Ar	32^{+2}_{-3}	131^{+10}_{-11}
	SO ₂ (1)	62 ± 2	127 ± 5
	SO ₂ (2)	70 ± 2	144 ± 5
Z21	Ar	25^{+3}_{-2}	104^{+10}_{-11}
	SO ₂	66 ± 2	137 ± 4
Z13	Ar	33 ± 2	124 ± 7
	Cl	41 ± 2	110 ± 5
	SO ₂	57 ± 3	99 ± 5

Table 5.4: Values for the additional Gaussian broadening. The asymmetric values for the error result from the fact, that for their calculation the package MINOS which is part of the CERN program library MINUIT, was used. The width of the aperture attached to the crystal is 60 mm, as this aperture was also used during the measurements of pionic hydrogen X-ray lines. The results for Z13 are taken from [28].

crystal spectrometer.

6 Analysis and results

6.1 Analysis

The $4p \rightarrow 1s$ X-ray transition in pionic hydrogen was measured in 2002 and 2006 at PSI. For the extraction of Γ_{1s} , different ADC-cuts ($1.0\sigma - 3.0\sigma$) were applied to the raw data (see Table 6.1).

In general, each measured line profile P is a convolution of three functions,

$$P = L \otimes R \otimes \left(\sum_i D_i \right). \quad (6.1)$$

L represents the Lorentz-like hadronic broadening of the ground state in pionic hydrogen. R is the instrumental response function of the used crystal, measured with an electron cyclotron resonance ion trap (ECRIT). The measurement and the following analysis are discussed in detail in chapter 5. D_i represents the Doppler-broadening, originating from the kinetic energy distribution due to a particular Coulomb transition. In chapter 2, the atomic cascade and its influence on the line shape was described.

6.1.1 Free fit to the data

On the basis of the line shape given in (6.1), an analysis routine was developed. It allows the extraction of the strong interaction width from the measured pionic hydrogen lines by taking into account the spectrometer response function as well as the kinetic energy distribution approximated by Doppler boxes. The strong interaction width is determined with a least squares fitting of the data using the program package MINUIT from the CERN program library.

6.1.1.1 Fitting parameters

In the analysis routine the following parameters are used to define the fit-model:

- position of the line,

Data set	ADC-cut [σ]	Rate	Q_p [Cb]	Rate [1/Cb]
2002	3.0	5577 ± 102	1461	3.82
	2.5	5470 ± 97	1461	3.74
	2.0	5277 ± 92	1461	3.61
	1.5	4733 ± 84	1461	3.24
	1.0	3842 ± 74	1461	2.63
2006	3.0	4577 ± 80	884	5.18
	2.5	4458 ± 78	884	5.04
	2.0	4262 ± 74	884	4.82
	1.5	3887 ± 70	884	4.40
	1.0	3205 ± 62	884	3.62

Table 6.1: Overview of the measurements from 2002 and 2006. Q_p is the integrated proton beam current from the accelerator.

- Lorentz-width of the line,
- weight of the Lorentz-peak,
- linear background,
- widths of the Doppler-boxes,
- weights of the respective Doppler-boxes.

The spectrometer response function is read in directly and the analysis routine allows the definition of up to five kinetic energy regions. All functions used in the analysis program are normalised to 1.

For the analysis the following widths for the ADC-cuts to the measured spectra were taken: 3σ , 2.5σ , 2σ , 1.5σ , and 1σ , see section 4.2.2. The wider the cut, the more events of the Lorentz distribution are taken into account. But of course the number of background events also increases accordingly.

These spectra were analysed with the above mentioned analysis routine. During high statistics Monte Carlo investigations ($\approx 10^7$ MC-trials) it turned out, that for the $4p \rightarrow 1s$ transition it is sufficient to use only three kinetic energy regions in order to approximate the kinetic energy distribution of the pionic atoms. Using up to five regions does not improve or change the result, but it increases the computing time, since more parameters have to be fitted.

For the analyses of the 2002 and 2006 data the following kinetic energy regions were used:

ADC-cut [σ]	Γ_{1s} [meV]	BG	I_{Lorentz}	χ^2/dof	χ^2_{red}
3.0	844^{+93}_{-79}	$8.25^{+0.16}_{-0.17}$	5577 ± 102	$\frac{563.47}{566}$	0.99
2.5	841^{+86}_{-75}	$6.83^{+0.15}_{-0.15}$	5470 ± 97	$\frac{594.81}{566}$	1.05
2.0	836^{+85}_{-73}	$5.50^{+0.14}_{-0.14}$	5277 ± 92	$\frac{561.58}{566}$	0.99
1.5	771^{+75}_{-66}	$4.14^{+0.12}_{-0.12}$	4733 ± 84	$\frac{556.85}{566}$	0.98
1.0	763^{+81}_{-70}	$2.82^{+0.10}_{-0.10}$	3842 ± 74	$\frac{579.24}{566}$	1.02

Table 6.2: Free fit to the $4p \rightarrow 1s$ transition in pionic hydrogen, measured in 2002. In order to be well away from the gap between the CCDs, [3:575] ch was used for the fit-region (gap at channel 600, see Figure 6.1(a) and 6.1(c)).

- [0 : 2] eV,
- [28 : 35] eV,
- [49 : 55] eV.

The choice of the energy regions is based on a kinetic energy distribution calculated in the framework of the ESCM (see chapter 2). Unlike the relative weights, the widths of the kinetic energy regions are fixed parameters in the analysis routine.

6.1.1.2 Free fit to the 2002 and 2006 data

Spectrum Figure 6.1 displays two examples of spectra for the $4p \rightarrow 1s$ transition measured in 2002 and 2006. Already after a first look at the spectrum one problem becomes evident for both spectra. At channel 600, where the gap between the two CCD columns is located, a clear change in the background level on the left and on the right side is visible. This circumstance renders one column of the CCD not usable for a correct background determination.

Fit region The fit-region has to be limited to the side of the peak only, which is a considerable drawback, as will become clear when the influence of the fit-region on Γ_{1s} will be discussed in section 6.1.3.2.

Results of the free fit In Tables 6.2 and 6.3 the results of the free fit to the 2002 and 2006 data are summarised. For the error calculation the subroutine MINOS, which is part of the program package MINUIT and is able to calculate asymmetric errors, was

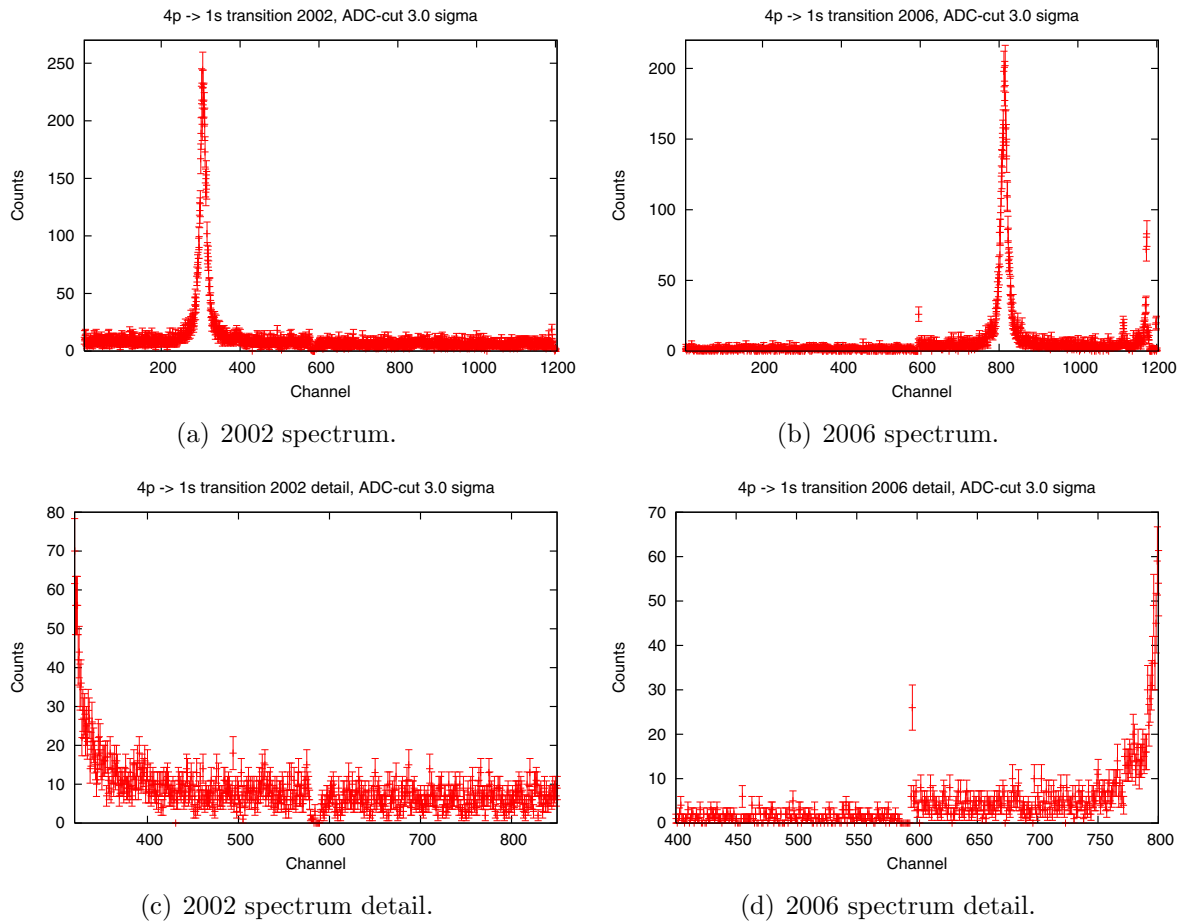


Figure 6.1: $4p \rightarrow 1s$ transition measured in the year 2002 and 2006. The 3.0σ ADC-cut is displayed.

used. Figure 6.2 shows two examples of the fitted spectrum for data measured in 2002 and 2006.

Problems For the ADC-cuts 1.5σ and 1.0σ a considerable decrease in the intensity of the Lorentz-peak compared to the wider cuts is visible (Tables 6.2 and 6.3). Applying these narrow cuts, the channel content of the resulting spectrum is drastically decreased, resulting in a spectrum with very low statistics.

6.1.2 Effect of statistics on the fit-result

As the background rate is low, i. e., the data points of the background and in the tails of the spectrum follow a Poisson distribution, the analysis routine uses maximum likelihood

ADC-cut [σ]	Γ_L [meV]	BG	I_{Lorentz}	χ^2/dof	χ^2_{red}
3.0	815^{+89}_{-76}	$3.60^{+0.12}_{-0.12}$	4577 ± 80	$\frac{536.68}{501}$	1.07
2.5	787^{+80}_{-70}	$3.08^{+0.11}_{-0.11}$	4458 ± 78	$\frac{462.67}{501}$	0.92
2.0	780^{+81}_{-70}	$2.46^{+0.10}_{-0.10}$	4262 ± 74	$\frac{518.63}{501}$	1.03
1.5	761^{+80}_{-69}	$1.87^{+0.09}_{-0.09}$	3887 ± 70	$\frac{547.28}{501}$	1.09
1.0	774^{+95}_{-79}	$1.28^{+0.08}_{-0.08}$	3205 ± 62	$\frac{566.26}{501}$	1.13

Table 6.3: Free fit to the $4p \rightarrow 1s$ transition in pionic hydrogen, measured in 2006. In order to be well away from the gap between the CCDs and also from the distortion at the right end of the spectrum (see Figures 6.1(b) and 6.1(d)), [603:1110] ch was used for the fit-region. See also Figure 4.18(a) right.

estimation (MLE). Let us assume a spectrum with N channels and n_i counts in channel i . Then $\mathbf{n} = (n_1, \dots, n_N)$ is the vector of observed values. The theoretical prediction in channel i is given by a fit function $\mathbf{y} = (y_1, \dots, y_N)$ which in turn is defined by j parameters describing the fit-model (see section 6.1.1.1). In an MLE for a Poisson histogram the function

$$L(\mathbf{y}|\mathbf{n}) = \prod_{i=1}^N \frac{y_i^{n_i}}{n_i!} \exp(-y_i) \quad (6.2)$$

is maximised. If the likelihood ratio

$$\lambda = \frac{L(\mathbf{y}|\mathbf{n})}{L(\mathbf{m}|\mathbf{n})} \quad (6.3)$$

is used (which asymptotically obeys a χ^2 distribution), with \mathbf{m} being the true (though unknown) value of \mathbf{n} if there were no errors in the measurement and, forming $-2 \ln \lambda$, then for Poisson distributed data points, the expression

$$\chi^2_\lambda = 2 \sum_i^N \left[y_i - n_i + n_i \ln \left(\frac{n_i}{y_i} \right) \right] \quad (6.4)$$

is minimised. In the case of maximum likelihood (as also for the least squares method) the estimators are often biased, even if they asymptotically converge to the true value. Biased means that the mean value of estimates obtained from repeated independent experiments is not equal to the true value. This bias can be corrected for by means of Monte Carlo studies. For detailed discussion on this issue see e.g. [83–85].

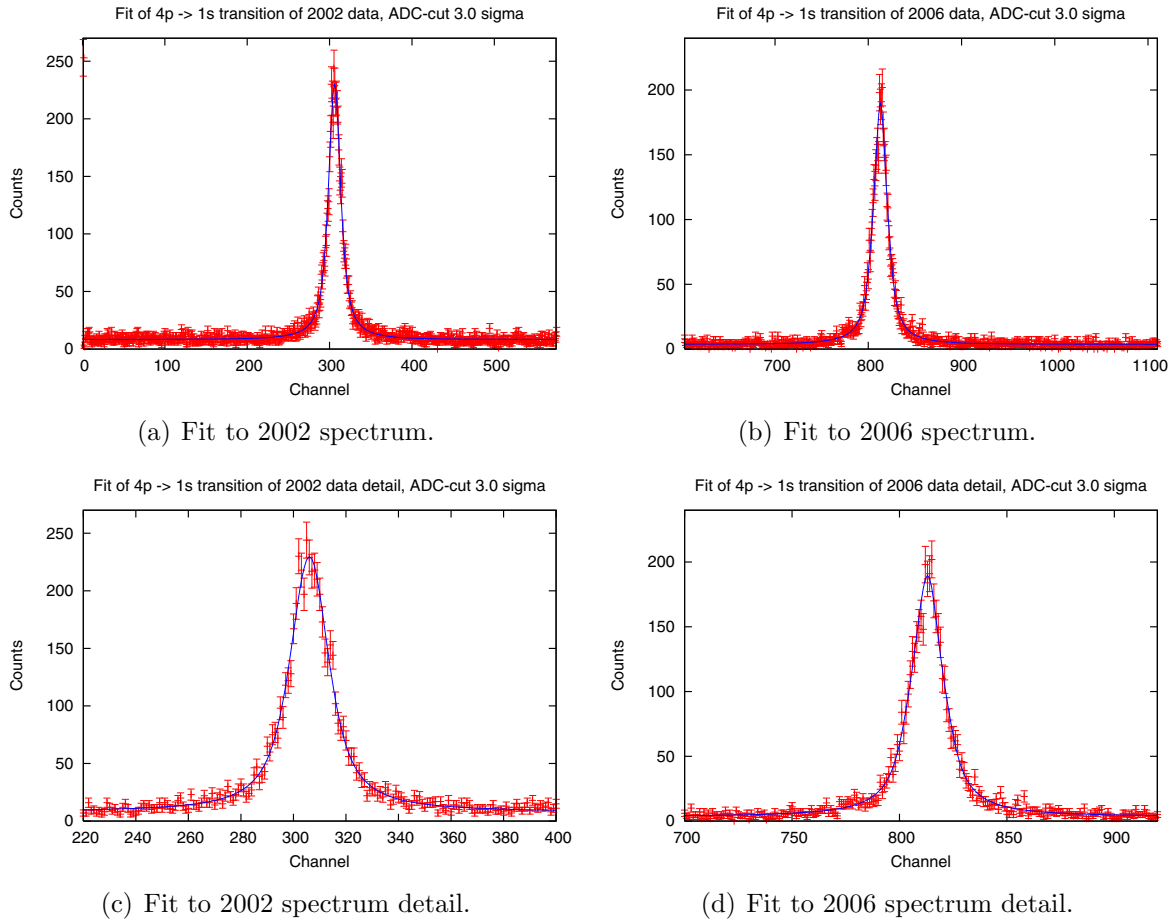


Figure 6.2: The 2002 and 2006 data with fit-function is displayed for 3.0σ ADC-cuts.

6.1.3 Monte Carlo studies

The task in this section is to gain a qualitative understanding what influence boundary conditions such as peak to background, height of background and fit-region have on the results of the fit. Therefore the following investigations are undertaken:

- Correlation of background and Γ_{1s} .
- Correlation of fit-region and Γ_{1s} .
- Correlation of fit-region and background.

All investigations are performed according to the spectra measured in 2002. The choice of the 2002 data is due to the worse peak to background compared to the 2006 data. Therefore a more pronounced effect is expected and the results are more instructive.

BG (fixed)	Γ_{1s} [meV]
8.075	898^{+84}_{-74}
8.110	883^{+86}_{-69}
8.145	874^{+82}_{-69}
8.180	865^{+78}_{-70}
8.215	856^{+75}_{-70}
8.250	844^{+75}_{-67}
8.285	834^{+74}_{-66}
8.320	825^{+72}_{-65}
8.355	815^{+71}_{-64}
8.390	806^{+70}_{-63}
8.425	798^{+69}_{-62}

Table 6.4: Fit-results with fixed background. The central value is printed in bold.

6.1.3.1 Correlation of background and Γ_{1s}

To check the influence of the background level on the result for Γ_{1s} , fits to the data are conducted by fixing the background at the central value found in the free fit (e. g. for the 3.0σ cut: $\text{BG} = 8.25^{+0.16}_{-0.17}$) and values corresponding to plus and minus the error and intermediate values in appropriate steps. The results are given in Table 6.4 and are plotted in Figure 6.3. A clear decrease of Γ_{1s} is seen with increasing background: a change of the background value in the order of \pm the error, gives a $\Delta\Gamma_{1s} \approx 100$ meV. This illustrates the strong dependence of Γ_{1s} on the background and reveals the high importance of a good measure of the background in order to get an accurate result for the strong interaction width in pionic hydrogen.

To understand the strong correlation between background and Γ_{1s} , the shape of a Lorentz curve has to be recalled:

$$L(x) = \frac{\Gamma}{2\pi} \frac{1}{\left(\frac{\Gamma}{2}\right)^2 + x^2}. \quad (6.5)$$

Unlike in the case of a Gaussian distribution, where the decrease in the tails is exponential, in the case of a Lorentz curve it is much less pronounced and its influence extends far off the peak position. Therefore, also far away from the peak position still some Lorentz fraction might be found. This fraction could in turn be wrongly attributed to the background instead of the Lorentz curve. This clearly points out that a wide fit-region is favoured in order to get a good fit-result for the Lorentz width. In the next section the influence of the fit-region will be investigated in detail.

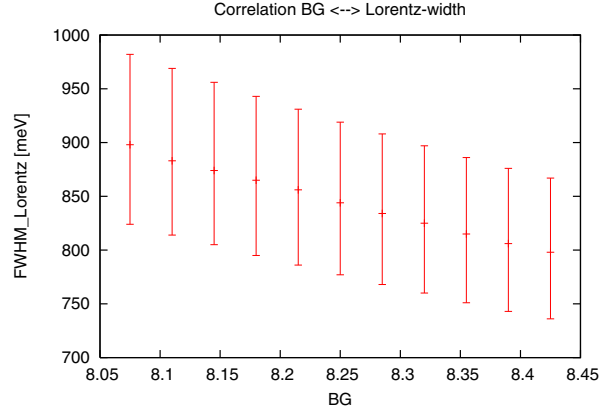


Figure 6.3: Results for Γ_{1s} from a fit to the 2002 data using a fixed background value as input.

6.1.3.2 Correlation of fit-region and Γ_{1s}

Spectra For the study of the influence of the fit-region on Γ_{1s} , spectra are simulated according to the statistics and the background condition of the 2002 data.

Simulation parameters In the simulation the following parameters are used as input: $\Gamma = 820$ meV, background $BG = 8.3$.

Effect of fit-region In the input of the fit-routine only the fit-range is varied in steps of 68 ch, which corresponds to ~ 5 eV. For each data point, i. e., one fit-region, 400 spectra with 400 different Monte Carlo seeds (starting value for the Monte Carlo generator) are simulated and fitted with all parameters describing the model kept free in the fit. From these 400 (fitted) values for Γ and background, the mean is calculated and then plotted versus the fit-region, see Figure 6.4.

Result The plots in Figure 6.4 clearly reveal a bias of the fit routine. Even for the maximally available fit-region (573 channels), the input width and background are not reproduced. In the particular case considered here (the $4p \rightarrow 1s$ transition measured in 2002) the bias manifests itself such, that the fitted value is too high. The bias has to be determined for each data set individually.

6.1.4 Analysis strategy

From the general considerations in the preceding sections, the strategy for the further analysis is obvious. The overall goal is to quantify the bias of the fit routine. Once it is

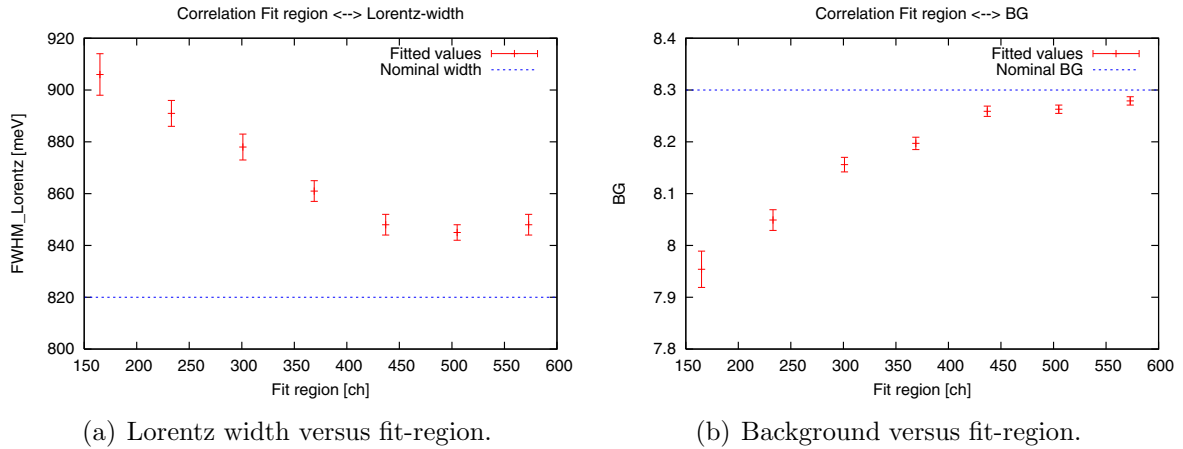


Figure 6.4: Correlation between Lorentz width and fit-region (Figure 6.4(a)) and between background and fit-region (Figure 6.4(b)). The values for the Lorentz width and background are the mean values resulting from 400 Monte Carlo simulations and subsequent fits for each data point in the plots.

determined, the results obtained from the free fit to the measured data (Tables 6.2 and 6.2) must be corrected for this bias.

Given the strong correlation of background and Lorentz width (see Figure 6.3), the basic idea to determine the bias is, to perform a high number of simulations with different seeds such, that the mean value of the fitted background is well in agreement with the one obtained from the free fit to the data (for each ADC-cut). In more detail:

1. Free fit to measured spectrum, yielding $BG_{\text{data}}^{\text{fit}}$ and $\Gamma_{\text{data}}^{\text{fit}}$.
2. Simulate N spectra (N different Monte Carlo seeds), with BG_{simul} and Γ_{simul} as input, where in general $BG_{\text{simul}} \neq BG_{\text{data}}^{\text{fit}}$. Γ_{simul} should be close to the value found in the free fit (Tables 6.2 and 6.3). In the analysis discussed here, the investigation was performed typically for three different values of Γ_{simul} (Tables 6.5 and 6.6).
3. Fit to simulated spectra. From each of the N fits, a background $BG_{\text{simul}}^{\text{fit}}$ and a width $\Gamma_{\text{simul}}^{\text{fit}}$ are obtained.

$$\text{Adjust } BG_{\text{simul}} \text{ until } BG_{\text{simul}}^{\text{mean}} = \frac{\sum_i^N (BG_{\text{simul}}^{\text{fit}})_i}{N} \approx BG_{\text{data}}^{\text{fit}}.$$

4. For the adjusted set of spectra calculate the mean Lorentz width $\Gamma_{\text{simul}}^{\text{mean}} = \frac{\sum_i^N (\Gamma_{\text{simul}}^{\text{fit}})_i}{N}$. From $\Gamma_{\text{simul}}^{\text{mean}}$, the bias $\Delta\Gamma = \Gamma_{\text{simul}}^{\text{mean}} - \Gamma_{\text{simul}}$ is calculated. $\Delta\Gamma$ represents the bias of the fit-routine for this specific case. N is chosen large enough that the statistical error of the simulation is in the order of 3 meV for Γ^{mean} only.

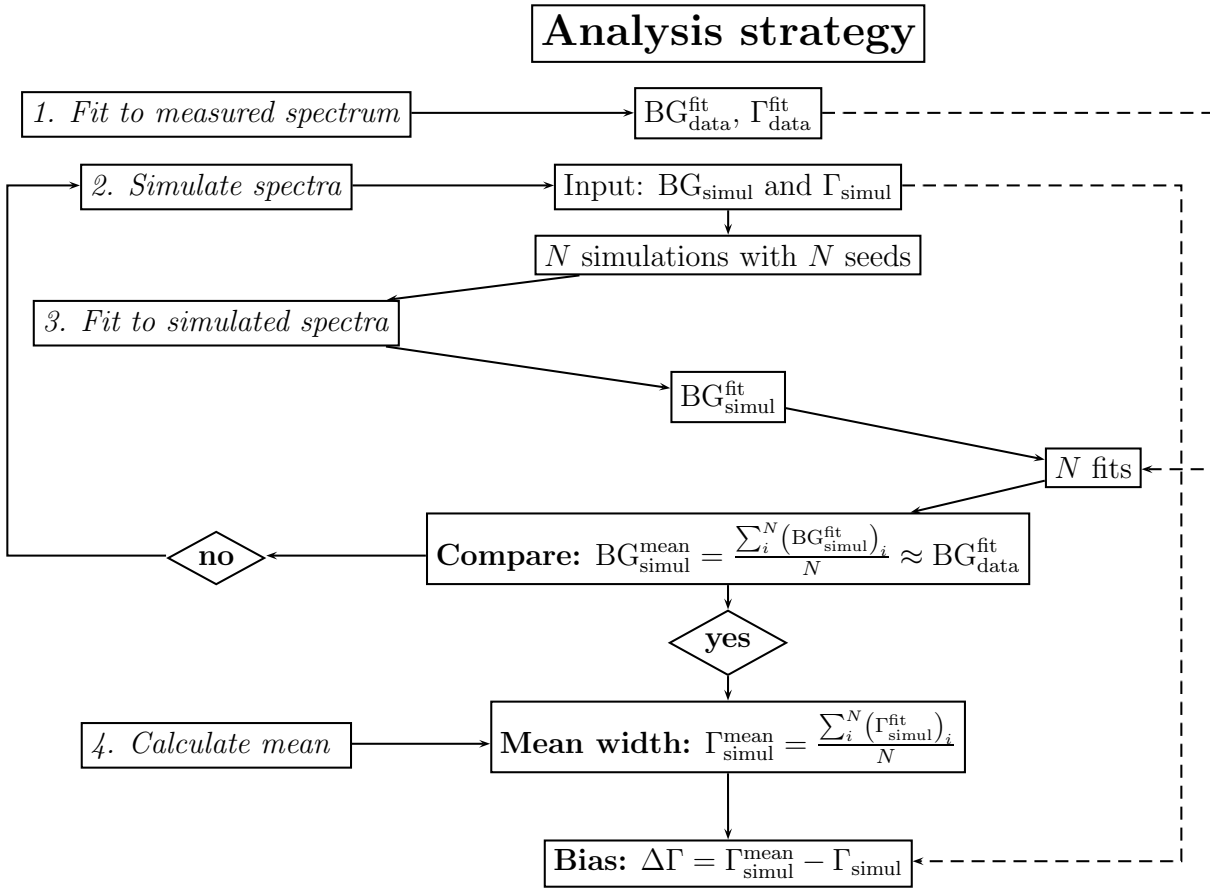


Figure 6.5: Flowchart of the analysis strategy. For details see text.

This procedure has to be repeated for each ADC-cut. Figure 6.5 illustrates the analysis strategy by means of a flow chart.

6.1.4.1 Statistics of simulated spectra and the definition of the fit-region

A necessary requirement for the above procedure to be successful is, that the conditions of the simulated spectra are the same as for the measured spectra. That is, the number of counts under the Lorentz curve must be the same as for the data. Furthermore, as was described in section 6.1.3.2, another very important requirement is the equality of the relative widths of the fit-regions. And lastly, the background level has to be chosen appropriately.

Statistics of simulated spectra The number of counts under the Lorentz curve for the 3.0σ ADC-cut for e.g., the 2002 data is 5577 ± 102 . This number represents only

the counts attributed to the Lorentz curve and is defined as $I_{\text{Lorentz}} = I_{\text{Peak}} - I_{\text{BG}}$. Thus, spectra have to be simulated with the number of counts according to I_{Lorentz} as determined by the free fit to the data.

Fit-region In the simulation routine the peak is positioned at channel 600, whereas it is at a different position during the measurement (e.g. at channel ~ 307 for the 2002 data). As already mentioned (section 6.1.3.2), the resulting value for Γ is highly sensitive on the fit-region. It is of high importance to have the same conditions for the free fit to the measured data and for the numerous fits to the simulated data. The fit-region used in the free fit to the 2002 data was [3:575] which corresponds to 573 channels, 304 channels on the left and 268 channels on the right side of the peak. Consequently, the fit-region used in the fits to the simulated spectra has to be chosen appropriately. I.e., with the peak being located at channel 600, the fit-region for the fit to the simulated data in the determination of the bias for the 2002 data is set to [296:868].

6.2 Results

6.2.1 Bias for $4p \rightarrow 1s$ 2002

In Table 6.2 the results of the free fit to the 2002 data are collected. As can be seen, the resulting Lorentz width for the ADC-cuts between 3.0σ and 1.0σ is of the order of ≈ 810 meV. Therefore, in order to determine the bias for the fit-routine in this region, the simulations are done for widths of 720, 760, 820 and 860 meV. For the number of simulations N , 800 was chosen, since the error of the mean value for Γ after 800 fits is of the order of 2-3 meV and negligible compared to the statistical error of the measurement. Simulations and subsequent fits following the prescription described in section 6.1.4 were carried out for each ADC-cut with the fit-region set to [296:868]. The results are summarised in Table 6.5.

6.2.2 Bias for $4p \rightarrow 1s$ 2006

For the analysis of the $4p \rightarrow 1s$ transition measured in 2006 only a few modifications have to be made. In comparison to the results from 2002, a clear decrease in the background level is seen. This is due to the fact, that during this beam time much effort was put in background reduction by further improving the concrete shielding.

The fit-region used in the free fit to the 2006 data was [603:1110], which corresponds to 501 channels, with 209 channels on the left and 298 channels on the right side of the peak.

ADC-cut [σ]	Γ_{simul} [meV]	$\Gamma_{\text{L}}^{\text{mean}}$ [meV]	BG _{simul}	BG _{mean}	$\Delta\Gamma$ [meV]
3.0	760	792 ± 2	8.280	8.240 ± 0.005	32 ± 2
	820	846 ± 2	8.300	8.274 ± 0.006	26 ± 2
	860	889 ± 3	8.270	8.246 ± 0.006	29 ± 3
2.5	760	783 ± 2	6.900	6.860 ± 0.005	23 ± 2
	820	845 ± 2	6.900	6.862 ± 0.005	25 ± 2
	860	889 ± 3	6.850	6.813 ± 0.005	29 ± 3
2.0	760	780 ± 2	5.495	5.467 ± 0.004	20 ± 2
	820	842 ± 2	5.500	5.476 ± 0.004	22 ± 2
	860	881 ± 2	5.500	5.479 ± 0.004	21 ± 2
1.5	720	737 ± 2	4.160	4.143 ± 0.004	17 ± 2
	760	786 ± 2	4.160	4.130 ± 0.004	26 ± 2
	820	848 ± 2	4.150	4.123 ± 0.004	28 ± 2
1.0	720	749 ± 2	2.850	2.827 ± 0.003	29 ± 2
	760	789 ± 2	2.845	2.818 ± 0.003	29 ± 2
	820	850 ± 2	2.838	2.815 ± 0.003	30 ± 2

Table 6.5: Results after 800 simulations and 800 convergent fits for the $4p \rightarrow 1s$ transition measured in 2002.

Hence, [391:898] was chosen for the fit-region in the fit to the simulated data.

In Table 6.3 the results of the free fit are summarised. The resulting Lorentz width for the ADC-cuts between 3.0σ and 1.0σ is of the order of ≈ 780 meV, thus, in the case of the 2006 data, the simulations are performed for widths of 720, 760, 820 and 880 meV. The results of the simulations are found in Table 6.6.

ADC-cut [σ]	Γ_{simul} [meV]	Γ_L^{mean} [meV]	BG _{simul}	BG _{mean}	$\Delta\Gamma$ [meV]
3.0	760	797 ± 2	3.630	3.588 ± 0.004	37 ± 2
	820	856 ± 2	3.635	3.593 ± 0.004	36 ± 2
	880	926 ± 2	3.641	3.594 ± 0.004	46 ± 2
2.5	720	756 ± 2	3.115	3.080 ± 0.004	36 ± 2
	760	794 ± 2	3.120	3.087 ± 0.004	34 ± 2
	820	860 ± 2	3.110	3.071 ± 0.004	40 ± 2
2.0	720	756 ± 2	2.505	2.466 ± 0.003	36 ± 2
	760	791 ± 2	2.505	2.471 ± 0.003	31 ± 2
	820	860 ± 2	2.510	2.469 ± 0.004	40 ± 2
1.5	720	754 ± 2	1.9	1.866 ± 0.003	34 ± 2
	760	796 ± 2	1.9	1.869 ± 0.003	36 ± 2
	820	859 ± 2	1.895	1.862 ± 0.003	39 ± 2
1.0	720	752 ± 2	1.305	1.282 ± 0.002	32 ± 2
	760	799 ± 2	1.305	1.282 ± 0.002	39 ± 2
	820	859 ± 2	1.310	1.282 ± 0.003	39 ± 2

Table 6.6: Results after 800 simulations and 800 convergent fits for the $4p \rightarrow 1s$ transition measured in 2006. The values Γ_{simul} for the 3.0σ cut are different from the others, because the value from the free fit is also slightly higher (Table 6.3).

ADC-cut [σ]	$\Gamma_{\text{data}}^{\text{fit}}$ [meV]	$\Delta\Gamma^{\text{mean}}$ [meV]	$\Gamma_{\text{data}}^{\text{corr}}$ [meV]
3.0	844_{-79}^{+93}	29 ± 4	815_{-79}^{+93}
2.5	841_{-75}^{+86}	26 ± 4	815_{-75}^{+86}
2.0	836_{-73}^{+85}	21 ± 3	815_{-73}^{+85}
1.5	771_{-66}^{+75}	24 ± 3	747_{-66}^{+75}
1.0	763_{-70}^{+81}	29 ± 3	734_{-70}^{+81}

Table 6.7: Results for Γ_{1s} for data measured in 2002. $\Gamma_{\text{data}}^{\text{fit}}$ denotes the result obtained with a free fit to the measured data, $\Delta\Gamma^{\text{mean}}$ is the mean value of the bias for the appropriate ADC-cut and $\Gamma_{\text{data}}^{\text{corr}}$ represents the corrected value of the strong interaction width.

ADC-cut [σ]	$\Gamma_{\text{data}}^{\text{fit}}$ [meV]	$\Delta\Gamma^{\text{mean}}$ [meV]	$\Gamma_{\text{data}}^{\text{corr}}$ [meV]
3.0	815_{-76}^{+89}	40 ± 3	775_{-76}^{+89}
2.5	787_{-70}^{+80}	37 ± 3	749_{-70}^{+80}
2.0	780_{-70}^{+81}	36 ± 3	744_{-70}^{+81}
1.5	761_{-69}^{+80}	36 ± 3	722_{-69}^{+80}
1.0	774_{-79}^{+95}	37 ± 3	737_{-79}^{+95}

Table 6.8: Results for Γ_{1s} for data measured in 2006. For explanation see Table 6.7.

6.2.3 Final value for Γ_{1s}

With the bias determined for the different simulated spectra and ADC-cuts (Tables 6.5 and 6.6), finally the results from the free fit to the data can be corrected appropriately. For this, the mean value of the bias for each ADC-cut has to be calculated and subtracted from the adequate value of Γ_{1s} obtained from the free fit to the data. The results for the 2002 and 2006 data derived this way are listed in Tables 6.7 and 6.8, respectively. For each measurement period the mean value of all ADC-cuts is calculated (Table 6.9) and finally, from these two mean values, the weighted mean (see (5.3) and (5.4)) is calculated:

$$\Gamma_{1s} = 765 \pm 56 \text{ meV}. \quad (6.6)$$

(6.6) is considered to be the final result of this work.

From the final value for Γ_{1s} given in (6.6), the following quantities are derived:

Year	Γ_{mean} [meV]	$\Gamma_{\text{final}}^{\text{symm.err.}}$ [meV]
2002	785_{-73}^{+84}	$785 \pm \frac{84+73}{2} = 785 \pm 79$
2006	745_{-73}^{+85}	$745 \pm \frac{85+73}{2} = 745 \pm 79$

Table 6.9: Calculation of final value for the strong interaction ground state width in pionic hydrogen. Γ_{mean} represents the mean value from all ADC-cuts for each year. $\Gamma_{\text{final}}^{\text{symm.err.}}$ is the value with symmetric error as needed for the calculation of the weighted mean.

πN scattering lengths From the final result for the hadronic broadening Γ_{1s} , the isovector scattering lengths a^- can be calculated from the Deser-type formula (3.62). Using the correction factor $\delta_{\Gamma} = (0.6 \pm 0.2) \cdot 10^{-2}$ (section 3.3.1), the isovector scattering length becomes

$$a^- = (83.35 \pm 3.06) \cdot 10^{-3} m_{\pi}^{-1}.$$

Using

$$a^+ + a^- = (93.20 \pm 2.9) \cdot 10^{-3} m_{\pi}^{-1}$$

from [8], the isoscalar scattering length reads

$$a^+ = (9.85 \pm 4.22) \cdot 10^{-3} m_{\pi}^{-1}.$$

πN coupling constant The πN coupling constant is calculated from the GMO sum rule by inserting the value for the isovector scattering length into (3.69) and with the value for J from (3.71) it reads

$$f_{\pi N}^2 = 0.0745 \pm 0.0020.$$

Goldberger-Treiman discrepancy Using the value for $f_{\pi N}$, the axial coupling constant $g_A = 1.2695 \pm 0.0029$ [38], the pion decay constant $F_{\pi} = 92.42 \pm 0.32$ MeV [38] and $g_{\pi NN} = 13.0134 \pm 0.1754$ (see also (3.31)) the value for the Goldberger-Treiman discrepancy (3.32) is

$$\Delta_{\pi N} = 0.961 \pm 1.397\%.$$

7 Summary and Outlook

7.1 Summary

This work describes the first step of an experimental program undertaken to increase significantly the accuracy for the strong interaction width of the ground state in pionic hydrogen. This goal was approached by several improvements both in the experimental realisation and the analysis strategy.

X-ray transition: The $4p \rightarrow 1s$ transition in pionic hydrogen was measured the first time and it was used to develop the analysis method in this work, since it is least influenced by Doppler broadening.

Concrete shielding: A dedicated concrete shielding between X-ray source and crystal spectrometer results in a substantial reduction of the background.

Doppler-broadening: The kinetic energy distribution of the pionic atoms leading to a Doppler-broadening of the X-ray transitions was approximated by a model using box-like distributions. This approach was verified by the measurement of the $3p \rightarrow 1s$ X-ray transition in muonic hydrogen, where the strong-interaction broadening is absent and hence the X-ray line-shape is very sensitive to Doppler-broadening.

Response function: The measurement of the instrumental response function with an electron cyclotron resonance ion trap allowed a precise and model-independent quantification of broadening effects originating from the crystal spectrometer setup.

X-ray tracking: A Monte Carlo based X-ray tracking routine was developed taking into account crystal properties and the geometric effects of the setup. This allows to study in detail systematic effects of the experimental conditions on the pionic hydrogen spectra.

Monte Carlo studies: Extensive Monte Carlo studies have been performed to determine the bias of the analysis routine caused by the low statistics of the π^-p spectra. This is of outstanding importance because of the strong correlation between Γ_{1s} and background in the analysis.

Accuracy: By analysing the $4p \rightarrow 1s$ transition only, the accuracy of the result for Γ_{1s} compared to the value given in [60] could be improved already. Here, the systematic errors owing to analysis and background have been precisely determined.

The final result for Γ_{1s} obtained in this work reads

$$\Gamma_{1s} = 765 \pm 56 \text{ meV.}$$

7.2 Outlook

The new analysis method developed in this work and first applied to the $4p \rightarrow 1s$ transition in pionic hydrogen will be the basis for the evaluation of the X-ray spectra from the $3p \rightarrow 1s$ and $2p \rightarrow 1s$ transitions in hydrogen and the deuterium $3p \rightarrow 1s$ measurement. In the case of the $4p \rightarrow 1s$ transition, because of the small dispersion, a sufficiently large region for background determination is available left and right of the line. For the $3p \rightarrow 1s$ and the $2p \rightarrow 1s$ transitions, the situation is complicated because of the increasing influence of Coulomb deexcitation causing a further broadening of the spectral line. In addition, the increasing dispersion leads to a decreasing region available for background determination.

From the accumulated statistics for all transitions, finally an accuracy of about 2-3% for the strong interaction ground state width in pionic hydrogen should be attainable. This corresponds to 1-1.5% for the isovector scattering length a^- . From the new result for the shift in pionic deuterium, an additional constraint for the scattering lengths is obtained. The data are currently being analysed.

Acknowledgement

The author would like to acknowledge the Laboratory for Advanced Computing of the University of Coimbra for providing computer time on the *Milipeia* supercomputer.

Appendix A

File lists

In the following pages the lists of data files for the 2002 and 2006 beamtimes are collected. An explanation of the table headers is given beforehand:

date: is the date the measurement was started.

crystal aperture: gives the dimension of the aperture attached to the Bragg crystal.

target / source: is the target gas or the source in the case of fluorescence X-rays.

***p*:** is the target pressure given in [mbar].

***T*:** is the target temperature in [K].

Q_p : is the integrated proton beam current in [C].

LEX #/ page: is the page in the beamtime logbook.

file name: is the name of the recorded data file.

comment: gives additional information, e. g., on spectrometer settings.

PIONIC HYDROGEN

FILE LIST PSI 2002 Run book: LEX #8/9

date	crystal aperture	target/source	p /mbar	T /K	Q_p /C	LEX #/page	file name	Analysis #/page	comment
5.6.	Z13 60	Ga	---	294	---	9/26	ga_0470-0475		target scan with arm
6.6.	Z13 60	Ga	---	294	---	9/26	ga_0476-0481		target scan with crystal
6.6.	Z13 60	Ga	---	294	---	9/28	ga_0482-0484		cry 39°46' 12.1" ,arm 43°13' , 5+60+60 frames, LinTab=69.79
6.6.	Z13 60	H ₂	1198	30.0	18.10	9/29	piH_0485-0488		cry 39°46' 12.1" ,arm 43°13' , LinTab=69.79
6.6.	Z13 60	H ₂	1198	30.0	9.39	9/29	piH_0489-0490		cry 39°31' , target scan with crystal
6.6.	Z13 60	H ₂	1216	30.0	697.75	9/29	piH_0491-0600		cry 39°46' 12.1" ,arm 43°13' , LinTab=69.79
12.6.	Z13 60	Ga	---	294	---	9/35	ga_0601-0602		cry 39°46' 12.1" ,arm 43°13' , 60+60 fr., LinTab=69.80
12.6.	Z13 60	Ga	---	294	---	9/35	ga_0603-0604		cry 39°46' 12.1" ,arm 43°13' , 60+60 fr., LinTab=69.80
13.6.	Z13 60	H ₂	1232	30.0	351.45	9/39	piH_0605-0659		cry 39°46' 12.1" ,arm 43°13' , LinTab=69.79
15.6.	Z13 60	Ga	---	294	---	9/41	ga_0660-0661		cry 39°46' 12.1" ,arm 43°13' , 60+60 fr., LinTab=69.80
16.6.	Z13 60	H ₂	1232	30.0	337.49	9/43	piH_0662-0715		cry 39°46' 12.1" ,arm 43°13' , LinTab=69.79
18.6.	Z13 60	Ga	---	294	---	9/45	ga_0716-0717		V2 operated to change safety air
18.6.	Z13 60	H ₂	1232	30.0	73.37	9/47	piH_0718-0729		cry 39°46' 12.1" ,arm 43°13' , LinTab=69.79
19.6.	Z13 60	Ga	---	294	---	9/47	ga_0730		cry 39°46' 12.1" ,arm 43°13' , 90 fr., LinTab=69.80
21.6.	Z13 60	Ge	---	294	---	9/50	ge_0731-0733		cry ,arm 90 fr., LinTab=88.7

date	crystal aperture	target/source	Pressure /mbar	T /K	Q_p /C	LEX #/page	file name	$\Delta E/\Delta x$ $\Delta x=93\text{-}1025$	comment
12.7.	Z13 ϕ 60	Ga K α	---	---	---		GaKa_0001-0004		Tilt adjust -0.07 -> +0.18 LinTab 56.76
13.7.	Z13 ϕ 60	Ga K α	---	---	---		GaKa_005-0017		Target scan 30kV 30 mA
12.7.	Z13 ϕ 60	Ga K α	---	---	---		GaKa_0018-0027		17:32 Axial position of target 30 kV 30 mA
12.7.	Z13 ϕ 60	Ga K α	---	---	---		GaKa_0028		18:53 25kV 18mA
12.7.	Z13 ϕ 60	Ga K α	---	---	---		GaKa_0029-0033		19:01
13.7.	Z13 ϕ 60	Ga K α	---	---	---		GaKa_0034		11:30
13.7.	Z13 ϕ 60	Ga K α	---	---	---		GaKa_0035-0048		12:00 Target scan
13.7.	Z13 ϕ 60	Ga K α	---	---	---		GaKa_0049-0062		Axial scan
13.7.	Z13 ϕ 60	Ga K α	---	---	---		GaKa_0063-0065		30kV 30mA target -12 mm CRV 42 31 05
		piH(4-1) BG							
13.7.	Z13 ϕ 60	H ₂	0.93	26?	86.35		piH_bg_0066-0083		18:30 CRV 40 20 00 ARM 42 31 05 LinTab 56:75?
		piH(4-1)							
10.8	Z13 ϕ 60	H ₂	1.04	26.28	2.50	14/1	piH4-1_0578		CRY405020 ARM 414000 LinTab79 84 10 bar start
10.8	Z13 ϕ 60	H ₂	1.04	26.31	3.97	14/1	piH4-1_0579 corrupt		15:30 file too long for csdcluster new noise set.
10.8	Z13 ϕ 60	H ₂	1.06	26.54	92.31	14/3	piH4-1_0580-0598		17:02 PIX3 crash after 0:598
11.8	Z13 ϕ 60	H ₂	1.07	26.3	301.53	14/5	piH4-1_0599-0662		20:19 between 662 and 673 start MEGAPIE
14.8	Z13 ϕ 60	H ₂	1.06	26.4	51.37	14/5	piH4-1_0663-0673		21:06 without MEGAPIE
15.8	Z13 ϕ 60	H ₂	1.07	26.1	57.27	14/17	piH4-1_0674-0687		15:53
16.8	Z13 ϕ 60	H ₂	1.01	26.6	83.31	14/19	piH4-1_0688-0705		14:04
17.8	Z13 ϕ 60	H ₂	1.04	26.4	298.29	14/22	piH4-1_0706-0769		14:08 (580-769: 878.08 Cb)

Bibliography

- [1] S. Deser, M. L. Goldberger, K. Baumann, and Walter E. Thirring. Energy level displacements in π -mesonic atoms. *Phys. Rev.*, 96:774–776, 1954.
- [2] B. Adeva et al. CERN experiment PS212 (DIRAC). Proposal CERN/SPSLC 95-1, CERN, 1995.
- [3] G. Beer et al. Measurement of the Kaonic Hydrogen X-Ray Spectrum. *Phys. Rev. Lett.*, 94:212302, 2005.
- [4] Web page: <http://www.lnf.infn.it/esperimenti/siddharta/>.
- [5] J. Bailey et al. Measurements of pionic X-rays from hydrogen. *Phys. Lett.*, B32:369–372, 1970.
- [6] H. C. Schroeder et al. Determination of the π N scattering lengths from pionic hydrogen. *Phys. Lett.*, B469:25–29, 1999.
- [7] D. Gotta et al. Measurement of the strong interaction width and shift of the ground state of pionic hydrogen. Proposal R-98-01, PSI, 1998.
- [8] M. Hennebach. *Precision Measurement of Ground State Transitions in Pionic Hydrogen*. PhD thesis, Universität zu Köln, 2003.
- [9] S. Tomonaga and G. Araki. *Phys. Rev.*, 58:90, 1940.
- [10] M. Conversi, E. Pancini, and O. Piccioni. *Phys. Rev.*, 68:232, 1945.
- [11] M. Conversi, E. Pancini, and O. Piccioni. *Phys. Rev.*, 71:209, 1946.
- [12] E. Fermi and E. Teller. *Phys. Rev.*, 72:399, 1947.
- [13] W. F. Fry. *Phys. Rev.*, 83:594, 1951.
- [14] T. S. Jensen and V. E. Markushin. *Lecture Notes in Physics*, 627:37–57, 2003.
- [15] M. Leon and H. A. Bethe. *Phys. Rev.*, 127:636, 1962.

- [16] E. Borie and M. Leon. X-ray yields in protonium and mesic hydrogen. *Phys. Rev. A*, 21(5):1460–1468, 1980.
- [17] T. S. Jensen and V. E. Markushin. *Eur. Phys. J. D*, 21:271, 2002.
- [18] T. S. Jensen and V. E. Markushin. *Eur. Phys. J. D*, 21:261, 2002.
- [19] T. S. Jensen. *Eur. Phys. J. D*, 31:11, 2004.
- [20] J. S. Cohen. *Phys. Rev. A*, 59:1160, 1999.
- [21] T. S. Jensen. In A. Hirtl, J. Marton, E. Widmann, and J. Zmeskal, editors, *International Conference on Exotic Atoms and Related Topics*, page 209. Austrian Academy of Sciences, 2005.
- [22] Proceedings of the International Symposium on Exotic Atoms, Molecules, and Muon Catalyzed Fusion (EXAT98). *Hyperfine Interact.* 118/119, 1999.
- [23] S. Jonsell, J. Wallenius, and P. Froelich. Influence of $pp\pi$ ions on pion absorption in h_2 . *Phys. Rev. A*, 59(5):3440–3453, May 1999.
- [24] J. F. Crawford et al. *Phys. Rev. D*, 43:46, 1991.
- [25] E. C. Aschenauer et al. *Phys. Rev. A*, 51:1965, 1995.
- [26] A. Badertscher et al. *Europhys. Lett.*, 54:313, 2001.
- [27] R. Frosch. Kinetic energy of π^-p atoms in liquid hydrogen. Technical Report TM-37-21, Paul Scherrer Institut, 1985.
- [28] D. Covita. PhD thesis, University of Coimbra, 2008.
- [29] L. M. Simons. Private communication.
- [30] J. Gasser and H. Leutwyler. *Ann. of Phys.*, 158:142, 1984.
- [31] J. Gasser and H. Leutwyler. *Nucl. Phys. B*, 250:465, 1985.
- [32] Torleif Ericson and Wolfram Weise. *Pions and Nuclei*. Clarendon Press, 1988.
- [33] M. L. Goldberger and S. B. Treiman. Decay of the π -meson. *Phys. Rev.*, 110:1178–1184, 1958.
- [34] S. Weinberg. *Physica*, 96A:327, 1979.

-
- [35] S. Scherer and M. R. Schindler. A chiral perturbation theory primer. 2005.
- [36] Anthony W. Thomas and Wolfram Weise. *The Structure of the Nucleon*. WILEY-VCH Verlag, Berlin, 2001.
- [37] Höhler, G. *Pion-nucleon Scattering*, volume I/9b2 of *Landolt-Börnstein*. Springer, 1983.
- [38] W. M. Yao et al. Review of particle physics. *J. Phys.*, G33:1–1232, 2006.
- [39] John R. Taylor. *Scattering Theory: The Quantum Theory of Nonrelativistic Collisions*. Dover Publications, 2006.
- [40] Leonard S. Rodberg and Roy M. Thaler. *Introduction to the Quantum Theory of Scattering*. Academic Press, 1967.
- [41] Brian H. Brandson and R. Gordon Moorhouse. *The Pion-Nucleon System*. Princeton Univ. Press, 1973.
- [42] Steven Weinberg. Pion scattering lengths. *Phys. Rev. Lett.*, 17(11):616–621, Sep 1966.
- [43] G. Rasche and W. S. Woolcock. Connection between low-energy scattering parameters and energy shifts for pionic hydrogen. *Nucl. Phys.*, A381:405–418, 1982.
- [44] J. Spuller et al. A remeasurement of the Panofsky ration. *Phys. Lett.*, B67:479–482, 1977.
- [45] D. Sigg, A. Badertscher, P. F. A. Goudsmit, H. J. Leisi, and G. C. Oades. Electromagnetic corrections to the s wave scattering lengths ion pionic hydrogen. *Nucl. Phys.*, A609:310–325, 1996.
- [46] J. Gasser, M. A. Ivanov, E. Lipartia, M. Mojzis, and A. Rusetsky. Ground-state energy of pionic hydrogen to one loop. *Eur. Phys. J.*, C26:13–34, 2002.
- [47] Valery E. Lyubovitskij and A. Rusetsky. π^-p atom in chpt: Strong energy-level shift. *Phys. Lett. B*, B494:9–18, 2000.
- [48] P. Zemp. *Pionic Hydrogen in QCD+QED: Decay width at NNLO*. PhD thesis, University of Bern, 2004.
- [49] P. Zemp. In L. Afanasyev, G. Colangelo, and J. Schacher, editors, *HadAtom05 – Workshop on Hadronic Atoms*, page 16, 2005.

- [50] A. N. Ivanov, M. Faber, A. Hirtl, J. Marton, and N. I. Troitskaya. On pionic hydrogen: Quantum field theoretic, relativistic covariant and model-independent approach. *Eur. Phys. J.*, A18:653–666, 2003.
- [51] A. N. Ivanov, M. Faber, A. Hirtl, J. Marton, and N. I. Troitskaya. Energy level displacement of the excited n_l state of pionic hydrogen. *Eur. Phys. J.*, A19:413–422, 2004.
- [52] Dolores Eiras and Joan Soto. Light fermion finite mass effects in non-relativistic bound states. *Phys. Lett.*, B491:101–110, 2000.
- [53] R. Koch. A Calculation of Low-Energy πN Partial Waves Based on Fixed t Analyticity. *Nucl. Phys.*, A448:707, 1986.
- [54] M. L. Goldberger, H. Miyazawa, and R. Oehme. Application of dispersion relations to pion-nucleon scattering. *Phys. Rev.*, 99(3):986–988, Aug 1955.
- [55] T. E. O. Ericson, B. Loiseau, and A. W. Thomas. Determination of the pion-nucleon coupling constant and scattering lengths. *Phys. Rev. C*, 66(1):014005, Jul 2002.
- [56] J. Gasser and H. Leutwyler. Quark masses. *Phys. Rept.*, 87:77–169, 1982.
- [57] J. Gasser, H. Leutwyler, M. P. Locher, and M. E. Sainio. Extracting the pion - nucleon sigma term from data. *Phys. Lett.*, B213:85–90, 1988.
- [58] M. P. Locher and M. E. Sainio. The pion - nucleon sigma term and threshold parameters. *Nucl. Phys.*, A518:201–206, 1990.
- [59] S. R. Beane, V. Bernard, E. Epelbaum, Ulf-G. Meissner, and D. R. Phillips. The S-wave pion nucleon scattering lengths from pionic atoms using effective field theory. *Nucl. Phys.*, A720:399–415, 2003.
- [60] H. C. Schroeder et al. The pion nucleon scattering lengths from pionic hydrogen and deuterium. *Eur. Phys. J.*, C21:473–488, 2001.
- [61] Ulf-G. Meissner, Udit Raha, and Akaki Rusetsky. Isospin-breaking corrections in the pion deuteron scattering length. *Phys. Lett.*, B639:478–482, 2006.
- [62] J. Gasser, V. E. Lyubovitskij, and A. Rusetsky. Hadronic atoms in QCD + QED. 2007.
- [63] L. M. Simons. Recent results on anti-protonic atoms using a cyclotron trap at LEAR. *Phys. Scripta*, T22:90–95, 1988.

-
- [64] A. Gruber. *Coulomb-Explosion in pionischem Kohlenstoff*. Diploma thesis, Institut für Mittelenergiephysik (now: Stefan-Meyer-Institute of subatomic physics), 2003.
- [65] M. Sanchez del Rio and R. J. Dejus. XOP: recent developments. In *Proceedings of SPIE*, page 3448, 1998.
- [66] E. Wagner. *Phys. ZS*, 17:407, 1916.
- [67] H. H. Johann. Die Erzeugung lichtstarker Röntgenspektren mit Hilfe von Konkavkristallen. *Z. Physik*, 69:185, 1931.
- [68] J. Eggs and K. Ulmer. Röntgenspektroskopie mit sphärisch gekrümmten Kristallen. *Zeitschrift für angewandte Physik*, 20(2):118, 1965.
- [69] H. H. Johann. Über ein neuartiges, genau fokussierendes Röntgenspektrometer. *Z. Physik*, 82:507, 1933.
- [70] Firma Carl Zeiss, 73446 Oberkochen, Germany.
- [71] S. Lenz. *Test und Kalibration eines Kristallspektrometers für die Untersuchung von Röntgenübergängen in exotischen Atomen*. PhD thesis, Universität zu Köln, 1996.
- [72] N. Nelms et al. Precision determination of pion mass using X-ray ccd spectroscopy. *Nucl. Instrum. Meth.*, A477:461–468, 2002.
- [73] Paul Indelicato, Eric-Olivier Le Bigot, Martino Trassinelli, Detlev Gotta, Maik Hennebach, Nick Nelms, Christian David, and Leopold M. Simons. Characterization of a charge-coupled device array for bragg spectroscopy. *Review of Scientific Instruments*, 77(4):043107, 2006.
- [74] A. M. Costa, M. C. Martins, F. Parente, J. P. Santos, and P. Indelicato. *Atomic Data and Nucl. Data Tables*, 79:223, 2001.
- [75] C. Bernard. PhD thesis, Université J. Fourier, Lyon, 1996.
- [76] Nader Sadeghi, Toshiki Nakano, Dennis J. Trevor, and Richard A. Gottscho. Ion transport in an electron cyclotron resonance plasma. *Journal of Applied Physics*, 70(5):2552–2569, 1991.
- [77] S. Biri, L. M. Simons, and D. Hitz. *Rev. Sci. Instr.*, 71(2):1116, 2000.
- [78] L. M. Simons et al. On the characterisation of a Bragg spectrometer with X-rays from an ECR source. *Nuclear Instruments and Methods in Physics Research A*, 545:217, 2005.

- [79] D. F. Anagnostopoulos et al. Highly charged ions in exotic atoms research at PSI. *Nucl. Instrum. Meth.*, B205:9–14, 2003.
- [80] D. Covita et al. Accurate miscut angle determination for spherically bent Bragg crystals. Accepted for publication in *Review of Scientific Instruments*, 2007.
- [81] D. Covita, S. Schlessler, and M. Ay. Miscut Measurement at the Seifert X-ray machine – PSI. Internal report piH-note 2/2006, PSI, 2006.
- [82] Glenn F. Knoll. *Radiation Detection and Measurement*. John Wiley & Sons, Inc., 1979.
- [83] S. Baker and R. D. Cousins. Clarification of the use of CHI-square and likelihood functions in fits to histograms. *Nuclear Instruments and Methods in Physics Research*, 221:437, 1984.
- [84] T. Hauschild and M. Jentschel. Comparison of maximum likelihood estimation and chi-square statistics applied to counting experiments. *Nuclear Instruments and Methods in Physics Research A*, 457:384, 2001.
- [85] U. C. Bergmann and K. Riisager. A systematic error in maximum likelihood fitting. *Nuclear Instruments and Methods in Physics Research A*, 489:444, 2002.

Lebenslauf

Persönliche Daten

Name: DI Albert Hirtl
Familienstand: ledig
geboren am: 16. Juni 1975 in Klagenfurt
Anschrift: 1030 Wien, Charasgasse 3/16
Tel.: +43 650 / 70 79 799
E-Mail: albert.hirtl@oeaw.ac.at

Schulbildung

06/1993 Matura am Bundesrealgymnasium für Slowenen / Zvezna gimnazija za Slovence, Klagenfurt, Kärnten

Studium

10/1993 – 10/2000 Studium der Technischen Physik an der TU Wien mit Schwerpunkt Atom-, Kern- und Teilchenphysik
Diplomarbeit unter der Anleitung von Prof. M. Faber mit dem Titel *Untersuchungen zur Vortexstruktur des Quarkconfinements*

11/1999 Förderungstipendium der Technisch-Naturwissenschaftlichen Fakultät der TU Wien

20/11/2000 Verleihung des akademischen Grades Diplom-Ingenieur (DI)

Zivildienst

02/2001 – 02/2002 Sanitäter beim Österreichischen Roten Kreuz, Landesverband Wien

Beruflicher Werdegang

seit 03/2002 Wissenschaftlicher Angestellter in der Österreichischen Akademie der Wissenschaften am Stefan-Meyer-Institut für subatomare Physik, Boltzmanngasse 3, 1090 Wien, <<http://www.oeaw.ac.at/smi>>.

seit 03/2002 Arbeit an der Dissertation mit dem Titel: *Determination of the Strong Interaction Ground State Width in Pionic Hydrogen*.
Durchführung der Experimente für die Dissertation am Teilchenbeschleuniger des Paul Scherrer Instituts (PSI), Villigen, Schweiz, <<http://www.psi.ch>>.

11/2002 Organisation des Workshops: *International Workshop on Exotic Atoms - Future Perspectives (EXA02)*, Wien, <<http://www.oeaw.ac.at/smi/exa02/>>.
Erstellung und Herausgabe der zusammenfassenden Publikation *Proceedings of EXA02*, Editor.

12/2004 Organisation des Symposiums: *Cutting Edge Technologies for fundamental sciences, life science and medical applications (CET04)*, Wien, <<http://www.oeaw.ac.at/smi/cet04/>>.

02/2005 Organisation der Konferenz: *International Conference on Exotic Atoms - Future Perspectives (EXA05)*, Wien, <<http://www.oeaw.ac.at/smi/exa05/>>.
Erstellung und Herausgabe der zusammenfassenden Publikation *Proceedings of EXA05*, Editor.

seit 12/2005 Institutsverantwortlicher für das Datenbanksystem AkademIS (Akademie Informationssystem) der Österreichischen Akademie der Wissenschaft (Verwaltung der relevanten Daten für den Jahresbericht und die Berechnung der Kennzahlen für die Wissensbilanz).

Weitere Qualifikationen

Sprachen: Englisch, verhandlungssicher
Slowenisch, verhandlungssicher
Russisch, ausgebaute Grundkenntnisse
Französisch, Grundkenntnisse

EDV: Linux
MS Office
Diverse Programmiersprachen (C, Fortran, Perl, Html)

Sonstige Tätigkeiten

seit 03/2002 Ehrenamtlicher Mitarbeiter beim Österreichischen Roten Kreuz,
Landesverband Wien
seit 06/2005 Notfallsanitäter

Wien, im Februar 2008